Preparation of polyamide-based composite membranes and investigation of their performance in organic solvent separation

付, 文明

(Degree)
博士（学術）

(Date of Degree)
2024-09-25

(Date of Publication)
2025-09-01

(Resource Type)
doctoral thesis

(Report Number)
甲第9025号

(URL)
https://hdl.handle.net/20.500.14094/0100492534

Doctoral Dissertation

Preparation of polyamide-based composite membranes and investigation of their performance in organic solvent separation

(ポリアミド系複合膜の作製と有機溶媒分離性能の検討)

Jul 2024

Graduate School of Engineering
Kobe University

FU WENMING
付 文明

Acknowledgments

Completing this PhD thesis would not have been possible without the support and guidance of many individuals. I would like to express my deepest gratitude to everyone who contributed to this work.

First and foremost, I am profoundly grateful to my advisor, Professor Matsuyama. His academic guidance, unwavering support, and constant encouragement have been invaluable. His wisdom, patience, and meticulous approach to research have deeply influenced me, and I have benefited immensely from his mentorship.

I also wish to thank the members of my dissertation committee, Professor Ogino, Professor Mori, and Professor Kamio. Their insightful feedback and suggestions have greatly enhanced the quality and depth of my research.

In addition, I sincerely thank Dr. Hu for his substantial contributions to the completion of this doctoral dissertation. Furthermore, I would like to express my gratitude to Kumagai sensei, Takagi sensei, Ms. Miyake, Ms. Kamio, and Ms. Ono from the Membrane Engineering Group for their help and support in various aspects of my research and daily life, including experimental design, data analysis, and manuscript preparation. The time we have spent together has been invaluable, and these experiences will be cherished.

A special thank you goes to my family, especially my parents. Their unwavering understanding, support, and unconditional love have been my greatest source of motivation. Without their encouragement, completing this thesis would not have been possible.

Finally, I would like to acknowledge the funding and support provided by China Scholarship Council (CSC), as well as the excellent research environment and resources offered by Kobe University and Graduate School of Engineering.

FU WENMING

Graduate School of Engineering
Kobe University, Japan

Jul 01, 2024

Table of contents

Chapter 1: General introduction

1.1 Research background: organic solvent separation and purification

Organic solvent separation and purification (OSSP) technology is a fundamental technique in industries such as chemical engineering and pharmaceuticals [1-4] with broad applications in environmental protection and resource utilization. As is well known, organic solvents play an indispensable role in fields such as chemical engineering, pharmaceuticals, food processing, and electronics due to their excellent solubility and chemical reactivity. They are widely used in raw material preparation, reaction media, extractants, and cleaning agents, creating immense value for modern industrial production. However, the widespread use of organic solvents has also introduced significant environmental issues. Most organic solvents are highly toxic, volatile, flammable, and explosive. If improperly managed, they can cause severe pollution to air, water, and soil, posing threats to human health and the ecological environment. The treatment and disposal of organic waste liquids have become a bottleneck in industry development.

OSSP technology has emerged to address these issues, aiming to reduce the environmental impact of organic solvents and promote sustainable resource utilization. This technology employs physical or chemical methods to separate target products from solvents or other impurities, achieving efficient recovery and reuse of organic solvents. Traditional separation methods, such as distillation, liquid-liquid extraction, and adsorption, have been used for solvent recovery. However, these methods often have drawbacks, including high energy consumption, low selectivity, and the generation of secondary waste streams. The separation and recovery of organic solvents face challenges, necessitating the development of a new, efficient, energy-saving, and environmentally friendly solvent separation technology.

1.2 Organic solvent separation membrane technology

As an emerging technology, membrane separation technology uses the separation membrane as the core and utilizes the selective permeability principle of the semipermeable membrane to achieve the separation, concentration, and purification of multi-component mixtures driven by external pressure or chemical potential difference (**Fig. 1.1**) [5]. This technology can be performed at room temperature and has the advantages of a simple operation process, no secondary pollution, large separation coefficient, no phase change, high efficiency, and energy saving. Beginning in the late 1960s, membrane separation processes were gradually used in industrial applications and developed rapidly. Compared with traditional heat-driven separation processes (**Table 1.1**), membrane separation technology shows significant advantages and has become a revolutionary technology in the field of separation. It is reported [2] that membrane-based chemical separation technology can save up to 90% of energy compared to traditional thermally driven separation processes (**Fig. 1.2**). This means that membrane separation technology can help chemical, pharmaceutical, and other industries achieve low-carbon production and make a significant contribution to green circumstances.

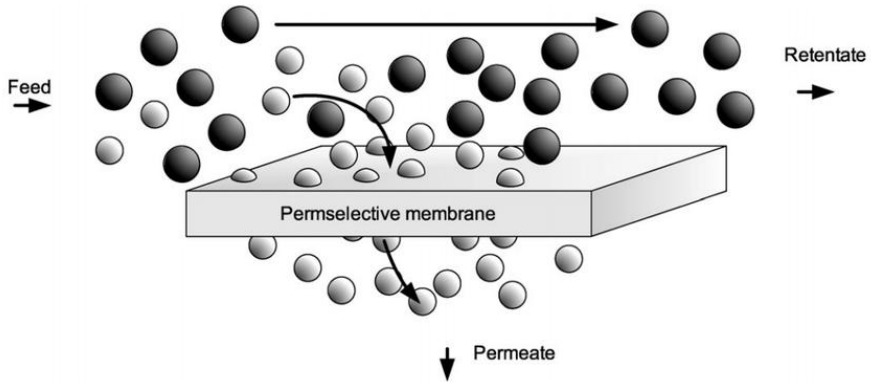

Fig. 1.1. Schematic of membrane separation [5].

Table1.1 Comparison between membrane separation technology and traditional separation methods

Aspect	Membrane Separation Technology	Traditional Separation Methods
Separation Efficiency	High	Low
Energy Consumption	Low	High
Environmental Impact	Minimal	Significant
Ease of Operation	Simple	Complex
Scope of Application	Wide	Narrow
Scalability	Good	Poor

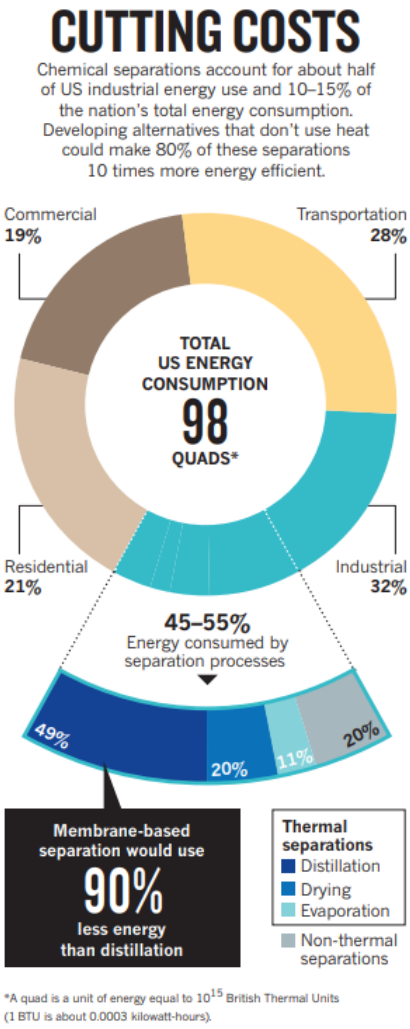

Fig. 1.2. Membrane-based chemical separation technology can save up to 90% of energy compared to traditional thermally driven separation processes [4].

Generally, membrane separation technology can be mainly divided into

microfiltration, ultrafiltration, nanofiltration and reverse osmosis membranes according to the substances to be separated and the pore size of the separation membrane (**Fig.1. 3**). Microfiltration (MF) [6] membrane: Pore size ranges from 0.1 to 10 µm, which can trap bacteria, suspended particles and other larger impurities. Ultrafiltration (UF) [7] membrane: Pore size ranges from 10 to 100 nm, which can trap viruses, macromolecules and colloidal particles. Nanofiltration (NF) [8] membrane: The pore size ranges from 0.5 to 2 nm, which can intercept small molecules, such as multivalent ions, organic molecules, and dyes, while retaining larger solutes. Reverse osmosis (RO) [9] membrane: With a pore size of less than 0.5 nm, it is extremely selective and can separate water molecules from dissolved salts and other small molecules.

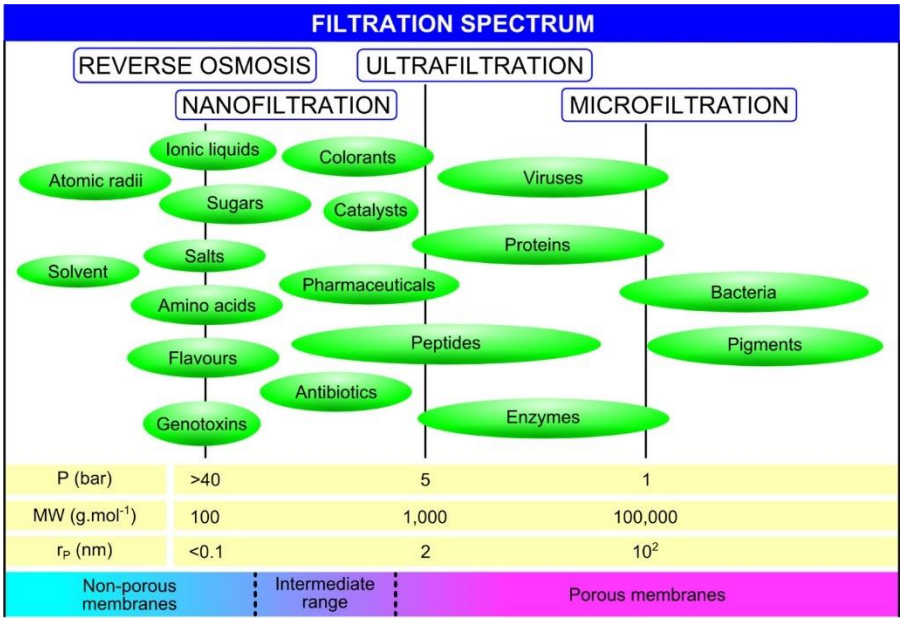

Fig. 1.3. Classification of membrane processes according to operating pressure, retained solute/pore size [nm], molecular weight cutoff [g mol^{-1}], transport mechanism, and examples of applications [2].

Organic solvent (OS) membrane separation technology refers to the application of membrane separation technology to systems involving organic solvents. In essence, this technology utilizes semipermeable membranes to selectively permeate specific components from a mixture of organic solvents, driven by external pressure or a

chemical potential gradient. Due to its high efficiency, energy-saving nature, and environmental friendliness, OS membrane separation technology has been widely applied in fine chemical and purification processes, including solvent recovery, solvent exchange, solute concentration, and solute purification. The current mainstream OS separation processes can be roughly divided into three categories (**Fig. 1.4**): organic solvent nanofiltration (OSN), pervaporation (PV) and organic solvent reverse osmosis (OSRO) [10].

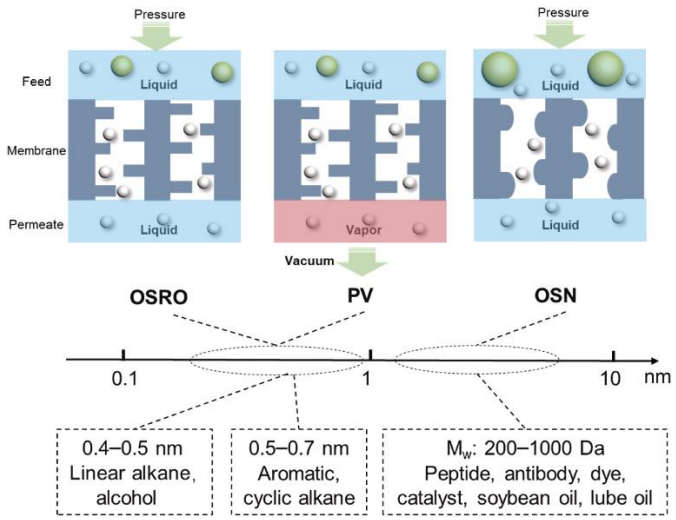

Fig. 1.4. Molecular size range for OSRO, PV, and OSN, and the representative molecules in each range [10].

1.2.1 Pervaporation (PV)

Pervaporation (PV) is a method of separating liquid mixtures through membrane selective permeation and vaporization. PV membranes separate one of the components from one bulk phase to another by controlled and selective mass transfer. The feed is in the liquid phase and the permeate is in the gas phase. PV deals with the partial vaporization of a liquid mixture through a dense membrane, whose downstream side is under vacuum (**Fig. 1.5**) [10, 11]. The vapor pressure difference across the membrane acts as the main driving force. The high vacuum on the downstream side forms a region in the membrane with a very low concentration of organic liquids. PV has great potential in the separation of organic liquid mixtures,

characterized by azeotrope separation, such as alcohol/water, alcohol/alkane and other azeotrope systems [11]. Due to selective mass transfer across membranes, PV is superior to continuous distillation for the separation of azeotropes and mixtures with high boiling points. However, continuous distillation and PV are generally considered as phase change-based separation processes or heat-based separation processes, which are inherently energy-intensive as they require large amounts of latent heat of vaporization. Nonetheless, PV is still worthy of study due to its high organic solvent separation selectivity, but the energy consumption of the entire separation process is still a problem to be solved. There is an urgent need to develop low energy consumption organic solvent membrane separation technology.

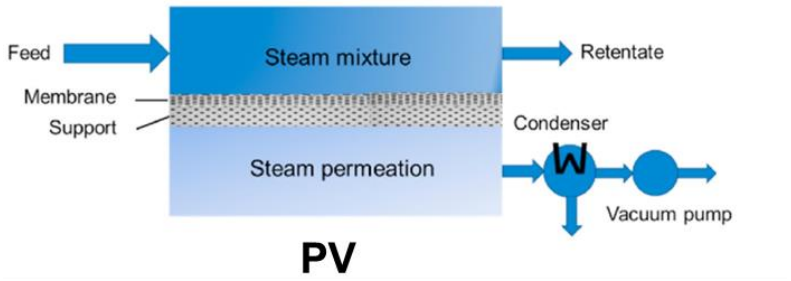

Fig. 1.5. Schematic diagram of PV separation process [12].

1.2.2 Organic solvent nanofiltration (OSN)

Organic solvent nanofiltration (OSN), also known as solvent-resistant nanofiltration (SRNF), is an emerging pressure-driven membrane separation technology that enables efficient separation of organic solvent systems (**Fig. 1.6**) [2, 12-15]. Compared to conventional separation methods, OSN technology offers several significant advantages: 1) Low operating pressure and energy consumption. OSN technology typically operates at lower pressures and consumes less energy during chemical separations, making it a more economical and environmentally friendly approach. 2) High separation efficiency. OSN membranes possess unique pore structures and surface properties, enabling them to effectively separate specific components from organic solvent mixtures, achieving high separation purity and

recovery rates. 3) Green and environmentally friendly. OSN separation processes involve no phase transitions or chemical reactions, and do not generate waste organic vapors, aligning with the principles of green chemistry and sustainable development.

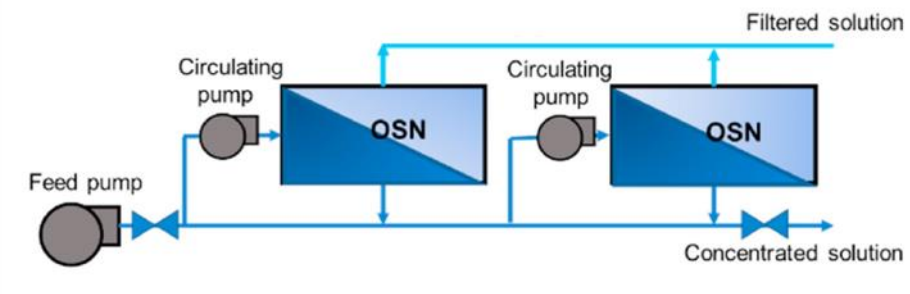

Fig. 1.6. Schematic diagram of OSN separation process [12].

OSN technology holds immense promise for various industries, including fine chemicals, pharmaceuticals, food processing, and environmental protection. Its potential applications include: 1) Recovery of organic solvents from lubricants. OSN technology can effectively recover organic solvents from lubricant, reducing resource waste and environmental pollution. 2) Separation and purification of drugs. OSN technology can be used to separate and purify active ingredients from pharmaceuticals, enhancing drug purity and quality. 3) Deacidification of vegetable oils. OSN technology can remove free fatty acids from vegetable oils, improving their quality and nutritional value. 4) Recovery of catalysts and extractants. OSN technology can be used to recover catalysts and extractants, lowering production costs and environmental impact. The core of OSN technology is the OSN membrane. Generally speaking, the pore size distribution of OSN membrane is narrow, with a pore size of 0.5-2.0 nm, and the corresponding molecular weight cutoff (MWCO) range is 200-1000 g mol^{-1}.

Research on OSN technology began in the 1960s. In 1964, Sourirajan employed cellulose acetate membranes to separate short-chain fatty acids, marking the first application of membrane separation technology in non-aqueous systems [16]. In 1965, Loeb proposed pressure-driven membrane separation technology [17]. Sourirajan and

his team dedicated over two decades to utilizing cellulose acetate membranes for organic solvent separation. Since the 1980s, companies like ExxonMobil, Shell, Union Carbide, and Dow Chemical have published numerous patents related to novel OSN materials [2]. The first commercial OSN membranes were produced by Grace, Davison, Koch, Solsep, and GMT in the mid-1990s. To date, the most successful industrial-scale application of OSN has been dewaxing in lubricating oils [2]. The breakthrough of OSN technology holds immense potential in the early 21st century. OSN applications address numerous challenges in industrial production and environmental protection [18]. However, as a newly developed technology, OSN also faces challenges, such as solvent resistance and stability of membrane materials, membrane preparation processes, and costs. These issues require further research and breakthroughs.

1.2.3 Organic solvent reverse osmosis (OSRO)

Organic solvent reverse osmosis (OSRO) is a pressure-driven membrane separation technology similar to the reverse osmosis (RO) process, but applied to organic solvent systems. OSRO uses the pressure difference on both sides of the membrane as a driving force to overcome the osmotic pressure of the solvent, allowing the solvent to pass through the membrane and intercept the solute, thereby achieving the separation, purification and concentration of the mixed solution (**Fig. 1.7**) [19]. The difference is that RO is a separation technology used in water systems, while OSRO is used in organic solvent separation systems. RO is considered to be one of the most promising technologies in the 21st century, with the advantages of no phase change, simple process, and low energy consumption [20]. RO membranes are developing rapidly in the fields of ultrapure water and pharmaceutical water preparation, food processing, municipal sewage, electroplating, printing and dyeing, papermaking wastewater treatment and reuse, seawater and brackish water desalination, and other fields [19]. The development of OSRO is still in its infancy.

In order to clearly describe OSRO, it is compared with the currently popular

OSN technology. The separation process of OSRO is affected not only by applied pressure but also by the chemical potential, while OSN is mainly driven by applied pressure [10]. Even tiny defects in the OSRO membrane can introduce pressure-driven diffusion of solvents that greatly weakens separation, making OSRO very sensitive to defects. In addition, the OSRO process requires considerable operating pressure to overcome high osmotic pressure and maximize productivity. Organic solvent mixtures usually have high osmotic pressures, and since the concentration of the OSRO separation system is much higher than that of OSN, OSRO operation usually requires a pressure higher than 30 bar, while OSN generally requires a pressure of less than 10 bar. Of course, the osmotic pressure varies with different organic mixtures, so the required pressure should be selected based on the actual situation. Furthermore, reducing the size difference between solvents results in less efficient size screening and more reliance on shape, entropy, or polar selectivity. Therefore, membrane conditioning recommendations can vary significantly between different separation systems. In summary, OSRO membranes must exhibit high stability, high pressure resistance, and good separation characteristics in organic media. All these stringent requirements have resulted in relatively slow development of OSRO membranes, while OSN research has grown exponentially (**Fig. 1.8**). Although the OSRO membrane is more difficult to fabricate than OSN and is much less developed, it has superior molecular differentiation capabilities in challenging organic liquids.

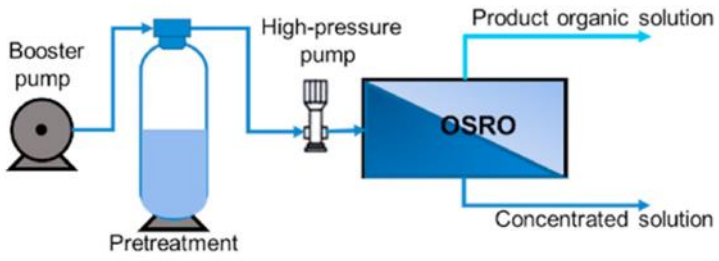

Fig. 1.7. Schematic diagram of OSRO separation process [12].

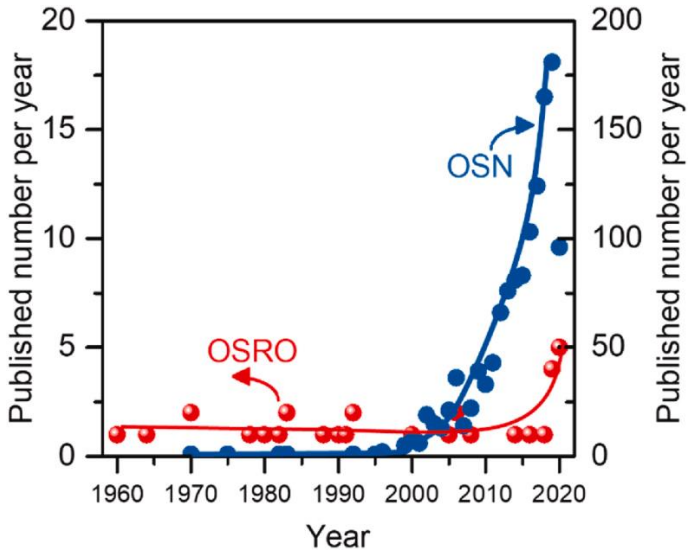

Fig. 1.8. Number of studies published per year on OSRO (red) and OSN (blue) membranes. [12].

1.3 Organic solvent separation membrane

The core component of OS membrane separation technology is the OS separation membrane, which plays a vital role in determining the overall performance and efficiency of the separation process. As early as 1965, Lobe *et al*. [21] first mentioned the idea of "pressure-driven solvent separation", but due to the limitations of solvent-resistant membrane materials, the research did not receive further development. Several key characteristics need to be considered in developing effective OS separation membranes [22]: (1) Excellent organic solvent resistance: OS separation membranes must exhibit exceptional resistance to organic solvents to ensure long-term stability and its stable separation properties over long periods of operation. (2) Processability: OS separation membranes should have good processability so that the membranes can be made into various shapes and sizes to meet different separation applications. (3) High mechanical strength and thermal stability: During the separation process, the OS separation membrane will be affected by mechanical stress and temperature fluctuations. Therefore, they must have high mechanical strength and thermal stability to maintain their structural integrity. (4) Cost-effectiveness: The production cost of OS separation membranes should be minimized to improve its economic feasibility and promote widespread adoption.

According to the properties of membrane materials, OS separation membranes can be divided into two major categories: inorganic membranes and organic polymer membranes.

1.3.1 Inorganic membranes

The OS separation membrane made of inorganic (ceramic) materials has the advantages of solvent resistance, acid and alkali resistance, high temperature resistance, narrow pore size distribution, and high separation efficiency. However, inorganic membrane materials are brittle, relatively difficult to process and form, expensive, and difficult to scale up production, so their applications are subject to certain limitations. Currently, as shown in **Fig. 1.9**, the inorganic materials used to prepare OS separation membranes are mainly silicon carbide (SiC), aluminum oxide (Al_2O_3), zirconium oxide (ZrO_2), and titanium oxide (TiO_2) [12, 23-26]. Ceramic membrane preparation methods include suspended particles, sol-gel method, anodization, chemical vapor deposition (CVD), phase separation and hydrothermal synthesis. Commercial ceramic membranes mainly use the sol-gel method.

In the 1980s, the chemical stability of ceramic membranes prepared from Al_2O_3, and TiO_2 gradually played a role in the separation of organic solvents [27]. For example, the company Sustainable Forest Education Cooperative (SFEC) built Carbosep complete ceramic membrane equipment. In 2019, Dutch PWN Technologies' ceramic membranes were successfully commercialized on a large scale in Singapore and other countries. In recent years, the modification of various ceramic membranes, the preparation of composite membranes of inorganic and organic materials, and the combination of membranes with catalytic reaction processes have accelerated innovation and expanded application fields [28]. Silicon carbide ceramic membrane is recognized as the most high-end membrane technology representative in the world and has the characteristics of high temperature resistance and strong corrosion. The flux is 5 times that of traditional membranes such as Al_2O_3, ZrO_2 and so on. It can replace sand filters and cartridge filters, greatly reducing operating costs

and difficulty. However, the cost of inorganic membrane is generally higher than polymer membranes. The large-scale production of inorganic membranes is also a significant challenge.

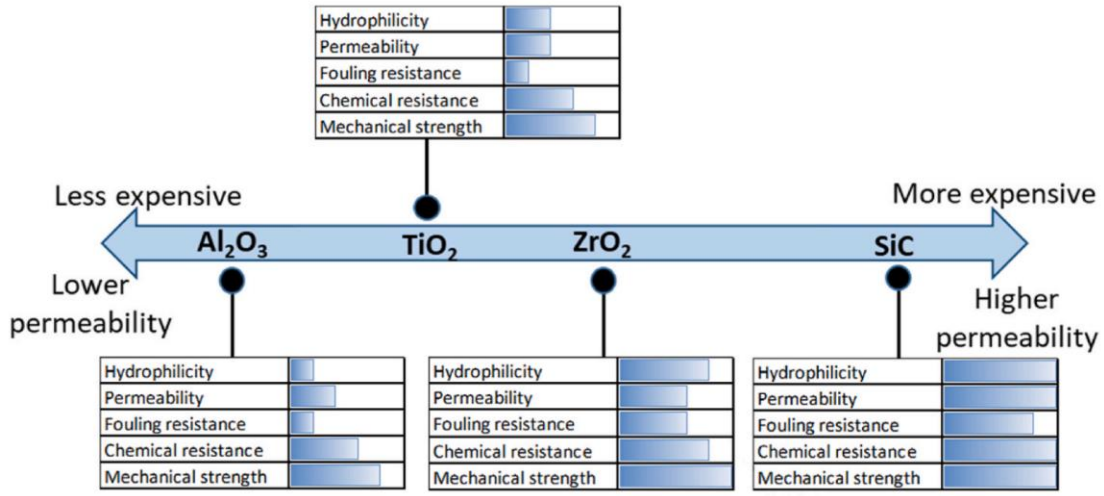

Fig. 1.9. Relative properties of ceramic membrane fabricated using alumina, titania, zirconia, and silicon carbide. [29]

1.3.2 Polymer membranes

At this stage, most commercialized OS separation membranes are made of polymer materials, such as polyamide (PA) [30], polybenzimidazole (PBI) [31], polyimide (PI) [32, 33], polyacrylonitrile (PAN) [34], poly(ether ether ketone) (PEEK) [35], polydimethylsiloxane (PDMS), and poly(ether imide) (PEI) [36], etc. This type of polymer membrane has the advantages of good molding and processing performance, high chemical stability, acid and alkali resistance, corrosion resistance, high mechanical strength, pressure resistance, etc., and has high separation selectivity.

For polymer OS separation membranes, according to their structural types, they can be divided into two categories: integral asymmetric (ISA) membranes and thin-layer composite (TFC) membranes (**Fig. 1.10**). The structural feature of the ISA membrane is a porous support layer and epidermal layer with the same composition (**Fig. 1.10a**). The polymer composed of sponge-like or finger-like micropores is the porous support layer, and the dense film is the selectively separated epidermal layer. The skin layer and the underlying support layer are formed simultaneously. Thin skin layers affect the final membrane properties, namely selectivity and permeability. The

preparation method of ISA membrane is usually through the phase inversion method, where the polymer solution is poured onto a flat support surface, and then a dense skin layer and a porous support layer are formed by controlling the evaporation rate of the solvent/non-solvent (**Fig. 1.11**). The density of the ISA membrane can be adjusted by controlling the solvent/cosolvent ratio in the polymer solution. In order to further increase the solvent resistance of ISA membranes, covalent cross-linking post-treatment is usually implemented. ISA membranes are favored for commercialization because they are easy to process and produce on a large scale, have relatively low costs, and have high mechanical strength. For example, there are commercial membranes on the market with different molecular weight cutoffs (MWCO) from 150 to 900 Da, such as DuraMem (150, 200, 300, 500 and 900 Da) and PuraMem (280, 600 Da) distributed by Evonik-MET GmbH. However, ISA membranes also have some limitations. For example, the thicker epidermal layer results in greater solvent transmission resistance and lower permeation flux; the selectivity is relatively low; and there are challenges in regulating the membrane structure and cortex thickness. This limits its further application.

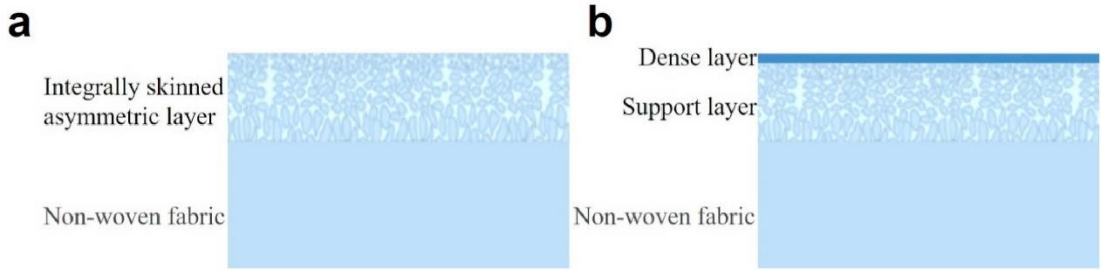

Fig. 1.10. (a) The structure of integrally skinned asymmetric (ISA) membranes. (b) The structure of thin film composite (TFC) membranes [12].

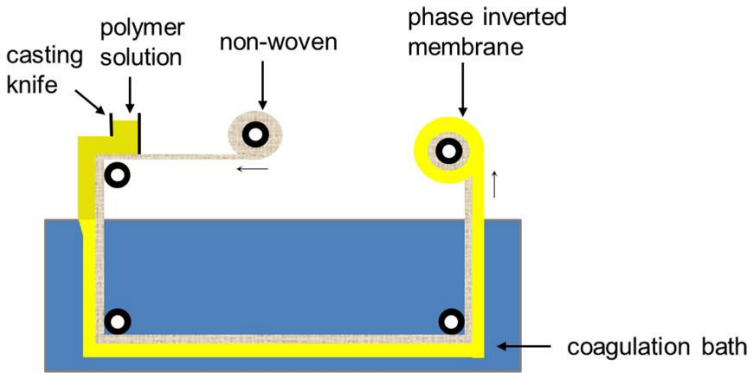

Fig.1.11. ISA membrane formation process by phase inversion [2].

TFC membranes have become an innovative technology in solvent separation technology due to their superior performance over traditional membrane types. TFC membrane consists of a porous support layer and an ultra-thin dense separation layer (**Fig. 1.10b**). The porous support layer provides mechanical strength and allows solvent penetration, while the ultrathin separation layer (often composed of different polymeric materials) exhibits excellent selectivity for specific components in the solvent mixture. Compared with ISA membranes, TFC membranes prepared by in-situ synthesis of ultrathin dense separation layers or coating thin and dense separation layers on top of porous substrates have great advantages. 1) Enhanced penetration flux. The ultrathin separation layer in the TFC membrane minimizes solvent transport resistance, resulting in significantly higher permeation flux compared to ISA membranes with a thicker dense top layer. 2) Improved selectivity. The unique structure of the TFC membrane, with a well-defined separation layer, is able to exhibit excellent selectivity for target components in the solvent mixture, resulting in purer permeate and higher separation efficiency. 3) Tailorable structure and performance. The properties of the porous support layer and ultra-thin separation layer in TFC membranes can be independently controlled to optimize performance parameters such as permeate flux, selectivity and mechanical strength to meet specific application requirements. 4) Versatility. TFC membranes can be used in a variety of solvent separation applications due to their flexibility in selecting appropriate materials and modifying the structural characteristics of the two layers. Numbers of methods, such as dip-coating, spin-coating, casting a diluted volatile solution containing a polymer

on the substrate [37], and interfacial polymerization (IP), have been developed to fabricate this thin selective layer with a thickness lower than 1 μm.

IP is a smart technique for synthesizing active layers at the interface between two immiscible phases. **Fig.1.12** shows a schematic diagram of the IP reaction. The IP reaction is a polycondensation reaction between two highly reactive monomers, one of which is dissolved in an aqueous solution and the other in an organic phase. Two monomers are covalently bonded at the interface to form a cross-linked polymer network. Pore size/structure, film thickness and degree of cross-linking can vary depending on reaction parameters such as monomer concentration, IP reaction time, additives, the nature of the monomers and so on. The IP method has achieved great success in preparing polyamide (PA) selective layers for TFC membranes. Thanks to its simple, fast, scalable production characteristics, and the excellent selectivity of the PA separation layer prepared by the IP method, TFC PA membrane has become the most successful commercial seawater desalination membrane type. Considering the good solvent resistance of PA layer, TFC PA membrane shows great potential in the field of organic solvent separation. This research will focus on organic solvent separation based on TFC PA membranes. By regulating the structure and surface properties of TFC PA membrane, it will provide theoretical guidance and technical support for the development of high-performance TFC PA membrane for organic solvent separation.

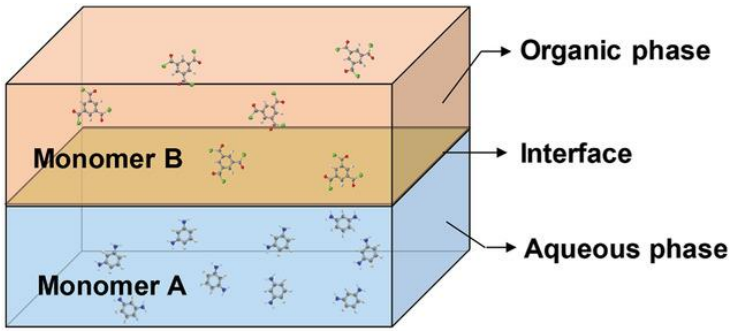

Fig.1.12 Schematic illustration of interfacial polymerization (IP) [38].

1.4 Overview of thin-film composite polyamide (TFC PA) membranes

Since 1965, Morgan proposed the first concept of using interfacial polycondensation reaction to prepare highly cross-linked and ultrathin polymer films [39, 40], the IP-prepared TFC PA membranes have been considered as one of the most important breakthroughs over the past decades. In this section, an overview of TFC PA membranes is given from the perspective of their unique structures and versatile applications. Later, unremitting endeavors on improving the TFC membrane performances are elaborately discussed in the following.

1.4.1 IP-based TFC PA membranes

Since their inception in the late 70s, PA membranes prepared by interfacial polymerization (IP) has been a key factor in the rapid growth of desalination technology [41]. The invention of TFC membranes and the discovery of the unique performance of fully-aromatic polyamide by Cadotte and coworkers brought about a major breakthrough that achieved >99% salt rejection in seawater (SW) desalination by reverse osmosis (RO) and concluded a two decade-long effort to surpass the cellulosic membranes introduced in the late 50s by Loeb and Sourirajan [2,3]. While cellulosic membranes were so-called ‘integrally-skinned’ asymmetric membranes, fabricated using a single phase-inversion step, TFC membranes comprised a selective layer added on top of a separately fabricated porous support, as schematically shown in **Fig. 1.13**. The immense success of TFC PA membranes is partly due to the very concept of a composite, which offering the potential to separately optimize each layer, but mostly due to the serendipitous ability to form robust, ultra-thin films of PA via IP. Owing to the exceptional performance, along with facile and readily up-scalable manufacturing, polyamide composites rapidly surpassed their cellulosic counterparts in most RO applications, while also demonstrating great potential for organic solvent separation [2, 30, 42].

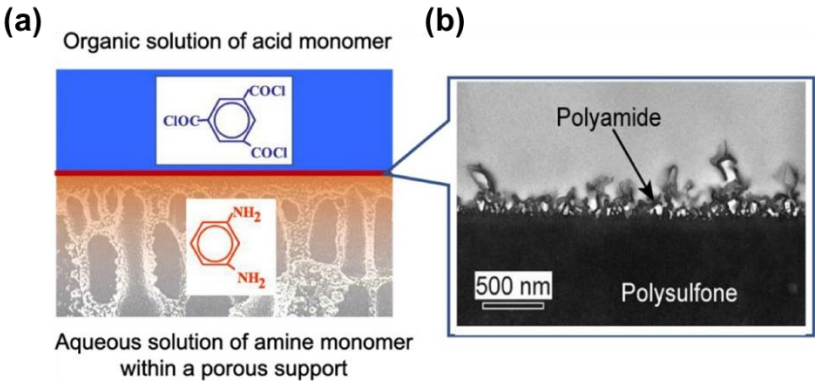

Fig. 1.13. (a) A schematic view of thin film composites membranes prepared via interfacial polymerization, (b) TEM cross-section image showing the morphology of a polyamide active layer on top of a porous polysulfone support [43].

The IP process is most commonly based on a polycondensation reaction of two polyfunctional monomers, separately dissolved in immiscible solvents, thereby the reaction occurs at the interface between the two liquid phases (**Fig. 1.13 (a)**). Among many other types of reactions amenable to interfacial polycondensation and polymerization, formation of PA membrane is by far the best known, typically involving a difunctional, hydrophobic acyl chloride and a hydrophilic diamine. The amine is placed in an aqueous solution, whereas acyl chloride is dissolved in a hydrophobic organic solvent such as hexane, immiscible with water.

The IP process for the formation of polyamide usually has the following characteristics:

(1) Self-limiting kinetics, which considerably slow down the growth of film thickness in a self-controlled manner, yielding ultra-thin films;

(2) Self-healing nature of the process that tends to direct the reaction to the most permeable spots (potential defects), sealing them and producing films with an exceptionally low defect rate;

(3) In-situ polymer crosslinking through use of multifunctional monomers, resulting in mechanically robust films with tunable barrier properties.

1.4.2 Effect of IP process on TFC PA membrane characteristics

Typical TFC PA membranes have an asymmetric structure and compose of a

porous substrate layer and a dense PA selective layer which is prepared via IP, as shown in **Fig. 1.13 (b)**. The IP technique begins with impregnating a microporous support membrane with an aqueous solution of a reactive diamine monomer such as m-phenylenediamine (MPD). Then, the porous sublayer membrane charged with the monomer is immersed into a water-immiscible organic solution containing a second reactive monomer such as a di/tri-acid chloride (e.g., trimesoyl chloride (TMC)). The polymerization of these two monomers occurs at the interface of two immiscible solvents and is diffusion-limited due to the high reactivity of the monomers. This interfacial reaction leads to the rapid formation of a highly cross-linked thin film layer that remains attached to the substrate matrix. The fabricated PA film with excellent solvents and acid/alkali-tolerance and heat-resistance is the core part of the TFC PA membrane [44]. IP process largely determines the perm-selectivity of the TFC PA membrane.

IP synthesis offers many pathways for optimizing membrane characteristics and membrane thickness via manipulation of monomer transport and reaction. One variable is the monomer concentrations in the two phases. The overall effect appears to be fairly complex, since increasing concentration may either increase or decrease film thickness. Higher concentrations drive faster diffusion across the film and so faster membrane growth. However, this also increases the reaction rate which reduces the initial film thickness. For example, when preparing aromatic polyamide membranes using the TMC-MPD reaction, the optimal composition was found to be about 0.1% of TMC in hexane and 2% MPD in water [45]. It must be stressed that the higher concentration of MPD in the aqueous phase is not indicative of the actual TMC:MPD ratio in the IP reaction, which takes place in the hexane phase, where the MPD concentration is much lower.

The nature of the solvent also plays an important role in controlling the film characteristics, as it affects monomer solubility, diffusivity, and reaction rates. For polyamide synthesis, a more polar organic solvent usually increases both amine solubility and reactivity. Accordingly, adding chloroform, a more polar solvent, to the

hydrocarbon solvent phase for encapsulation was shown to increase film permeability. Although chloroform addition would not suit TFC membranes, as this would damage the polysulfone support, other additives have been proposed in the context of aromatic polyamide RO membranes. Addition of water-soluble co-solvents such as acetone or dimethylsulfoxide (DMSO) was found to steadily increase the membrane permeance. Remarkably, they may be added to either phase with a similar effect. Presumably, the co-solvent diffusing to the organic phase along with diamine enhances its solubility and accelerates its reaction with acyl chloride, which should modify film morphology and thus its effective thickness or permeation area. The solvent viscosity may also significantly affect the ultimate film characteristics, since higher viscosity is expected to slow down the monomer diffusion. Thus, replacing hexane with isopar G (five times higher viscosity than hexane) substantially increased the membrane permeance.

Table 1.2. summarizes the major synthesis variables and their effect on the reaction, diffusion and solution thermodynamics that control the IP process and resultant polyamide film characteristics. These effects and corresponding changes in permeability point to systematic morphological changes, whose nature will be clarified below.

Table 1.2. The effects of synthesis parameters on the IP process and film formation [43].

Parameter variation	Effect
Monomer/polymer type	Reaction kinetics and enthalpy; monomer diffusivity; amine partitioning; monomer permeability in the polymer film
Monomer concentration	Rate of reaction vs. rate of mass transfer (incipient thickness); mass transfer across the film (film growth above incipient thickness)
Solvent viscosity	Monomer diffusivity; mass transfer rate
Additive: co-solvent	Amine partitioning; reaction rate; interfacial tension
Additive: surfactant	Interfacial tension; support wetting
Additive: acid/base	Increased reaction rate
Additive: polymer	Increased viscosity and reduced diffusivity

1.5 Challenges faced by polyamide organic solvent separation membranes

Polyamide (PA) membranes have shown great application potential in the field of organic solvent separation due to their excellent selectivity, chemical stability and solvent resistance. According to different application scenarios, it can be divided into PA OSN membrane and PA OSRO membrane. PA OSN membrane is mainly used to separate substances with a molecular size of 0.5-2 nm and a molecular weight of 200-1000 Da, such as antibiotics, small molecule drugs, dyes, etc. PA OSRO membranes are mainly used to separate organic liquid mixtures with a molecular size of lower than 0.5 nm and molecular weights below 100 Da, such as polar/non-polar, aromatic hydrocarbons/alkanes, isomers, organic solvents/water, etc. This section will focus on the existing problems, performance optimization and prospects of PA membranes in OSN and OSRO applications.

1.5.1 Challenges faced by TFC PA OSN membranes

TFC PA membranes have shown great application potential in the field of organic solvent separation due to their excellent selectivity, chemical stability and solvent resistance. However, the permeability of traditional TFC PA membranes fabricated by TMC-MPD reaction is low. For example, the permeance of methanol is only 0.23 L m^{-2} h^{-1} bar^{-1}. This is mainly because the PA layer of traditional TFC PA membrane has a dense structure and a low free volume, resulting in the difficulty of solvent molecules penetrating the membrane. In order to overcome the problem of low permeation flux of traditional TFC PA membranes, most research focuses on adding nanomaterials during the interfacial polymerization process to prepare thin-layer nanocomposite (TFN) PA membranes to improve the microporosity of the separation layer, thereby improving the membrane's penetration performance. For example, graphene oxide (GO) [46-48], graphene quantum dots (GQDs) [49] carbon nanotubes (CNTs) [50], silicon dioxide (SiO_2) nanoparticles [51], metal organic frameworks (MOFs) [52], and covalent organic frameworks (COFs) [53]. Nanomaterials are embedded into the PA film through interfacial polymerization. On

the one hand, nanogaps will be generated between nanomaterials and at the interface between nanomaterials and the PA membrane, thereby increasing the microporosity of the TFN PA membrane. On the other hand, adding nanomaterials to the interfacial polymerization solution can adjust the diffusion of monomers, water/oil interfacial tension, etc. to regulate the interfacial polymerization reaction, thereby affecting the surface hydrophobicity and roughness of the prepared TFN membrane and the selection of the separation layer. The cross-linking degree and thickness ultimately improve the separation performance of TFN OSN membrane. However, the TFN PA membrane has the problem of poor compatibility between nanoparticles and PA, which easily leads to the introduction of interface large pores and defects in the PA separation layer. Furthermore, the large-scale preparation of nanomaterials as well as the reproducibility and scale-up possibilities of the prepared TFN OSN films are still challenging. Therefore, it is still quite challenging to prepare high-performance TFC PA OSN membranes with stable performance and easy large-scale application. Researchers should focus more on the regulation of the interfacial polymerization process during the preparation of PA membranes in order to achieve high-flux PA OSN membranes.

1.5.2 Challenges faced by TFC PA OSRO membranes

The separation of organic liquid mixtures has been extensively studied for decades due to its importance in the chemical industry. Due to similar physical properties, strong intermolecular interactions, and the presence of azeotropes in most organic liquids, their separation can be arduous using simple distillation. [10] The emergence of OSRO technology makes it possible to separate organic liquid mixtures. PA membrane with extensive research foundation and excellent performance has become an ideal membrane material for OSRO technology. Since there are many polar bonds in the PA membrane, usually non-polar solvents cannot pass through it, so the PA membrane is particularly suitable for the separation of polar/non-polar organic liquid mixtures. Different from the problem of low permeation flux of PA membrane

in OSN, in OSRO, the problem of PA membrane is its low separation selectivity for organic liquid mixtures. To address this problem, some researchers have used a two-step heat treatment method to regulate the free volume of the PA membrane, and the prepared membrane has improved separation selectivity for organic liquid mixtures. [54] But two-step heating introduces additional energy consumption. In addition, some researchers have optimized the structure of the PA membrane by regulating the temperature of the aqueous solution during interfacial polymerization. [55] The results show that increasing the temperature of the aqueous solution can increase the cross-linking degree of the PA membrane and increase the specific surface area of the PA membrane. Although the OSRO performance of PA membrane has been improved, it is still at a low level. On the one hand, the limited polarity of the PA membrane surface limits its efficient separation of polar/non-polar organic liquid mixtures. Increasing the polarity of the PA membrane surface is expected to further improve the separation efficiency of the PA membrane for polar/non-polar organic liquid mixtures. On the other hand, PA prepared by interfacial polymerization has a wider pore size distribution, which is unacceptable for OSRO that requires fine separation. PA membrane with narrow pore size distribution is considered to be one of the most ideal OSRO membranes.

1.6 Purpose and overview of this dissertation

Polyamide (PA) membranes have great potential in the field of organic solvent separation due to their excellent solvent resistance and tunable chemical properties. This research will focus on the application of PA membranes in the currently popular OSN and the attractive and challenging OSRO. As discussed above, the molecular size of the target isolates used in OSN applications is relatively large, ranging from 0.5 to 2 nm, such as some antibodies, dyes, catalysts, and oils. While the molecular size of the target isolates used in OSRO applications is relatively small, usually less than 0.5 nm, such as mixtures of some small molecule organic solvents. Therefore, when traditional TFC PA membranes are used in the field of OSN, the TFC PA

membrane will exhibit low permeation flux due to its too-dense structure. When PA membranes are applied to OSRO fields, PA membranes will show limited selectivity due to limited surface polarity and wide pore size distribution. Therefore, the above questions will be divided into three tasks of this study:

Chapter 2: To overcome the issues of small permeation surface area and low flux in PA OSN membranes, this study employed an acetone-assisted interfacial polymerization strategy to optimize the membrane structure, creating PA membranes with a unique 3D honeycomb-like structure. This distinctive structure endowed the PA membranes with an exceptionally high specific surface area, significantly improving their OSN performance. Compared with the control membrane prepared by the conventional IP method, the modified membrane prepared by acetone-regulated IP (ARIP) exhibited 2.6 times higher methanol solvent permeance (7.0 LMH/bar) and comparable methyl orange rejection (94.6%). This work explores the underlying mechanism of acetone-regulated IP, providing a facile strategy for tailoring the membrane morphology with high-efficiency organic solvent nanofiltration.

Chapter 3: Addressing the problem of low separation efficiency in PA OSRO membranes due to weak surface polarity, this study innovatively applied a physical surface modification method. By coating the PA membrane surface with an Fe^{3+}/TA layer, an enhanced polarity surface was constructed. The increased surface polarity facilitated the formation of a polarization layer on the PA membrane surface while reducing concentration polarization effects, enhancing the interaction differences between polar and non-polar solvents on the membrane surface, ultimately significantly improving the separation efficiency of the PA membrane for polar/non-polar mixtures. Additionally, the concept of partial flux to gain a better understanding of the sensitivity and dependence of separation performance on pressure and concentration in the OSRO process was proposed. This will serve as a valuable reference for comprehending the mass transfer process in OSRO in greater depth. This study illustrates the role of the surface polarity of the PA membrane in the separation of polar/non-polar organic mixtures and emphasizes the significance of the

interaction between the components of the organic solvent mixture and the polymer membrane in the OSRO process.

Chapter 4: To address the issue of low separation efficiency in PA OSRO membranes due to wide pore size distribution, this study employed surface repair engineering techniques. By coating the PA membrane surface with a CS/GA layer, the membrane pores on the PA surface were blocked and repaired, resulting in a PA composite membrane with a narrow pore size distribution. This PA composite membrane with a narrow pore size distribution exhibited extremely high OSRO separation performance. Under the condition of a methanol/toluene mass ratio of 9:1 in the concentrated feed solution, the optimized TFC-PA-CS membrane exhibits a remarkable separation factor of 86.3, surpassing the separation performance of all previously reported OSRO membranes. This surface repair engineering method provides novel insights into the design of high-performance OSRO membranes.

Chapter 2: Polyamide composite membrane with 3D honeycomb-like structure via acetone-regulated interfacial polymerization for high-efficiency organic solvent nanofiltration

2.1 Introduction

Organic solvents are used extensively in chemical processes in various areas, such as the petrochemical, fine chemical, food, and pharmaceutical industries. Considering high toxicity/non-degradability of some organic solvents and meanwhile recycle potential of high value-added solvents, it is vital to realize organic solvent treatment *via* precise separation and purification. However, effective separation and purification of high-value-added products and recovery of organic solvents are achieved mostly through energy-intensive and thermally-driven processes (e.g., distillation and evaporation) [56, 57]. The pressure-driven membrane-based process known as organic solvent nanofiltration (OSN), or solvent-resistant nanofiltration (SRNF), is expected to provide an efficient and energy-saving alternative for the separation and purification of organic solvents [2, 13]. Over the past few decades, thin-film composite polyamide (TFC-PA) membranes fabricated *via* interfacial polymerization (IP) have become the most dominant and commercialized separation membranes for reverse osmosis (RO) [58] and nanofiltration (NF) [59] applications. Cross-linked PA is also a promising candidate for OSN because of its excellent solvent tolerance [60]. However, it is noteworthy that the high cross-linking degree of PA results in low free volume and dense structure, leading to enhanced mass transfer resistance and inevitable decrease in membrane permeability, posing a barrier to the wide range of industrial applications of TFC-PA OSN membrane [61].

For improving the OSN performance of TFC-PA membranes, various effective strategies have been explored, including implementing solvent-activated post-

treatment [60, 62, 63], reducing the thickness of the PA layer [30], introducing nanomaterials into the PA layer to construct nanochannels [53, 64], and applying organic small molecules with intrinsic microporosity or non-planar structures, such as cyclodextrins (CDs) [65-67], pillar [n]arene [68], Noria [69], and contorted phenol [70-72] as novel IP monomers to construct highly microporous OSN membranes. However, these methods face many challenges such as complex multi-stage procedures, stability, and high synthesis costs of materials [15, 73].

Increasing the specific surface area is an effective strategy for improving the permeability of TFC-PA membranes while maintaining satisfactory selectivity. For example, certain 3D structures [74] can significantly improve the permeance of TFC-PA membranes, making them a promising way for enhancing the OSN performance of TFC-PA membranes. Co-solvent assisted interfacial polymerization (CAIP) is a polymerization procedure involving the addition of a co-solvent in the organic or aqueous phase, proven to be a simple and effective method for increasing the effective permeable area of the membrane [75-82]. PA layers prepared by CAIP typically exhibit a thicker apparent thickness and multilayer structure, making CAIP a potential method for constructing PA films with 3D-like structures. Although previous works achieved refreshing results, they did not elaborate on the convective diffusion behavior of monomers at the aqueous/organic interface and its influence on the membrane structure and performance. It is generally accepted that conventional IP reactions are diffusion-controlled [77]. The diffusion rate of the IP reactants into the IP reaction zone affects the morphology of the resulting nanofilm. Therefore, an exhaustive understanding of the role of co-solvents in the IP process will help further generate and manipulate PA layers with 3D structures, thereby increasing the effective permeable area of the membrane.

In this study, a high-performance TFC-PA OSN membrane on porous polyketone (PK) supports was developed by regulating the IP with acetone as an organic co-solvent. The hydrophilic and high-porosity PK membrane can provide sufficient *m*-Phenylenediamine (MPD) supply during IP, which is favorable for the formation of

multilayer and even higher-dimensional PA membranes. This acetone co-solvent reduces the interfacial tension of the IP interface and promotes the convective diffusion of MPD and 1,3,5-benzenetricarbonyl trichloride (TMC), leading to a more vigorous IP reaction and a larger release of reaction heat, resulting in aggravated vaporization of acetone, and finally, the formation of the PA layer with a honeycomb-like structure. It was emphasized that acetone regulation and sufficient MPD supply through PK supports during the IP process were the necessary conditions for the formation of a honeycomb-like structured PA layer. This honeycomb-like structure endowed the TFC-PA-acetone membrane prepared by acetone-regulated IP (ARIP) with an ultrahigh specific surface area, significantly improving the permeability of the TFC-PA-acetone membrane. Molecular dynamics (MD) simulations were performed to reveal the underlying mechanisms of ARIP. Additionally, The permeability of the prepared membrane with a variety of organic solvents with different polarities and the rejection of a series of model dyes with different molecular weights were systematically tested. This work explores the underlying mechanism of acetone-regulated IP, providing a facile strategy for tailoring the membrane morphology with high-efficiency organic solvent nanofiltration.

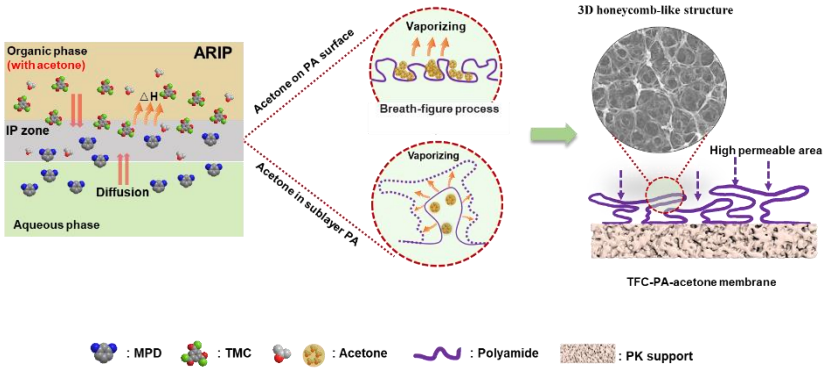

Fig. 2.1 Schematic pictures of polyamide layer formation in ARIP process.

2.2 Experimental

2.2.1 Materials

Polyketone powder (Mw=200,000 g mol^{-1}) was obtained from Asahi Kasei Company (Tokyo, Japan). Commercial polysulfone ultrafiltration membranes (PSF, CF30K) were supplied by Nitto Denko Corporation (Japan). Resorcinol (99.0%), methanol (99.8%), acetone (99.5%), and *n*-hexane (99.0%) obtained from FUJIFILM Wako Pure Chemical (Osaka, Japan) were used to prepare the PK support membranes. 1,3,5-benzenetricarbonyl trichloride (TMC, 98.0%) and *m*-Phenylenediamine (MPD, 99.0%) purchased from Sigma-Aldrich (St. Louis, MO, USA) were used to fabricate the polyamide layer on the PK support *via* interfacial polymerization (IP). Methyl orange MO (Mw=327 g mol^{-1}, 98%), rhodamine B (RDB, Mw= 479 g mol^{-1}, 95%), brilliant blue R (BBR, Mw=826 g mol^{-1}, 95%), and rose bengal (RB, Mw=1018 g mol^{-1}, 95%) provided by Tokyo Chemical Industry (Tokyo, Japan) were used as the model solutes for OSN. Other organic solvents used in this study were purchased from FUJIFILM Wako Pure Chemical Company Software (Osaka, Japan). Deionized (DI) water was produced using a Milli-Q ultrapure water system (Merck Millipore, Billerica, MA, USA).

2.2.2 Preparation of the PK support membrane

The PK support membrane was fabricated using the nonsolvent-induced phase separation (NIPS) method according to a previous report [83-85]. A certain amount of PK polymer powder was dissolved in a resorcinol/water (65/35 wt%) solvent mixture at a temperature of 80 °C with constant stirring (200 rpm) for 3 h to form a 10 wt% PK homogenous solution. Before casting, the PK solution was placed in an oven at a temperature of 60 °C overnight to remove the air bubbles. The PK solution was cast onto a non-woven polyester fabric using a casting knife with a gap of 400 μm, and then immediately immersed in a coagulation bath of methanol/water (35/65 wt%) for 20 min to complete the phase separation process. The formed PK support membrane was washed sequentially with acetone and *n*-hexane for 20 min each to remove

residual resorcinol and water. After drying in a fume hood, the PK support membrane was used as a substrate for the IP process.

2.2.3 Preparation of TFC-PA membranes

TFC-PA membranes were prepared by conventional interfacial polymerization (CIP) or ARIP using a PK membrane as the substrate (**Fig. 2.2**). The surface of the PK substrate was exposed to an aqueous solution of 2.0 wt% MPD for 2 min and the excess aqueous solution was removed using a rubber roller. After drying in the air for 1 min, a 0.1 wt% TMC/*n*-hexane solution (with or without acetone) (**Table 2.1**) was rapidly poured onto the membrane surface for 2 min to form the PA layer. After removing the TMC/*n*-hexane solution, the resultant membrane was air-dried and further post-treated in a ventilated oven at a temperature of 60 °C for 5 min. Finally, the resulting membranes were washed with deionized (DI) water and stored in methanol for further use.

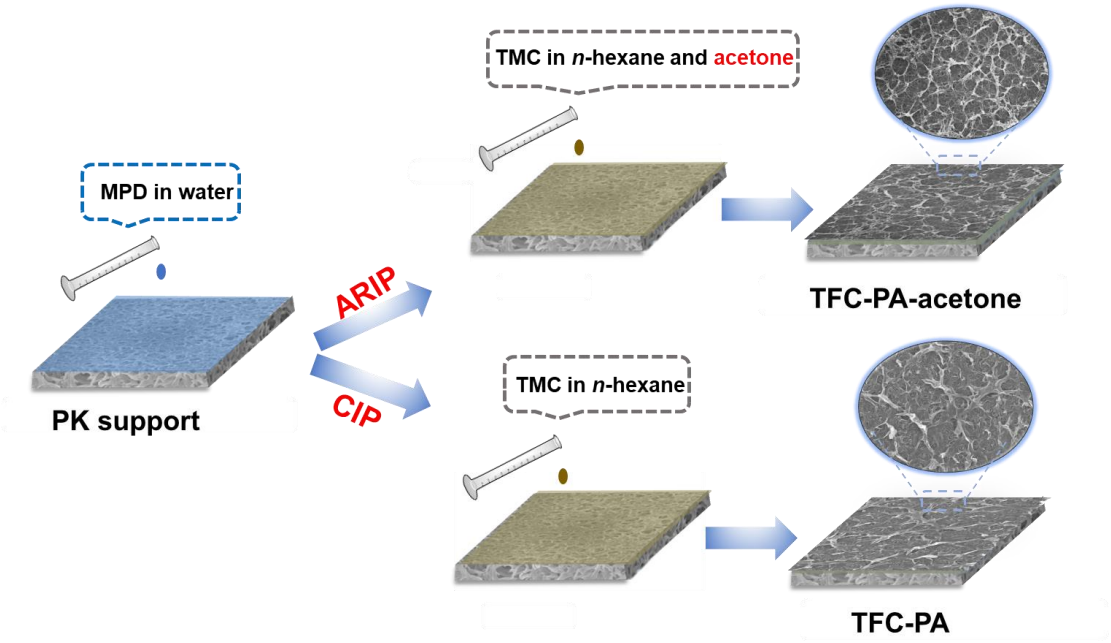

Fig. 2.2. Schematic illustration for the fabrication of the TFC-PA-acetone and TFC-PA membrane via acetone regulated interfacial polymerization (ARIP) and conventional interfacial polymerization (CIP).

Table 2.1. Composition of aqueous/organic solution for IP reaction.

Membrane	Method of preparation	Aqueous solution		Organic solution		
		MPD (wt%)	Water (wt%)	TMC (wt%)	Acetone (wt%)	*n*-hexane (wt%)
TFC-PA	CIP	2	98	0.1	0	99.9
TFC-PA-acetone	ARIP	2	98	0.1	2.0	97.9

2.2.4 Preparation of freestanding PA-acetone membranes

Freestanding PA-acetone membranes were fabricated using ARIP at a free-aqueous/organic interface. A 2.0 wt% MPD aqueous solution was dropped onto a glass slide followed by the addition of 0.1 wt% TMC *n*-hexane solution containing 2.0 wt% acetone, the two immiscible phases was allowed to contact for 2 min. Subsequently, the aqueous and organic phase solutions were immediately drained to obtain freestanding PA-acetone membranes, which were then washed with clean DI water. Finally, the freestanding PA-acetone membranes were transferred onto nylon support and further post-treated in a ventilated oven at a temperature of 60 ℃ for 5 min. The resulting membranes were cooled to room temperature for further characterization.

2.2.5 Interfacial tension measurement

The interfacial tension at the water and *n*-hexane solution (with the addition of different concentrations of acetone) interface was evaluated using the Du Noüy ring method on an Attension Sigma 700 tensiometer (Biolin Scientific, Sweden). Initially, 20 mL *n*-hexane solution with different concentrations of acetone was carefully added to the surface of the water (40 mL) to form a stable interface without any bubbles. The Du Noüy ring was then lowered into the water phase, and the interfacial tension was determined by measuring the force required to pull the ring back to the water/*n*-hexane interface. The Du Noüy ring was cleaned with ethanol (EtOH) and *n*-hexane, successively, and cauterized by flame (~1300 °C) for ~60 s to completely remove contaminants on its surface.

2.2.6 Monomer diffusion experiment

Ultraviolet-visible (UV-vis) spectroscopy (V-650KE, JASCO Company, Japan) was used to investigate the diffusion behavior of the monomers. The absorbance-concentration standard curve was obtained by measuring the absorbance of different concentrations of MPD/*n*-hexane and TMC/water solutions (**Fig. 2.3**). The absorbance changes of *n*-hexane above the MPD/water solution and water below the TMC/*n*-hexane solution was measured after adding different concentrations of acetone to the *n*-hexane phase. To measure the MPD concentration change in the *n*-hexane phase, 1.0 mL of 2.0 wt% MPD/water solution was slowly added to a quartz cuvette to ensure that the optical path of the spectrometer was above the MPD aqueous solution. The test was performed after adding 2.0 mL of *n*-hexane with different concentrations of acetone. Similarly, when measuring the TMC concentration change in the water phase, 2.0 mL of pure water was slowly added to a quartz cuvette to ensure that the liquid level of the pure water remained high on the optical path of the spectrometer. The test was performed by adding 1.0 mL of 0.1% TMC/*n*-hexane with different acetone concentrations. The time from the addition of the two-phase solvent to the quartz cuvette to the start of the test was controlled within 30s.

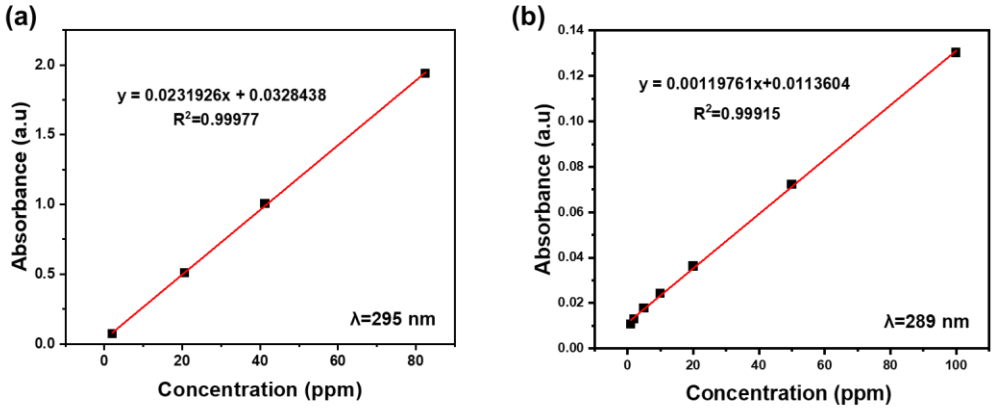

Fig. 2.3. Concentration-absorbance standard curves of (a) MPD/*n*-hexane and (b) TMC/water.

2.2.7 Reaction heat measurement

In this system, the temperature of the reactor is adjusted by controlling the

temperature of the jacket. 60 mL of 2.0 wt % MPD aqueous solution was added to the reactor. The temperature of the system was then adjusted to 298 K with stirring at a speed of 200 rpm. After stabilization for 60 min, 5 mL of 0.1 wt % TMC/hexane solution (with 2 wt % acetone) was added dropwise to the reactor.

During the reaction, the temperatures of the reactor, T_R (K), and jacket T_J (K) were monitored. The total heat generated by the reaction was equal to the total heat transferred from the reactor to the jacket during the reaction. The rate of heat transfer from the reactor to the jacket, Q (J s^{-1}), is expressed as follows:

$$Q = U \cdot A\left(T_R - T_J\right) \tag{2.1}$$

where U (J m^{-2} K^{-1} s^{-1}) and A (m^2) are the heat-transfer coefficient and surface area, respectively. Therefore, the heat of the reaction, H (J), can be calculated by integrating Q over the reaction time.

$$H = \int U \cdot A\left(T_{\mathrm{R}} - T_{\mathrm{J}}\right) \tag{2.2}$$

The value of UA was determined by calibration as 625.9×10^{-3} J K^{-1} s^{-1}.

2.2.8 Molecular dynamics (MD) simulation

MD simulations were performed to investigate the interfacial properties of the water/*n*-hexane and water/*n*-hexane-acetone interfaces. All MD simulations were performed using the Forcite module with Condensed-phase Optimized Molecular Potential for Atomistic Simulation Studies II (COMPASS II) force field in the commercial software BIOVIA Materials Studio 2020.

The water/*n*-hexane interface was constructed with 3500 water and 500 *n*-hexane molecules inserted into a rectangular box (XYZ parameters:47 × 47 × 180 $Å^3$) with periodic boundary conditions applied in all three dimensions. The interface was parallel to the *XY* plane, with the water phase at the bottom layer and *n*-hexane at the top layer of the simulation box.

The water/*n*-hexane-acetone interfaces with different acetone concentrations were constructed with the same numbers of water and *n*-hexane as for the water/*n*-hexane interface, except that 25, 50, 100 acetone molecules were added to each

simulation box corresponding to 0.5 wt%, 1.0 wt% and 2.0 wt% of acetone addition, respectively. It is noteworthy that the number of acetone molecules was higher than that under realistic scenarios in the experiments. Using this concentrated acetone organic solution, the diffusion of acetone molecules at the interface was visualized.

After the initial configurations were defined for each system, a geometry optimization process was performed for a maximum of 50000 iterations, followed by a dynamic run for 50 ps with NVE (constant number of molecules, volume, and energy) ensemble at 298 K. A time step of 1.0 fs was used. Then 50 ps of equilibration with NVT (constant number of molecules, volume and temperature) ensemble at 298 K was applied to each system, during which properties (e.g., energy and temperature of the system) were analyzed. The simulation results (including trajectories and the diffusion properties of different solvent molecules) of the final 10 ps run in NVT ensemble were used for data analysis.

An examination of the animated trajectories shows that the structure of the water/*n*-hexane interface exhibits a depletion zone between the two phases, as previously reported [86-88]. In contrast, there is no such depletion zone in the water/*n*-hexane-acetone interface systems at any acetone concentration. The structures of the water/*n*-hexane-acetone interfaces with different acetone additions are observed to become highly disordered, and in each system, the effective surface region is broadened due to the intermixing of water, acetone, and *n*-hexane molecules.

To facilitate discussion of the properties of the water/*n*-hexane-acetone interface systems, the definition of interfacial width in previous works was adopted (it is not necessary to define the interfacial width for a water/*n*-hexane system because there is a definite depletion zone in such systems) [89, 90]. Since unambiguous characterization of the width of the interface separating two immiscible components is not possible, the definition here is the distance of region from where the water density drops from 90% to 10% of its bulk value, to where the *n*-hexane density increases from 10% to 90% of its bulk value. On this basis, the width could be calculated and the fluctuations in the interfacial width can be evaluated after the equilibration period

2.2.9 Characterizations

The surface chemical structures of the membranes were analyzed using an attenuated total reflection Fourier Transform Infrared Spectrometer (ATR-FTIR; Alpha, Bruker, USA). Field-Emission Scanning Electron Microscopy (FE-SEM, JSM7500F, JEOL Co. Ltd., Tokyo, Japan) was used to observe the surface and cross-sectional morphologies of the membranes. The surface roughness of the membranes was characterized by Atomic Force Microscopy (AFM, SPI3800N, Hitachi, Ltd., Japan) in the dynamic force microscopy (tapping) mode. The reaction heat of interfacial polymerization was detected using a Heat Flow Calorimeter (Flexy CUBE-HFC, SYSTAG, Switzerland).

2.2.10 OSN performance

The OSN performance was evaluated by testing the rejection of various model dyes and the flux of various organic solvents in a cross-flow filtration system [83, 91]. Before the test, the membrane was placed in a stainless-steel cell that has an effective permeation area of 7.07 cm^2. The flow rate of the feed solution was adjusted to 9.9 mL min^{-1} by using a dual pump (KP-21 series; FLOM Co., Japan). Pure solvent flux tests were performed by pre-compacting the membrane until a stable permeate flux was obtained. MeOH solutions with various dissolved dyes were used as the feed solutions (50 ppm) for rejection testing. To minimize the concentration polarization, the stirring speed of the stainless-steel cell was adjusted to 600 rpm. To maintain a constant feed concentration, a sufficient amount of feed solution was used and replenished as needed. The solvent permeability (J_v, L m^{-2} h^{-1} bar^{-1}, LMH/bar) and dye rejection (R, %) were calculated using Equations (1) and (2):

$$J_v = \frac{V}{A * T * P} \tag{2.3}$$

where V, A, T, and P are the respective permeate volume (L), effective membrane area (m^2), operation time (h), and operated transmembrane pressure (bar).

$$R = \left(1 - \frac{C_p}{C_f}\right) \times 100\% \quad (2.4)$$

where C_p and C_f are the solute concentrations of the permeate and feed solutions, respectively, detected using a UV-vis spectrometer (V-650KE, JASCO Company, Japan). The organic solvents used for the OSN performance test were acetonitrile (ACN), acetone, methanol (MeOH), ethanol (EtOH), isopropanol (IPA), and *n*-hexane. The solutes used for the rejection test were methyl orange (MO), rhodamine B (RDB), brilliant blue R (BBR), rose bengal (RB) dyes.

All tests were performed at room temperature under a pressure of 5 bar. All data reported were obtained from more than three parallel samples and consisted of the average value of multiple tests.

2.3 Results and discussion

2.3.1 Membrane characterization

Fig. 2.4a and 2.4b show the SEM images of the TFC-PA and TFC-PA-acetone membranes fabricated by CIP and ARIP, respectively. The surface SEM images confirmed that the addition of acetone to the organic phase significantly affected the morphology of the membrane. Large leaf-like structures covered most of the typical ridge-and-valley structures on the TFC-PA membrane surface (**Fig. 2.4a)**. It could be attributed to the high surface porosity and strong hydrophilicity of the PK substrate (**Table 2.2**), which provided more MPD supply during the IP process [92-95]. An interesting phenomenon observed in this work was that the TFC-PA-acetone membrane exhibited a completely different structure, displaying a unique 3D honeycomb-like network structure with the addition of acetone as the organic co-solvent (**Fig. 2.4b)**. The cross-sectional SEM images (**Fig. 2.4c and 2.4d)** show that although the apparent thickness of the TFC-PA-acetone membrane (~991 nm) was approximately twice as large as that of the TFC-PA membrane (~495 nm), the intrinsic thickness of both of the PA layers was almost the same (~27 nm).

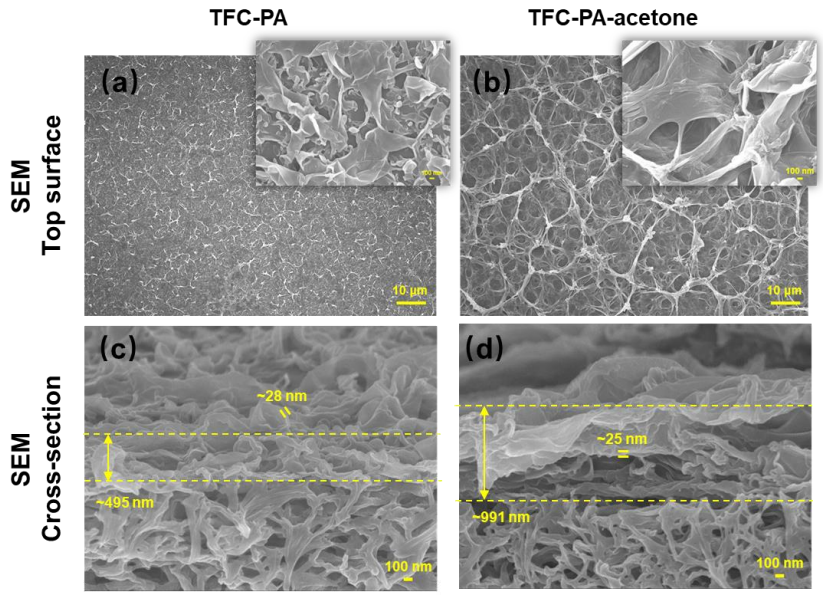

Fig. 2.4 SEM surface morphologies and SEM cross-sectional morphologies of the (a, c) TFC-PA membrane, (b, d) TFC-PA-acetone membrane. The inset is the SEM image at a large magnification.

Table 2.2. Properties of the fabricated porous PK and commercial PSF support membranes.

Membrane	Thickness (μm)	Mean pore size （nm）[a]	Surface porosity （%）[a]	Surface roughness (nm)	Water contact angle (°)	Pure methanol permeance (LMH/bar)
PK	240±10	121±22	35.6±4.3	71.8±3.2	38±4	420±30
PSF	160	77±7	5.7±0.3	9.2±0.2	92±3.0	-

[a] Calculated using ImageJ software

The FTIR spectra (**Fig. 2.5a**) results show that the intensity of the amide II band (1539 cm^{-1}) was increased by the addition of acetone, indicating an increase in the amount of PA formation. The large amount of PA seemed to thicken the PA layer, which consistent with the increase in the apparent thickness of the PA layer. **Fig. 2.5b** confirms the presence of enlarged voids inside the PA layer of the TFC-PA-acetone membrane, which may have facilitated solvent molecular transport through the membrane. This is because these enlarged voids are non-selective defects. It has no penetration resistance and can effectively improve the permeability of the PA layer

[76, 94, 96-98]. Furthermore, **Fig. 2.5c and 2.5d** show that the surface of the TFC-PA-acetone membrane was much rougher than that of the TFC-PA membrane. The average surface roughness value (Ra) of the TFC-PA-acetone membrane (236.2 nm) was about 3.5 times larger than that of the TFC-PA membrane (68.4 nm). The AFM results agree with the SEM results. However, it is noteworthy that the AFM technique has certain limitations, specifically in its inability to access the internal features of the 3D honeycomb-like network structure which results in an underestimated effective membrane roughness and membrane filtration area [98]. The 3D honeycomb-like network structure of the TFC-PA-acetone membrane greatly improves its specific surface area, thereby improving the OSN performance.

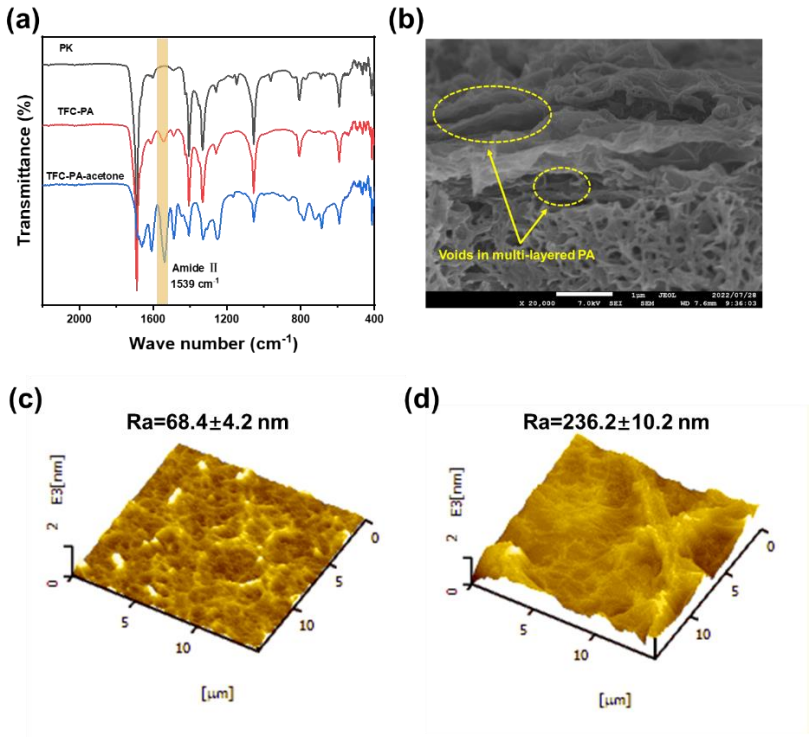

Fig. 2.5 (a) ATR-FTIR spectra of PK support, TFC-PA (without acetone) and TFC-PA-acetone membranes. (b) Cross-section image of TFC-PA-acetone membrane (with 2.0 wt% acetone). The 3D AFM profile of the (c) TFC-PA membrane, (d) TFC-PA-acetone membrane.

For analyzing the role of the PK support membrane in the formation of the 3D honeycomb-like structure, a freestanding PA-acetone membrane was prepared by

ARIP at the free water-oil interface. Surprisingly, the freestanding PA-acetone membrane exhibited a 3D honeycomb-like structure similar to the TFC-PA-acetone membrane (**Fig. 2.6a**). As a control, a PA-acetone@polysulfone (PSF) membrane was fabricated *via* ARIP on a hydrophobic PSF support membrane with low surface porosity (**Table 2.2**). The PA-acetone@PSF membrane did not exhibit a honeycomb-like structure (**Fig. 2.6b**) but exhibited a multilayer structure similar to that reported in the literature [76, 79, 80]. It was speculated that the hydrophilic PK with high surface porosity could store more MPD than hydrophobic PSF membranes with low surface porosity, which could provide sufficient MPD supply for the formation of 3D honeycomb structure PA during IP process. This suggests that a sufficient MPD supply during the IP process is one of the necessary conditions for the formation of PA with a 3D honeycomb-like structure. **Fig. 2.6a and 2.6d** show SEM images of the top side (facing the organic phase) and the back side (facing the water phase) of the freestanding PA-acetone membrane, which confirmed its multilayer structure containing a sublayer (back side) and a top layer (top side). The top layer exhibited a honeycomb-like porous structure (**Fig. 2.6c**). The sublayer showed a relatively dense structure, and the honeycomb-like structure of the top layer was mapped onto the sublayer (**Fig. 2.6a**), indicating that the sublayer was very thin.

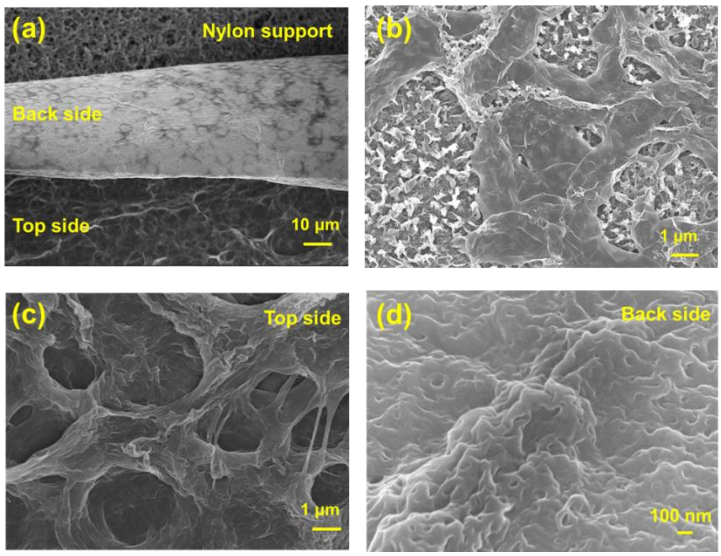

Fig. 2.6. (a) SEM surface morphologies of the freestanding PA-acetone membrane on nylon support. (b) SEM surface morphologies of the PA-acetone@PSF composite

membrane (with 2.0 wt% acetone). (c) The top surface SEM of the freestanding PA-acetone membrane (top side). (d) The bottom surface SEM of the freestanding PA-acetone membrane (back side).

2.3.2 The effect of acetone on the formation of PA membrane with a 3D honeycomb-like structure

The characteristics of water/*n*-hexane interface was investigated through interfacial tension experiments and MD simulations to dissect the role of acetone in the formation of a PA membrane with a 3D honeycomb-like structure. The effect of acetone concentration on the interfacial tension was evaluated, as described in **Fig. 2.7**. The results demonstrated that the interfacial tension of the water/*n*-hexane interface reduced from 51.5 mN/m to 32.8 mN/m with an increase in acetone concentration from 0 wt% to 3.0 wt%. This may be because acetone, like a surfactant, contains both a hydrophilic ketone group and two hydrophobic methyl groups. Acetone molecules could enter the water/*n*-hexane interface and significantly reduced the interfacial tension [48]. As acetone concentration increased, the number of acetone molecules at the interface increased, further decreasing the interfacial tension. This means that more water molecules and *n*-hexane molecules will enter the interfacial to form a wider interface area.

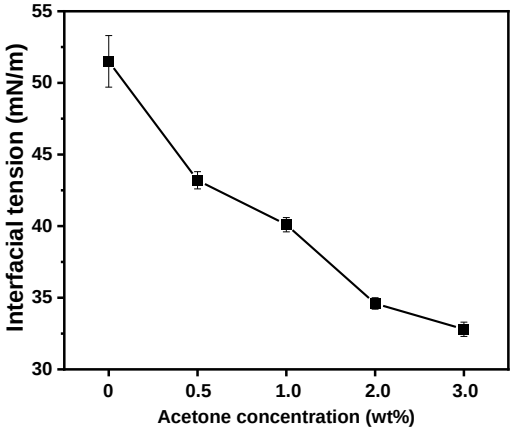

Fig. 2.7. Variation of interfacial tension between water/*n*-hexane interface with different acetone concentration

The MD simulation results validate this assumption that the width of the

interface between the two immiscible liquids, i.e., water and *n*-hexane, regarded as the IP reaction zone, increased from 10.0 Å to 25.5 Å (**Fig. 2.8a-c**) with an increase in acetone concentration from 0 wt% to 2.0 wt%. After adding acetone in the organic phase, the sharp interface separating the water and *n*-hexane solutions (**Fig. 2.8a**) becomes disordered due to the intermixing of the three solvent molecules. The disordered interfacial structure became more significant with increasing acetone concentration (**Fig. 2.8b**). It is noteworthy that the simulated pure water/*n*-hexane interface is very non-planar on a microscopic scale, and nanovoids can be observed in this system, as reported previously [86-88]. The intermixing of the three solvent molecules was primarily induced by acetone as it has high solubility in both the water and *n*-hexane phases (**Table 2.3**). As water and *n*-hexane molecules diffused and intermixed, the IP reactive monomers in each liquid phase (i.e., MPD in water and TMC in *n*-hexane) also diffused into each other phase, inducing interfacial instability into the IP process. [99] This intermixing process results in the formation of a PA layer with a thicker interfacial width. The MD simulation results are consistent with the SEM images for both the surface and cross-sectional morphologies of the PA membranes in water/*n*-hexane-acetone systems (**Fig. 2.4d**), and confirm the postulations in the interfacial tension measurements. As shown in **Fig. 2.8d**, as the concentration of acetone increased, the depth of acetone diffusion into the water/*n*-hexane interface increased similarly (after 50 ps of two-phase contact), which is consistent with the trend of increasing interface width.

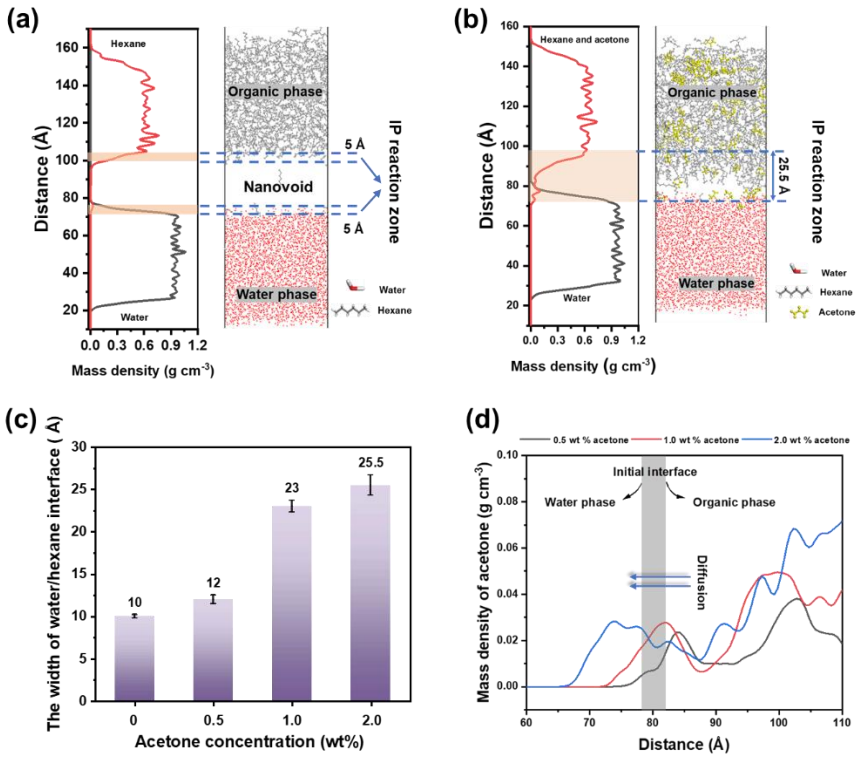

Fig. 2.8 MD simulation results. The width of the water/*n*-hexane interface (a) without acetone and (b) with 2.0 wt% acetone. (c) Water/*n*-hexane interface width with different acetone concentration. (d) The change of the acetone mass density within 50 ps after two-phase contact.

Table 2.3. Hansen solubility parameters of solvents used in interfacial polymerization

solvents	Hansen solubility parameter $(MPa^{1/2})$			
	Total	δ_D	δ_P	δ_H
Water	47.8	15.6	16.0	42.3
Hexane	15.3	15.3	0	0
Acetone	19.9	15.5	10.4	7.0

It is generally accepted that the conventional IP reaction is a diffusion-controlled reaction that occurs in the organic phase because of the unfavorable dissolution of acyl chloride in the aqueous phase [77]. Therefore, the rate of diffusion of the IP reactants towards the IP zone is a critical parameter in the IP reaction [100], that affects the morphology of the resulting nanofilms. To illustrate the diffusion behavior of the IP reactants in the IP zone, different acetone contents were used as an organic co-solvent. **Fig. 2.9a** indicates that the addition of acetone greatly promotes the diffusion of MPD to the organic phase. Particularly, after the addition of 2.0 wt%

acetone, the concentration of MPD in the organic phase increased from 3.2 ppm to 89.3 ppm (about 28 times). High concentrations of TMC were also detected in the water phase. The TMC concentration in the water phase increased from almost 0 ppm to 46.8 ppm with the addition of 2.0 wt% acetone. The increase in the IP reactant concentration in the IP reaction zone inevitably led to more vigorous IP reactions. A reaction heat test was performed where the heat release of ARIP and CIP was observed for further validation. The reaction heat value of ARIP (121.8 J) with higher IP reactant concentrations in the reaction zone was approximately 2.2 times larger than that of CIP (55.9 J), indicating that ARIP is a more violent exothermic reaction than CIP (the values of the reaction heat originated and calculated from the data in **Fig. 2.9b**).

The long-term diffusion behavior of the IP reactants was explored in **Fig. 2.9c** and **2.9d**, which show that MPD and TMC exhibit different diffusion behaviors induced by acetone. The MPD concentration in the organic phase almost reached its maximum at the initial stage of diffusion. While the concentration of TMC in the water phase did not reach a maximum at the initial stage of diffusion but increased with time. The difference in diffusion rate is due to a higher solubility of MPD in the organic phase, enabling quick entering into the organic phase under the induction of acetone. However, the TMC has low solubility in the pure water phase and its concentration will increases when TMC molecules are dragged with the acetone diffusing into the water phase. When the acetone concentration exceeds 2 wt%, a part of the MPD is also dragged into the water phase by acetone, resulting in a decrease in the MPD concentration in the organic phase. It is noteworthy that during the IP process with the reactive monomers, the dense PA film formed by the reaction of MPD and TMC prevents further diffusion of acetone into the aqueous phase. Thus, it is expected that during the ARIP process, a portion of acetone is retained in the chain segment of the formed PA, and more acetone is intercalated into the PA segments closer to the membrane surface.

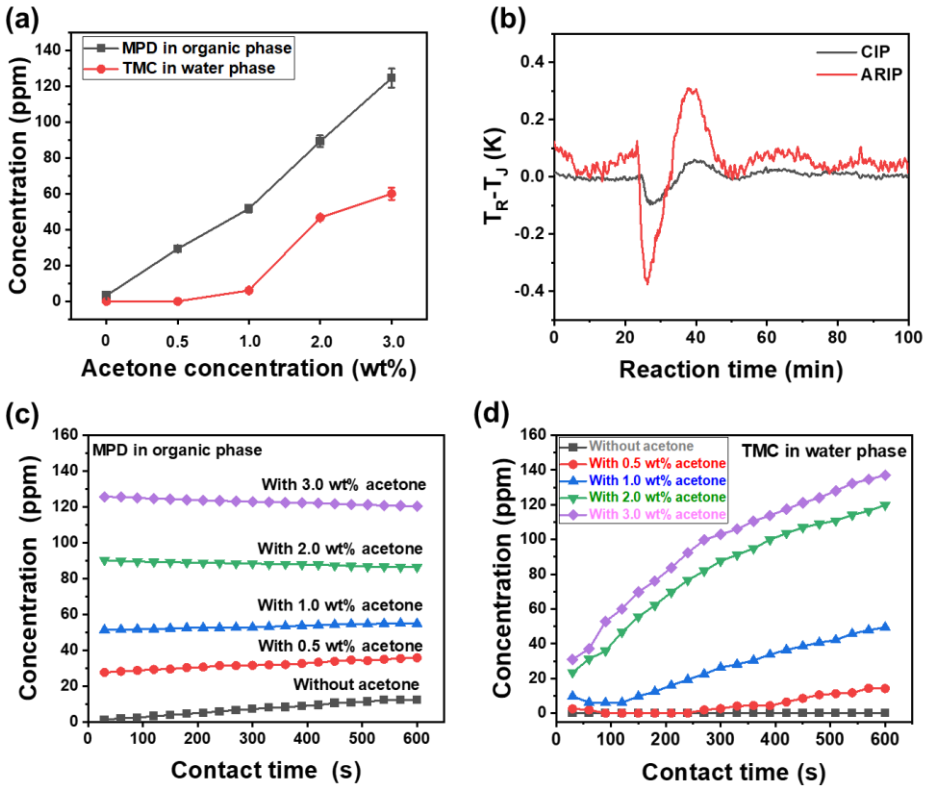

Fig. 2.9. (a) Variation of MPD concentration in the organic phase and TMC concentration in the water phase (contact time: 120s) with different acetone concentrations. (b) Temperature difference between the reactor and jacket in CIP and ARIP （with 2.0 wt% acetone）systems as a function of reaction time . (c) Time course of MPD concentration in organic phase with different acetone concentrations. (d) Time course of TMC concentration in water phase with different acetone concentrations.

Reasonable speculation on the formation mechanism of 3D honeycomb-like PA membranes is as follows (**Fig. 2.9**). Compared to the CIP, acetone reduced the water/*n*-hexane interfacial tension, and broadened the IP reaction zone during ARIP. This resulted in convective diffusion of MPD and TMC into the IP reaction zone, greatly promoting the IP reaction and leading to a dramatic exotherm. The violent exothermic reaction aggravated Rayleigh-Bénard convection [30, 43] and Marangoni flow [43]. Simultaneously, the acetone-induced relative motion of each phase in the fluid roll-to-roll process (fluid shear) may have caused interfacial instability and eventual deformation of the 3D wrinkled PA film [101]. As mentioned above, acetone molecules will be wrapped in the surface of these wrinkled PA, and finally form a 3D honeycomb-like structured PA by the evaporation of acetone (breath-figure preparation method) [102, 103]. Furthermore, when the acetone in the sublayer PA evaporated, causing the formation of voids in the membrane (**Fig. 2.5b**).

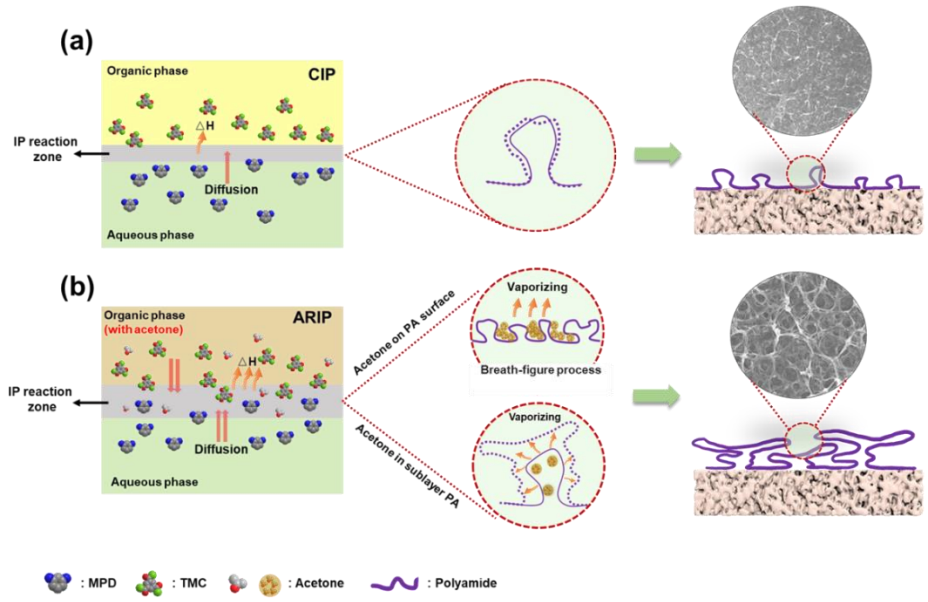

Fig. 2.9. Schematic pictures of polyamide layer formation in (a) CIP and (b) ARIP.

2.3.3 Organic solvent nanofiltration performances of TFC-PA-acetone membranes

The OSN performance of the TFC-PA-acetone membranes was optimized by adding different acetone concentrations and varying the IP reaction times. The results show that the TFC-PA-acetone membrane prepared with 2.0 wt% acetone and IP reaction time of 120s exhibits the best separation performance with a MeOH permeance of 7.0 LMH/bar and a MO rejection rate of 94.6% (**Fig. 2.10a, b**). **Fig. 2.10c** shows the various organic solvent permeances of the TFC-PA and TFC-PA-acetone membranes prepared under the above-mentioned optimal conditions. It is worth noting that the TFC-PA-acetone membrane prepared by ARIP exhibited significantly higher solvent permeance than that of the conventional TFC-PA membrane. For example, the solvent permeance of the TFC-PA-acetone membrane can reach up to 17.3 LMH/bar, 11.2 LMH/bar, and 7.0 LMH/bar for acetonitrile, acetone, and methanol, respectively, approximately 2-3 times higher than those of the TFC-PA membrane. The high performance of the TFC-PA-acetone membrane can be attributed to its ultrahigh specific surface area due to its honeycomb-like structure.

The permeance against the solvent physical and chemical properties, such as viscosity (η: pa·s), molar diameter (dm: nm), and Hansen solubility parameter due to

the polar attraction (δp: $MPa^{1/2}$), was plotted based on previously reported literature [30] (**Fig. 2.10d, Table 2.4**). The results show that regardless of the type of membrane (TFC-PA and TFC-PA-acetone), its organic solvent permeation conformed to the phenomenological transport model of the polyamide membrane reported in the literature [30]. It indicates that the PA layer prepared by ARIP does not alter the transport properties of solvents across the PA membrane. This further implies that the increase in TFC-PA-acetone membrane permeance is due to its high specific surface area endowed by its honeycomb structure.

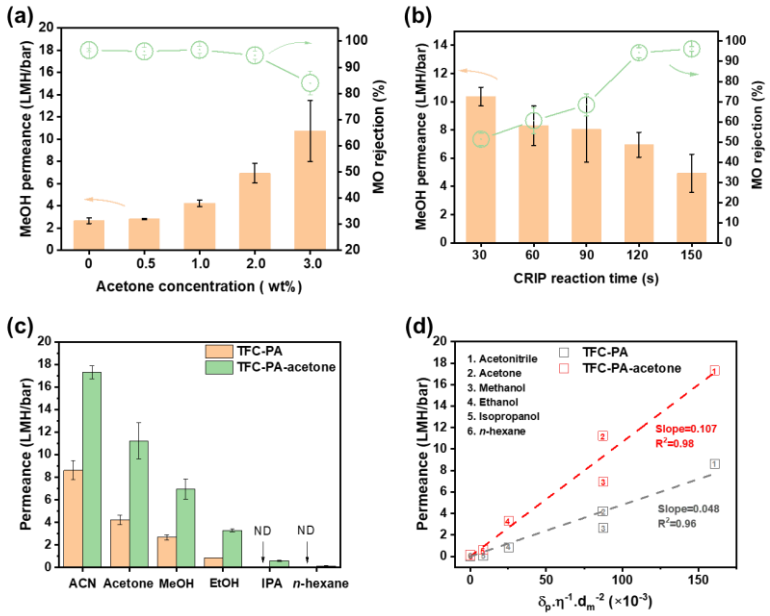

Fig. 2.10. (a) Pure permeance of various organic solvents through the TFC-PA-acetone and TFC-PA membranes. (ND: not detectable) (b) Plot of solvent permeance with the combined solvent property (viscosity: η, molar diameter: d_m, and Hansen solubility parameter due to the polar attraction: δ_p) for the TFC-PA membrane and TFC-PA-acetone membrane.

Table 2.4. Properties of solvents used for nanofiltration tests.

Name	Molar volume[a] ($cm^3\ mol^{-1}$) at 25 °C	Molar diameter (nm)	Hansen Solubility parameter[a], δ_P ($MPa^{1/2}$) at 25 °C	Viscosity[b] (*10^{-3} pa • s) at 25 °C
Acetone	74.0	0.62	10.4	0.31
Acetonitrile	52.6	0.55	18.0	0.37
Methanol	40.7	0.51	12.3	0.54
Ethanol	58.5	0.57	8.8	1.07
IPA	76.8	0.62	6.8	2.04
Hexane	131.6	0.75	0.0	0.29

[a] Taken from Hansen Solubility Parameters: A User's Handbook, 2nd Edition, Charles M. Hansen, CRC Press, Boca Raton, FL, 2007.

[b] Taken from the CRC Handbook of Chemistry and Physics, 85th Edition, David R. Lide, ed., CRC Press, Boca Raton, FL, 2004.

The rejection of the TFC-PA and TFC-PA-acetone membranes in methanol was evaluated using various dye molecules such as MO, RDB, BBR, and RB (**Table 2.5**). The results (**Fig. 2.11a**) show that the TFC-PA and TFC-PA-acetone membranes had similarly high rejection rates (over 94.6%) for MO dye (327 g mol^{-1}). This further indicates that the TFC-PA membrane prepared using the ARIP method was defect-free. Additionally, the long-term separation performance of the TFC-PA-acetone membrane in an MO/MeOH solution was investigated to demonstrate the practicability of the membrane and the possible dye separation mechanism. The results (**Fig. 2.11b**) show that the TFC-PA-acetone membrane maintained high solvent permeance and a high rejection rate of MO during a 30 h OSN test, suggesting that the dye separation mechanism of the membrane was rejection rather than solute adsorption [64, 68, 70]. Because, if the mechanism of dye separation by the membrane is adsorption, once the adsorption of the dye to the membrane reaches saturation, it will not be able to separate the dye solution.

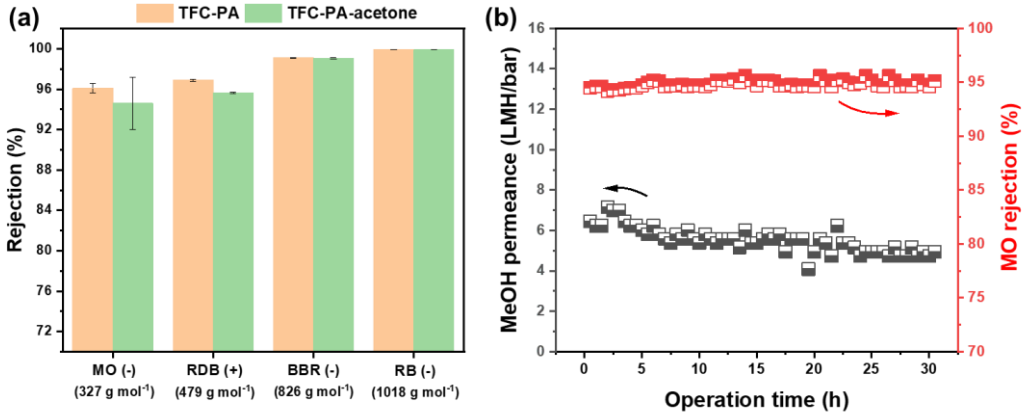

Fig. 2.11. (a) Dye rejections of the TFC-PA-acetone membrane and the TFC-PA membrane in MeOH. (b) Long-term filtration performance of the TFC-PA-acetone membrane for MO/MeOH mixture solution.

Table 2.5. Chemical structures, molecular weights and UV-vis absorption peak of various dyes used in this work.

Dyes	M_W (g mol^{-1})	Chemical structure	3D molecular structure	charge	UV-vis absorption peak (nm)
Methyl orange （MO）	327	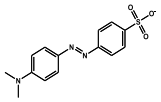		-	422
Rhodamine B （RDB）	479	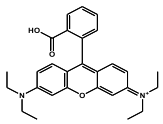	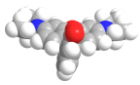	+	545
Brilliant Blue R （BBR）	826	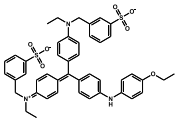	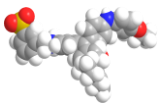	-	588
Rose bengal （RB）	1018	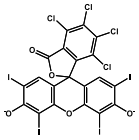		-	556

The methanol permeance and small-sized solute (⩽327 g mol^{-1}) rejection of the TFC-PA-acetone membrane were compared with those of other polymeric OSN membranes reported in the literature, as shown in **Fig. 2.12**. The TFC-PA-acetone membrane exhibited superior or comparable perm-selectivity to the previously

investigated OSN membranes, which include TFC-PA membranes (with DMF activation) [30, 60, 63], thin film nanocomposite PA (TFN-PA) membranes (with nanomaterials) [91, 104, 105], and TFC polyarylate (TFC-PAR) membranes (with special structure monomers) [65, 68-70] (**Table 2.6**). As compared to other methods for improving the performance of OSN membranes, the ARIP method has the advantages of simple operation, high efficiency, and easy integration with existing production processes. This is a promising way for achieving industrial production of high-performance TFC OSN membranes.

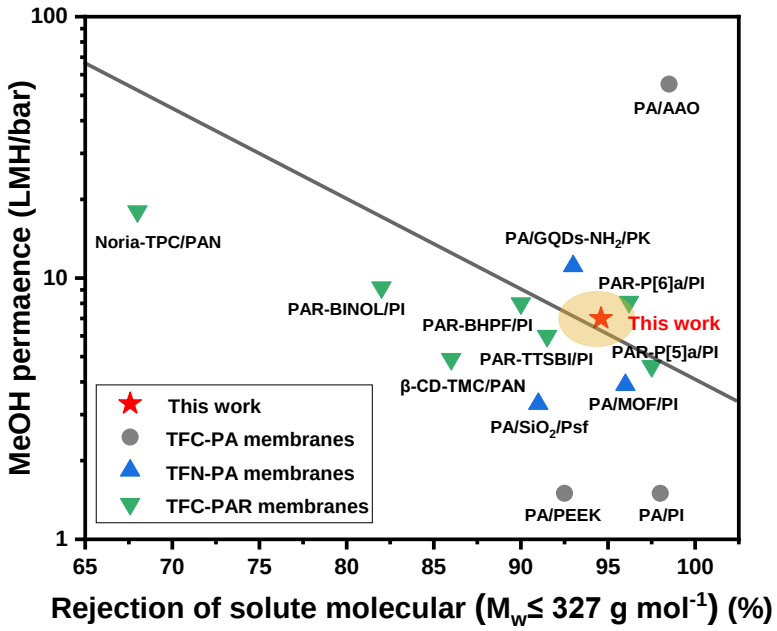

Fig. 2.12. Performance comparison of the TFC-PA-acetone membrane with previously reported OSN membranes in literature. (Solutes with a molecular weight lower than 327 g mol^{-1} were selected)

Table 2.6. Detailed information about the reported membranes shown in Fig. 2.12.

Membrane types	Membrane material	Notes about the fabrication method	Support	MeOH permeance (L m^{-2} h^{-1} bar^{-1})	Solute M_W (g mol^{-1})	Rejection (%)	Ref.
TFCs-PA	MPD/TMC	ARIP	PK	7.0	Methyl orange /327	94.6	This work
	MPD/TMC	With DMF activation	PI (XP84)	1.5	Polystyrene/ 236	98.0	[60]
	MPD/TMC		PEG-PEEK	1.5	Polystyrene/ 236	92.5	[63]
	MPD/TMC		AAO	52.5	NHSA/246	98.5	[30]
TFNs-PA[a]	MPD/TMC /MOFs	With nanomaterials	PI (XP84)	3.9	Polystyrene/ 236	96.0	[104]
	PIP/TMC /SiO_2		Psf	3.3	Methyl orange /327	91	[105]
	MPD/TMC /GQDs-NH_2		PDA-PK	11.1	Methyl orange /327	93	[91]
TFCs-PAR[b]	β-CD-TMC	With special structure monomer	PI (Matrimid)	4.9	Methyl orange /327	86.0	[106]
	Noria-TPC		PAN	18.0	Methyl orange /327	68	[69]
	PAR-TTSBI		PI (XP84)	6.0	Disperse red/314	91.5	[72]
	PAR-BHPF			8.0	Disperse red/314	90.0	
	PAR-BINOL			9.2	Methyl orange /327	82.0	[70]
	PAR-P[6]a			8.1	Methyl orange /327	96.2	[68]
	PAR-P[5]a			4.6	Methyl orange /327	97.5	

[a]TFNs-PA : Thin film nanocomposite polyamide membranes

[b]TFCs-PAR : Thin film composite polyarylate membranes

2.4 Conclusions

In this chapter, a high-performance TFC-PA OSN membrane with a 3D honeycomb-like structure on porous PK supports was developed by regulating the IP process with acetone as an organic co-solvent. The experimental results emphasized that acetone regulation and sufficient MPD supply through PK supports during the IP

process were the necessary conditions for the formation of a honeycomb-like structured PA layer. Both the experimental and MD simulation results confirmed that the acetone co-solvent enlarged the IP reaction zone and greatly promoted the convective diffusion of MPD and TMC, leading to a more vigorous IP reaction. The increased heat release led to aggravated vaporization of acetone, which facilitated the formation of a 3D honeycomb-like structure of the PA layer. Such a 3D honeycomb-like structure endowed the TFC-PA-acetone membrane with an ultrahigh specific surface area. Compared with the TFC-PA membrane prepared by the conventional IP method, the optimized TFC-PA-acetone membrane demonstrated 2.6 times higher MeOH solvent permeance (7.0 LMH/bar) and comparable MO selectivity (94.6%). This work explored the underlying mechanism of acetone co-solvents in IP reactions, providing new ideas for tailoring the membrane morphology and separation properties for high-efficiency organic solvent nanofiltration.

Chapter 3: Surface polarity modulation enables high-performance polyamide membranes for separation of polar/non-polar organic solvent mixtures

3.1 Introduction

Separation and recovery of organic liquid mixtures are essential in modern industry and environmental preservation [1-4]. However, the complexity of organic liquid mixtures, characterized by intricate compositions and similar physical and chemical properties, poses a significant challenge. Nowadays, conventional processes, such as distillation and direct combustion, while effective, suffer from high energy consumption and waste generation, impeding sustainability goals [2]. In contrast, membrane-based separation strategies, such as organic solvent reverse osmosis (OSRO) and pervaporation (PV), have been demonstrated as potential approaches for treating organic liquid mixtures by exploiting differences in molecular chemical properties or sub-nanometer pores[4, 10, 107-111]. Unfortunately, PV remains an energy-intensive separation process [110]. Therefore, there is an urgent need to develop high-performance OSRO membrane technology for the separation of organic liquid mixtures.

Polyamide (PA) membranes prepared by interfacial polymerization (IP), widely used in seawater desalination[112, 113], are considered ideal OSRO membranes due to their high selectivity, processability and scalability, and excellent solvent resistance[30]. While conventional PA membranes often demonstrate preferential permeation of polar solvents and rejection of non-polar ones, the PA OSRO composite membranes have limited selectivity for polar/non-polar liquid mixtures[55, 83, 114, 115]. To improve separation efficiency, researchers have attempted to increase the density of PA membranes by implementing a two-step heating process and raising the

temperature of the aqueous solution during the IP process [54, 55]. These methods inevitably sacrifice the permeability of the PA membrane. Although the resulting membranes show improved separation performance, the ideal permselective performance is still desired.

Generally, a transmembrane transport in dense polymer membranes is considered to follow a solution-diffusion model [116]. In OSRO, when separating organic liquid mixtures with similar molecule size, the mechanism of molecular transport across the membrane is primarily determined by the affinity of the molecule to the membrane rather than by the size of the molecule [10, 114, 117, 118]. Therefore, the interaction between solvent, solute, and membrane significantly impacts the selective separation performance of the OSRO membrane. For example, when separating polar/non-polar organic liquid mixtures, the interaction between polar solvents and PA membranes is higher than that between non-polar solvents and PA membranes. This difference allows polar solvents to preferentially penetrate through the PA membrane [30, 55, 114, 119].

Here, a physical surface modification method for high-surface-polarity PA membrane construction was introduced by applying a coating of Fe^{3+} and tannic acid (Fe^{3+}/TA) complex on the surface of the PA membrane, to enhance the polarity of the PA membrane surface. The enhanced surface polarity of the membrane increases the interaction disparity between polar and non-polar solvents and the membrane. It also forms a polarization layer on the membrane surface to weaken the concentration polarization effect on the membrane surface, thereby enhancing the OSRO separation performance. Additionally, the concept of partial flux was proposed to gain a better understanding of the pressure, concentration dependence, and sensitivity of separation performance in the OSRO process. This will serve as a valuable reference for comprehending the mass transfer process in OSRO in greater depth. This study illustrates the role of the surface polarity of the PA membrane in the separation of polar/non-polar organic mixtures and emphasizes the significance of the interaction between the components of the organic solvent mixture and the polymer membrane in

the OSRO process.

3.2 Experimental

3.2.1 Materials

Polyimide (Lenzing P84) polymer particles (Granlat/SG, 100000 g mol^{-1}) were purchased from Ensinger Sintimid GmbH (Linz, Austria). 1,6-hexanediamine (HDA, 99%) was supplied by Tokyo Chemical Industry (Tokyo, Japan) and used for cross-linking the polyimide substrates. *m*-Phenylenediamine (MPD, 99.0%) and 1,3,5-benzenetricarbonyl trichloride (TMC, 98.0%), purchased from Sigma-Aldrich (St. Louis, MO, USA), were used for fabrication of the polyamide layer *via* IP process. Ferric chloride ($FeCl_3$) was obtained from Sigma-Aldrich (St. Louis, MO, USA). Tannic acid (TA) and other organic solvents (e.g., acetonitrile (AcN), methanol (MeOH), acetone, ethanol (EtOH), isopropyl alcohol (IPA), toluene, hexane) used in this study were purchased from FUJIFILM Wako Pure Chemical (Osaka, Japan). Deionized (DI) water was produced using a Milli-Q ultrapure water system (Merck Millipore, Billerica, MA, USA).

3.2.2 Preparation of the control and Fe^{3+}/TA-coated thin-film composite (TFC) membranes

The cross-linked P84 polyimide (XP84) ultrafiltration (UF) support membranes were fabricated using the nonsolvent-induced phase separation (NIPS) method and a subsequent substrate cross-linking procedure, as reported in previous reports [68, 70, 72, 120]. The control TFC membranes, designated as XP84-PA, were prepared by conventional IP using MPD and TMC on the XP84 UF membranes (**Fig. 3.1a**). The XP84 membranes were prewetted with a 3.4 wt% aqueous MPD solution for 2 min, followed by drainage of excess solution using a rubber roller. Subsequently, the membrane was air dried for 1 minute before applying a 0.15 wt% TMC/hexane solution was applied onto the MPD-impregnated side for 1 min. Following the removal of excess TMC solution, the nascent membrane underwent post-treatment at

60 °C for 10 min. Prior to further modification, testing, and characterization, the resulting membranes underwent washing with DI water.

The Fe^{3+}/TA-coated TFC membranes, referred to as PA-Fe^{3+}/TA membranes, were prepared by immersing the XP84-PA membranes sequentially in $FeCl_3$ and TA solutions (**Fig. 3.1b**). There is strong hydrogen bonding, hydrophilic interaction, and π-π interaction between TA and PA. Meanwhile, there are unreacted amino groups on the PA membrane, which can react with the phenolic hydroxyl groups on TA to form amide bonds. Therefore, the Fe^{3+}/TA layer can stably bind to the surface of the PA membrane. The XP84-PA membranes were first immersed in a $FeCl_3$ solution in ethanol with a pre-optimized concentration of 0.16 wt% for 3 min. The membrane was then immersed in an aqueous 0.2 wt% TA solution and shaken on a shaker at 100 rpm for 2 min. Finally, the modified membranes were rinsed with DI water several times and stored at 4 °C in the refrigerator until use.

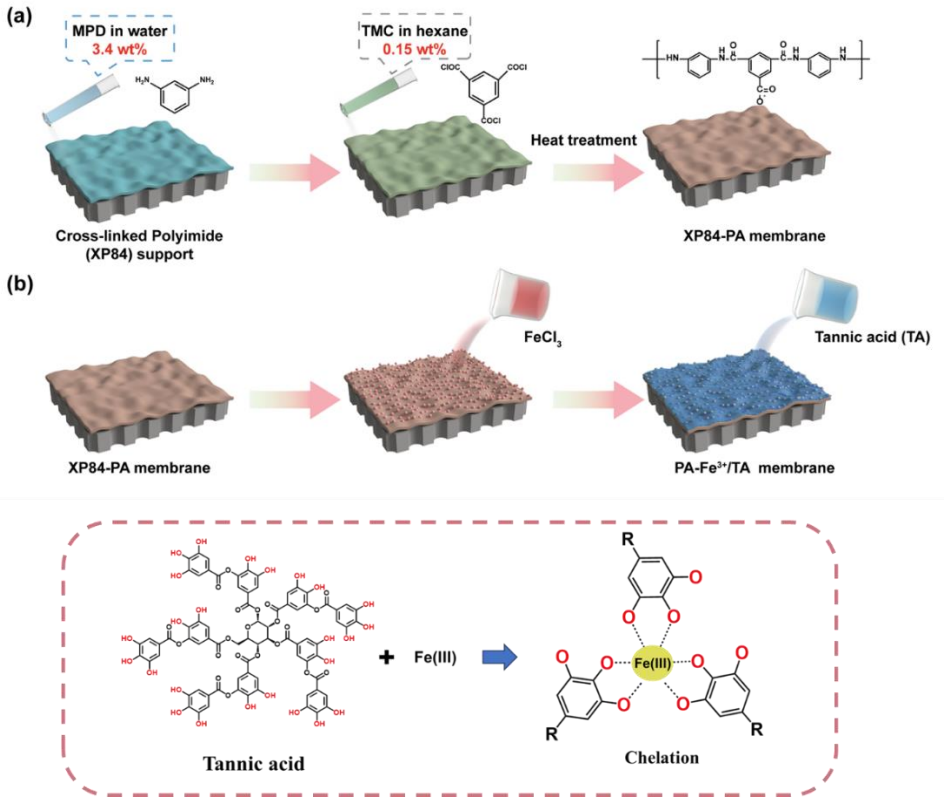

Fig.3.1. Schematic illustration for the fabrication of (a) the XP84-PA membrane and (b) the PA-Fe^{3+}/TA membrane via interfacial polymerization and physical surface

coating method, respectively.

3.2.3 Characterization

The surface element composition and chemical structures of the membranes were analyzed using an X-ray photoelectron spectroscopy with monochromatic Al Kα excitation (XPS, JPS-9010MC, JEOL, Japan) and an attenuated total reflection Fourier transform infrared spectrometer (ATR-FTIR; Alpha, Bruker, USA). The surface and cross-sectional morphologies of the membranes were observed by field-emission scanning electron microscopy (FE-SEM, JSM7500F, JEOL Co. Ltd., Tokyo, Japan). The membranes' surface roughness was evaluated using dynamic force microscopy (tapping mode) with an atomic force microscope (AFM, model SPA-400, Hitachi, Japan). The membrane surface hydrophilicity and polarity were measured using a contact angle analyzer (WCA, DM-300, Kyowa, Japan) with water and Diiodomethane in a droplet volume of 2 μL. A quartz crystal microbalance with dissipative function (QCM-D, Biolin Scientific, Q-Sense Explorer, Sweden) was used to measure the adsorption mass of polar/non-polar solvents on the free-standing membrane to evaluate the interaction between the solvent and the membrane. The free-standing membranes were prepared according to the reported method [30, 70] and loaded onto the chip of QCM-D. All samples were dried in an oven at 45 ℃ overnight before characterization, and all tests were performed at room temperature.

3.2.4 OSRO performance measurement

The OSRO performance, encompassing pure solvent flux, selective separation of organic solvent mixtures, and long-term organic solvent mixture separation stability, was evaluated in a cross-flow filtration system [55, 83, 91, 114, 119]. The membrane was installed in a stainless-steel cell with an effective permeation area: 7.07 cm^2. Performance assessment was conducted under stirring speed of 900 rpm to minimize the possible change in osmotic pressure caused by concentration polarization and an applied pressure gradually increased from 0 to 7 MPa. The feed solution circulated back to the feed container using a plunger pump (NP-FX100 series; FLOM Co., Japan)

at a flow rate of 20 mL min^{-1}. The membrane was pre-compacted in pure MeOH under 7 MPa for at least 12 hours before testing two kinds of organic mixtures, MeOH/hexane (M/Hex) and MeOH/toluene (M/T). MeOH concentration range was fixed between 70 to 100 wt% and the pressure range was 3 to 7MPa. Based on its composition, the azeotropic mixture is denoted as AxBy, i.e., a solution containing 90 wt% MeOH and 10 wt% hexane is denoted as M90Hex10. The composition of permeate and feed solutions were analyzed by Gas chromatography (GC, GC-2014, Shimadzu, Japan) [83]. After the measurement of each mixture, the feed solution was replaced with pure MeOH, and pure MeOH flux was measured again in order to evaluate membrane stability. Solvent flux (J_v, kg m^{-2} h^{-1}) and the separation factor (α) were calculated based on equations (3.1) and (3.2):

$$J_v = \frac{m}{A * T} \tag{3.1}$$

where *m*, *A*, and *T* represent the permeate weight (kg), permeate membrane area (m^2), and permeate time (h), respectively.

$$\alpha_{A/B} = \frac{\chi_{Ap}/\chi_{Bp}}{\chi_{Af}/\chi_{Bf}} \tag{3.2}$$

where χ_{Ap}, χ_{Bp}, and χ_{Af}, χ_{Bf} are molar fractions of component A and component B in the permeate and feed, respectively. All tests were conducted at room temperature, and the reported data represent averages from multiple tests on more than three parallel samples.

3.2.5 Calculation of the partial flux of OSRO membrane in organic mixtures.

The partial flux of component A (J_{mA}, kg m^{-2} h^{-1}) and component B (J_{mA}, kg m^{-2} h^{-1}) in organic mixtures (A/B) can calculated using equations (3.3-3.5):

$$n_{Ap} = \frac{m_{Ap}}{M_A} \tag{3.3}$$

$$m_{Ap} = J_{mA} * s * t \tag{3.4}$$

$$J_m = J_{mA} + J_{mB} \tag{3.5}$$

Where n_{Ap} and n_{Bp} are the moles of component A and component B in the permeate, which can be determined based on the GC test results of the permeate. m_{Ap} is the mass of component A in the permeate, kg. M_A is the molar mass, kg/mol. s is the membrane surface area, m^2. t is the permeate time, h. J_m is the total mass flux of the permeate, kg m^{-2} h^{-1}.

3.2.6 Calculation of the surface energy

Fowkes surface energy theory combines the Young and Young−Dupree equations and dissociates liquid and solid surface energy into its polar and nonpolar (dispersive) components1:

$$\frac{\gamma_l(\cos\theta+1)}{2}=(\gamma_l{}^d)^{1/2}(\gamma_s{}^d)^{1/2}+(\gamma_l{}^p)^{1/2}(\gamma_s{}^p)^{1/2} \qquad (3.6)$$

where $\gamma_l{}^d$ and $\gamma_l{}^p$ are the liquid dispersive and polar components, respectively, and $\gamma_s{}^d$ and $\gamma_s{}^d$ are the solid dispersive and polar components, respectively.

3.2.7 Molecular Dynamics (MD) Simulations

For the MD simulations, the GROMACS 4.67 package and the GROMOS96 force fields were used [121-125]. The membrane of Fe^{3+}/TA and PA were fabricated by the molecule skeleton method, described in our former work. The membrane for PA was comprised by 119 PA skeleton molecules, with dimensions about 10.04116×10.04116×4.50 nm^3. The SPC model was used for water.

To study the interaction energy between different solvent with the membranes was fixed, the membranes were fixed in a simulation box with dimensions about 10.04×10.04×16 nm^3, and 9.40×9.40×16 nm^3. And then, A solvent box (MeOH or hexane) was put on the surface of membrane (Fe^{3+}/TA or PA), respectively. The Ag slabs about 1 nm thickness with dimension in XY directions of simulation box size were put on the solvent slab. Finally, the system was prepared as the order of Ag slab, solvent, membrane, where the Ag slab can prevent the solvent molecules escape. The NVT ensemble was used, which maintained a steady volume (V) and temperature (T, 300 K, Berendsen). The cutoff distance for short-range non-bonded interactions was

chosen to be 12 Å, and the long-range electrostatic coupling and Berendsen bath coupling scheme were employed [126]. The simulations were performed in steps of 2 fs over a period of 2 ns after a full energy minimization using the steepest descent algorithm by the Particle-Mesh Ewald (PME) algorithm [127, 128]. The membrane was fixed and other molecules were allowed to move freely and the LINCS algorithm [129] was used.

To check the concentration effect for MeOH/hexane mixed solvent, three concentrations of MeOH/hexane mixture were made depending on the experimental ratio. The simulation box sizes after equilibrium for the three kinds of mixture were about 9.48×9.48×8.07 nm^3, 7.63×7.63×6.49 nm^3, and 6.75×6.75×5.75 nm^3, respectively. And then, a serial of pressure (3, 5, 7 MPa) was applied to the simulation box. The NPT ensemble was used after the system, which maintained a steady pressure (P) and temperature (T, 300 K, Berendsen). The simulations were performed in steps of 2 fs over a period of 2 ns. After simulation run, density properties were collected.

3.3 Results and discussion

3.3.1 Membrane characterization

Surface morphology, cross-sectional thickness, and surface roughness in the XP84-PA and PA-Fe^{3+}/TA membranes were assessed using SEM and AFM. The SEM surface images (**Fig. 3.2a** and 3.**2d**) revealed that the typical ridge-and-valley structures on the XP84-PA membrane surface were covered mainly by the Fe^{3+}/TA complex. Additionally, SEM results suggest that the peak-and-valley structures on the surface of the XP84-PA membrane appeared relatively smaller compared to the literature description, [130, 131] facilitating the filling of the valleys within the PA structure by the Fe^{3+}/TA complex. SEM cross-sectional analysis (**Fig. 3.2b** and 3.**2e**) indicated that the Fe^{3+}/TA coating layer was very thin. AFM images (**Fig. 3.2c** and **3.2f**) show a decrease in the average roughness value (Ra) of the TFC membrane surface from 48.2 nm to 20.4 nm after coating with the Fe^{3+}/TA complex.

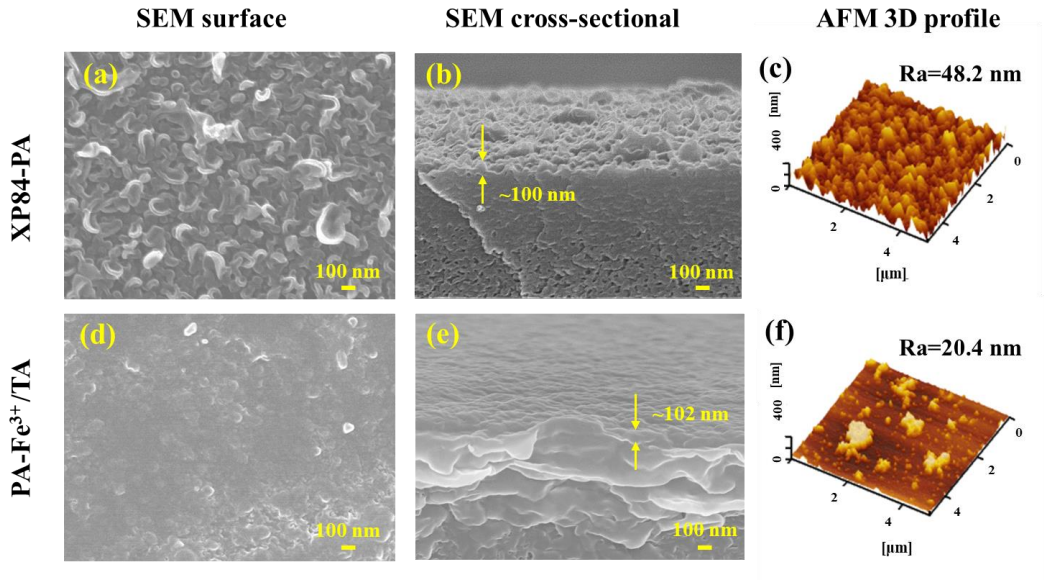

Fig. 3.2. SEM surface, SEM cross-sectional morphologies, and the AFM 3D profile of the (a-c) XP84-PA membrane, (d-f) PA-Fe^{3+}/TA membrane.

ATR-FTIR analysis was performed to characterize the chemical structure changes on the PA membrane surface before and after coating the Fe^{3+}/TA complex. The results (**Fig. 3.3a**) show that the PA- Fe^{3+}/TA membrane exhibits an enhanced peak intensity in the wavenumber range of 3200-3550 cm^{-1}, compared with the XP84-PA membrane. The broad peaks in this wavenumber range can be attributed to the -NH_2 and -OH functional groups in PA and the -OH functional group in TA. XPS characterization was employed to investigate elemental composition changes on the TFC membrane surface before and after Fe^{3+}/TA complex coating. The presence of the Fe 2p characteristic peak around 710 eV (**Fig. 3.3b**) confirmed the successful adsorption of Fe^{3+} on the TFC membrane surface. Chemical element analysis (**Fig. 3.3c** and **3.3d**) revealed that the O/C ratio on the membrane surface increased from 0.348 to 0.632 after coating with the Fe^{3+}/TA complex. This increase is attributed to the higher O/C ratio of TA compared to the PA layer [132]. Furthermore, a lower N 1s content was detected in the PA-Fe^{3+}/TA membrane compared to the XP84-PA membrane. Considering the detection depth of XPS is less than 10 nm [68-70], this result indicates that the Fe^{3+}/TA layer is very thin, which is consistent with the SEM

cross-section results. The FTIR and XPS results confirmed that the Fe^{3+}/TA complex effectively covered the TFC membrane surface.

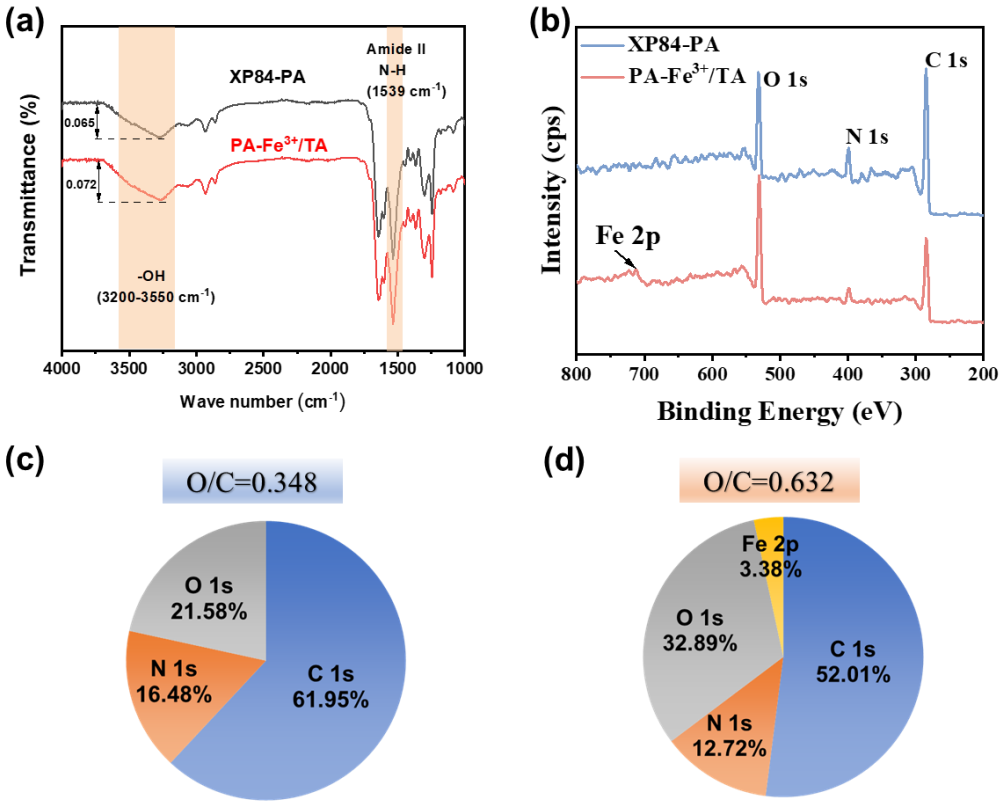

Fig. 3.3. (a) ATR-FTIR spectra of XP84-PA and PA-Fe^{3+}/TA membranes. (b-d) XPS spectra and chemical element composition analysis of XP84-PA and PA-Fe^{3+}/TA membranes.

3.3.2 The effect of coating the Fe^{3+}/TA complex on surface polarity of the TFC membrane

The Fowkes surface energy theory was proposed to quantitatively calculate the polar component of the membrane surface through the Fowkes equation, providing a quantitative measurement method for surface polarity [133, 134]. **Fig. 3.4a** shows the water and diiodomethane contact angles of the XP84-PA and PA-Fe^{3+}/TA membranes, as well as the polar components of the membrane surface energy (γ^p) calculated based on Fowkes surface energy theory (**Table 3.1**). The results showed that compared with the XP84-PA membrane, the water contact angle of the PA-Fe^{3+}/TA membrane

decreased and the diiodomethane contact angle increased. This is attributed to the increase in surface polarity of the PA-Fe^{3+}/TA membrane. At the same time, considering the impact of membrane surface roughness on its liquid contact angle, the relatively small roughness (**Fig. 3.2f**) of the PA-Fe^{3+}/TA membrane surface weakens the impact of increased polarity on the liquid contact angle to a certain extent. For the membrane surface energy (γ^p), the results indicate that the γ^p value increases from 30.6 ± 0.1 mJ/m^2 to 34.6 ± 0.14 mJ/m^2. This signifies an increase in the polarity of the PA membrane surface following the Fe^{3+}/TA complex coating. It is noteworthy that while Fowkes theory may not fully account for the polar contribution of hydrogen bonds, the presence of numerous hydroxyl groups on TA offers ample opportunities for hydrogen bonding, significantly enhancing the polar component of surface energy.

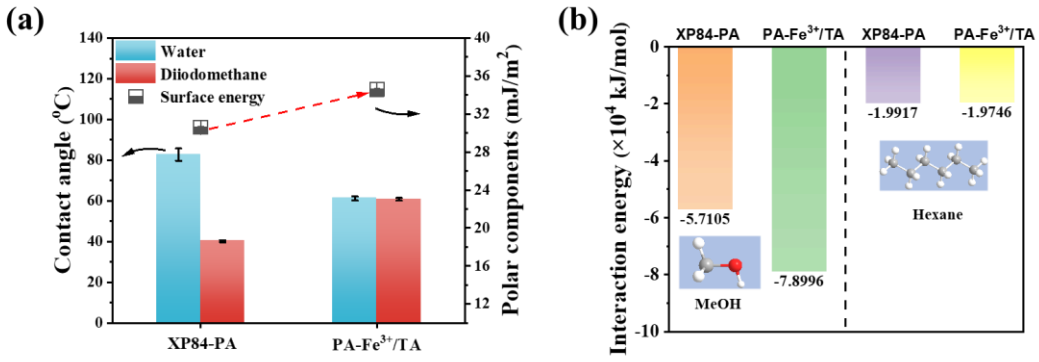

Fig. 3.4. (a) Water, diiodomethane contact angles and polar components of surface energy (γ^p) of XP84-PA and PA-Fe^{3+}/TA membranes. (b) Changes in the interaction energy between XP84-PA and PA-Fe^{3+}/TA membranes and different polar solvents obtained through MD simulation.

Table 3.1. Polar and dispersive surface energy properties (mJ·m^{-2}) of the probe liquids

	γ_l^d	γ_l^p	γ_l
Water	21.8	51	72.8
Diiodomethane	50.8	0	50.8

As shown in **Fig. 3.4b**, the MD simulation results show that after coating with Fe^{3+}/TA complex, the interaction energy between the membrane and the polar solvent

(MeOH) increases, and the interaction energy with the non-polar solvent (hexane) decreases. This implies that the enhancement of membrane surface polarity will be beneficial to the adsorption of polar solvents on the membrane surface, and will be detrimental to the adsorption of non-polar solvents. To evaluate this characteristic, QCM-D was used to test the adsorption behavior of organic solvents on the free-standing membrane surface. The results (**Fig. 3.5a and b**) show that the adsorption mass of the free-standing PA-Fe^{3+}/TA membrane for polar solvents (MeOH) increases and the adsorption capacity for non-polar solvents (hexane) decreases, which is consistent with the MD simulation results. In addition, it was found (**Fig. 3.5c**) that the adsorption mass of the free-standing PA-Fe^{3+}/TA membrane to MeOH/hexane mixed solvent (M90Hex10) was greater than that of the free-standing XP84-PA membrane. This can be explained by the fact that the increase in MeOH adsorption by the free-standing PA-Fe^{3+}/TA membrane was much greater than the decrease in hexane adsorption.

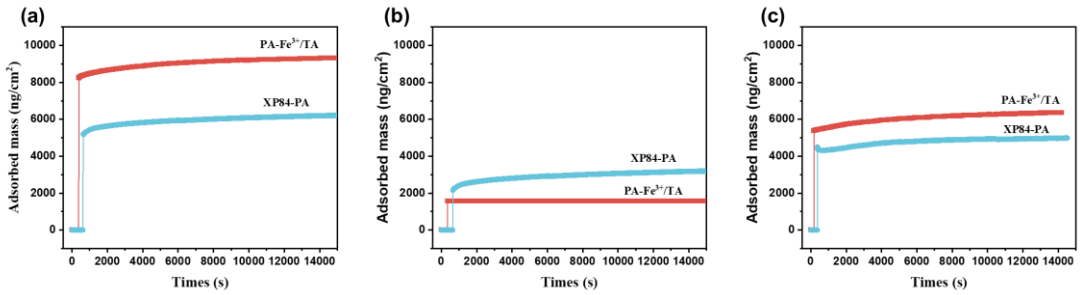

Fig. 3.5. The adsorption mass of (a) MeOH, (b) hexane and (c) M90Hex10 on the membrane surface was obtained by QCM-D.

As is well known, the concentration of feed solution in the OSRO process is very high, usually as high as tens of thousands or even hundreds of thousands of ppm [83, 107, 110, 114]. This will inevitably lead to serious concentration polarization on the membrane surface, thus reducing separation efficiency. Similar to the formation of a hydration layer through hydrophilic modification [135], it is speculated that polar modification on the membrane surface will also form a polarized layer on the membrane surface (**Fig. 3.6a**). Due to the existence of the polarization layer, the

rejected non-polar solvent is difficult to adhere to the membrane surface, thereby reducing its residence time on the membrane surface. Therefore, when separating polar/non-polar mixed liquids, enhancing the polarity of the membrane surface is beneficial to reducing concentration polarization on the membrane surface. Furthermore, the change in concentration polarization on the membrane surface before and after modification was detected by adjusting the cross-flow rate of the feed liquid during the test. As shown in **Fig. 3.6b**, as the cross-flow rate increased, the total flux of both membranes likewise increased, indicating that serious concentration polarization existed on the membrane surface [136]. It is worth noting that the normalized total flux of the XP84-PA membrane was more sensitive to the cross-flow rate than that of the PA-Fe^{3+}/TA membrane, meaning there was a more severe concentration polarization on the XP84-PA membrane surface. The above experimental results show that due to the numerous polar hydroxyl (-OH) groups on TA, the Fe^{3+}/TA coating could increase the polarity of the PA membrane surface. The enhanced membrane surface polarity increased the interaction disparity between polar and non-polar solvents and the membrane, and formed a polarization layer on the membrane surface to weaken the concentration polarization effect on the membrane surface.

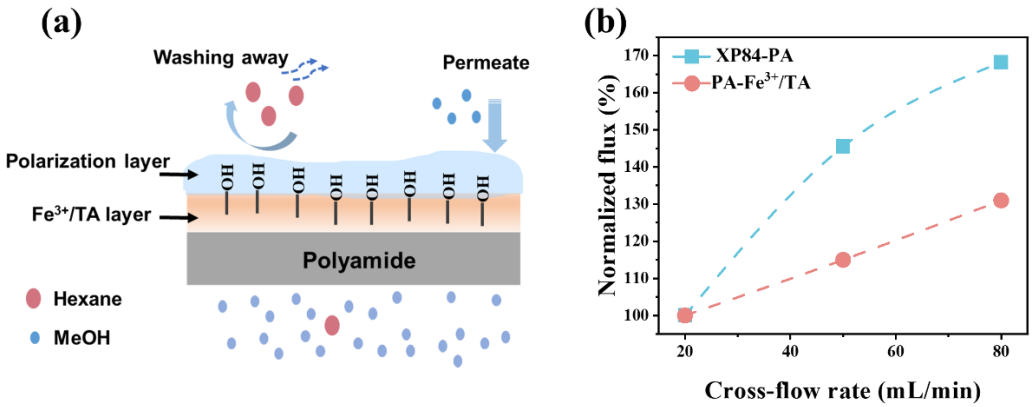

Fig. 3.6. (e) Schematic illustration of the mechanism by which the polarization layer weakens concentration polarization. (f) Cross-flow-rate sensitivity of the normalized M90Hex10 flux of the XP84-PA and PA-Fe^{3+}/TA membrane. These experiments were conducted at an operating pressure of 7 MPa.

3.3.3 OSRO performances

Fig. 3.7a illustrates the pure MeOH flux as a function of applied pressure for the PA-Fe^{3+}/TA membrane prepared under optimal conditions. The results indicate that the pure MeOH flux of the PA-Fe^{3+}/TA membrane maintained a consistent linear relationship with pressure during the decrease-increase pressure cycle. This suggests that the membrane exhibited stability and excellent swelling resistance during these operational cycles. **Fig. 3.7b** shows the pure solvent flux of XP84-PA and PA-Fe^{3+}/TA membranes in organic solvents with various polarities. Due to the polarity of the PA layer, both membranes exhibit a preference for selectively permeating solvents characterized by high polarity, low viscosity, and small molar diameter, such as AcN, MeOH, and acetone (**Table 3.2**). The flux of IPA was nearly zero due to its high viscosity and large molar diameter. In the case of non-polar solvents like toluene and hexane, no permeability was observed. Notably, the PA-Fe^{3+}/TA membrane exhibited a significantly higher permeation flux compared to the XP84-PA membrane. For instance, the AcN, MeOH, and acetone flux values increased from 8.18 kg m^{-2} h^{-1}, 11.6 kg m^{-2} h^{-1}, and 1.49 kg m^{-2} h^{-1} to 15.4 kg m^{-2} h^{-1}, 17.7 kg m^{-2} h^{-1}, and 2.67 kg m^{-2} h^{-1}, respectively. This improved permeation performance is attributed to the enhanced surface polarity of the PA-Fe^{3+}/TA membrane, which strengthens the interaction between the membrane and the polar solvent. This facilitates the reduction of the adsorption energy barrier of the polar solvent, thereby reducing the permeation resistance [137]. The above results showcase the positive impact of surface modification on polar solvent penetration.

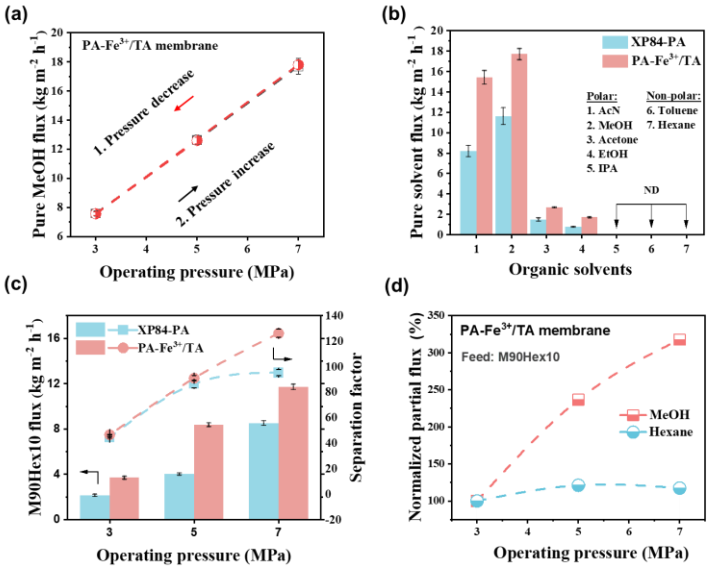

Fig. 3.7. (a) Pure MeOH flux as a function of operating pressure. The pressure was initially decreased from 7 to 3 MPa and subsequently increased from 3 to 7 MPa. (b) Pure solvent flux of XP84-PA and PA-Fe^{3+}/TA membranes in organic solvents of different polarities at 7MPa (ND: not detectable). (c) M90Hex10 flux and separation factors of XP84-PA and PA-Fe^{3+}/TA membranes under different operating pressures. (d) Pressure sensitivity of the normalized partial flux of MeOH and hexane of PA-Fe^{3+}/TA membrane when permeating M90Hex10 liquid mixture.

Table 3.2. Properties of solvents used for nanofiltration tests.

Name	Molar volume[a] (cm^3 mol^{-1}) at 25 °C	Molar diameter (nm)	Hansen Solubility parameter[a], δ_P ($MPa^{1/2}$) at 25 °C	Viscosity[b] (cP) at 25 °C
Acetone	74.0	0.62	10.4	0.31
Acetonitrile	52.6	0.55	18.0	0.37
Methanol	40.7	0.51	12.3	0.54
Ethanol	58.5	0.57	8.8	1.07
IPA	76.8	0.62	6.8	2.04
Toluene	106.8	0.70	1.4	0.59
Hexane	131.6	0.75	0.0	0.29

[a] Taken from Hansen Solubility Parameters: A User's Handbook, 2nd Edition, Charles M. Hansen, CRC Press, Boca Raton, FL, 2007.

[b] Taken from the CRC Handbook of Chemistry and Physics, 85th Edition, David R. Lide, ed., CRC Press, Boca Raton, FL, 2004.

Polar/non-polar organic liquid mixtures find widespread use in practical industrial applications [54, 138, 139], and the separation and recovery of such mixtures have substantial economic benefits and contribute to reducing environmental pollution. A prime example is the separation of hexane and MeOH, a process vital in MeOH synthesis to overcome thermodynamic and heat transfer limitations. Hexane addition enhances the single-pass conversion rate of carbon monoxide (CO) to 90%, yielding significant economic and societal benefits [139, 140]. Separating a MeOH/hexane mixture, especially in the presence of azeotropes, poses a considerable challenge, making the polar characteristics of the PA membrane an ideal choice for such applications.

In this study, the OSRO performance of TFC membranes was assessed focusing on the selective separation of MeOH/hexane organic liquid mixtures. Similar to other pressure-driven processes, the membrane separation performance in OSRO is closely linked to transmembrane pressure [83, 110, 114]. **Fig. 3.7c and Table 3.3** illustrate the M90Hex10 flux and separation factor values of XP84-PA and PA-Fe^{3+}/TA membranes under different operating pressures. The results demonstrate that, in the pressure range of 3-7 MPa, the PA-Fe^{3+}/TA membrane exhibited higher M90Hex10 flux and separation factor compared to the XP84-PA membrane, overcoming the conventional trade-off effect. Specifically, at an operating pressure of 7 MPa, the M90Hex10 flux of the PA-Fe^{3+}/TA membrane reached 11.7 kg m^{-2} h^{-1}, with a separation factor of 126. This represents a 37.6% increase in flux and 32.4% increase in the separation factor compared to the XP84-PA membrane. As mentioned above, the improved permeation selectivity properties of the membrane is attributed to enhanced surface polarity, which increased the interaction difference between polar and non-polar solvents with the membrane. In addition, during the OSRO process, the enhanced surface polarity is conducive to the formation of a polarization layer to weaken the concentration polarization on the membrane surface. In addition, we found that as the pressure increases, the growth rate of the flux of XP84-PA membrane gradually increases, showing a nonlinear trend. This phenomenon may be

attributed to the non-linear increase in the separation factor with pressure (**Fig 3.7c**), resulting in a decrease in the rate of increase in the osmotic pressure difference across the membrane. [141, 142] Ultimately, this leads to an increase in the growth rate of the effective driving force of the membrane, thereby directly affecting the flux change of the XP84-PA membrane.

Table 3.3. Separation factors of XP84-PA and PA-Fe^{3+}/TA membranes by OSRO separation with different weight ratios of methanol/hexane under the specified transmembrane pressure, Δp (MPa), and 25 °C.

	Separation factor of M90Hex10		Separation factor of M80Hex20		Separation factor of M70Hex30	
Δp	XP84-PA	PA-Fe^{3+}/TA	XP84-PA	PA-Fe^{3+}/TA	XP84-PA	PA-Fe^{3+}/TA
3	44.6	46.6	26.2	29.3	12.4	16.4
5	86.5	91.0	80.4	96.2	75.6	124
7	95.3	126	116	146	145	218

M = Methanol; Hex = Hexane

Furthermore, with increasing pressure, the flux and separation factors of PA-Fe^{3+}/TA and XP84-PA membranes in the M90Hex10 mixture exhibit an upward trend. This pressure-dependence of separation performance is consistent with literature reports [83, 110, 114]. Despite its prevalence, there is a notable absence of research aimed at gaining a comprehensive understanding of this phenomenon. Here, the concept of a partial flux is proposed to understand the pressure dependence of separation performance. The partial flux refers to the amount of a certain component passing through the membrane per unit of time, and its value can reflect the difficulty of the component passing through the membrane. The partial fluxes of components in organic mixtures are readily calculated based on separation factor calculation formulas and experimental results (details are in the Supporting Information). It is worth noting that hexane flux cannot be observed in pure solvent tests due to the small interaction of hexane with both membranes (**Fig. 3.4b and Fig. 3.7b**). However, in the MeOH/hexane mixture, MeOH will drag hexane through the membrane when it

permeates due to the interaction between MeOH and hexane [83, 114, 141]. Therefore, the hexane flux can be detected in the MeOH/hexane mixture system. After normalization, the curve of partial flux changing with pressure was obtained (**Fig. 3.7d**). The results indicate that the partial flux of MeOH is more pressure-sensitive than that of hexane. The different responses of each component in MeOH/hexane mixture to pressure can be attributed to the differences in their permeability and permeation modes. As shown in **Fig. 3.8a**, molecules in the MeOH/hexane mixture system are categorized into three types based on their penetration capabilities: MeOH molecules, MeOH-hexane molecular clusters, and hexane molecules. It's worth emphasizing that hexane molecules require the assistance of MeOH to traverse the membrane, typically in the form of MeOH-hexane molecular clusters [83, 114, 141]. With increasing pressure, the driving force for penetration intensifies, hastening the penetration of pure MeOH molecules and MeOH-hexane molecular clusters. However, pure hexane molecules remain unable to penetrate the membrane independently. Consequently, the partial flux of MeOH relies on both MeOH molecules and MeOH-hexane molecular clusters, while the partial flux of hexane solely hinges on the penetration of MeOH-hexane molecular clusters. Therefore, the partial flux of MeOH is more pressure-sensitive than that of hexane. Specifically, when the pressure increased from 3 MPa to 7 MPa, the partial flux of MeOH through the PA-Fe^{3+}/TA membrane increased by 218%, while the partial flux of hexane only increased by 17%. Ultimately, the separation factor of the membrane increased from 46.6 to 126. This pressure sensitivity helps us to more intuitively understand the phenomenon that the separation factor increases with pressure. Interestingly, compared with the XP84-PA membrane (**Fig. 3.8b**), the PA-Fe^{3+}/TA membrane exhibited comparable pressure sensitivity of MeOH partial flux and lower pressure sensitivity of hexane partial flux due to enhanced surface polarity. This more profound understanding of the pressure-dependent separation performance contributes valuable insights for optimizing membrane performance in different application scenarios.

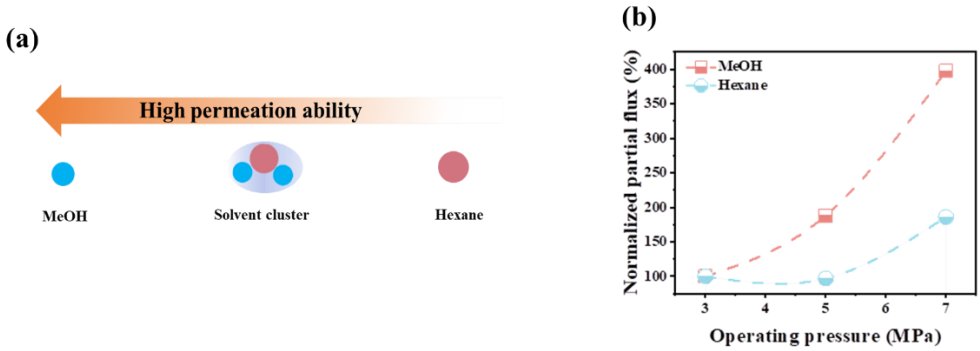

Fig. 3.8. (a) The proposed molecular forms and penetration capabilities in MeOH/hexane mixture. (b) Pressure sensitivity of the normalized partial flux of MeOH and hexane of XP84-PA membrane when permeating M90Hex10 liquid mixture.

In practical applications, the separation and recovery of organic liquid mixtures with varying solute concentrations are common, impacting the performance of OSRO membranes [83]. Therefore, it is crucial to investigate the concentration dependence of membrane separation performance. **Fig. 3.9a** shows the total flux and MeOH/hexane separation factor of XP84-PA and PA-Fe^{3+}/TA membranes across different feed hexane concentrations. Interestingly, with the increasing hexane concentration in the feed, the fluxes of both XP84-PA and PA-Fe^{3+}/TA membranes decreased, while the separation factors increased. Notably, when the hexane concentration increased from 10 wt% to 30 wt%, the MeOH/hexane separation factors of the XP84-PA and PA-Fe^{3+}/TA membranes increased from 95.3 and 126 to 145 and 218, respectively. This phenomenon of increasing separation factor with increasing solute concentration is contrary to the commonly held view that the separation factor decreases with solute concentration in the OSRO process [83, 110, 114]. To eliminate membrane influence, the influence of concentration was verified using the more commonly used MeOH/toluene separation system (**Fig. 3.9b and Table 3.4**), showing consistency with prior literature trends [54, 83, 110, 114]. This implies that the difference in separation behavior is mainly influenced by the use of the MeOH/hexane feed solution. At the same time, it was observed that the separation factor of the PA-Fe^{3+}/TA membrane is smaller than that of the XP84-PA membrane. This is because the π-π interaction between toluene and the benzene ring on TA increases the permeability

of toluene.

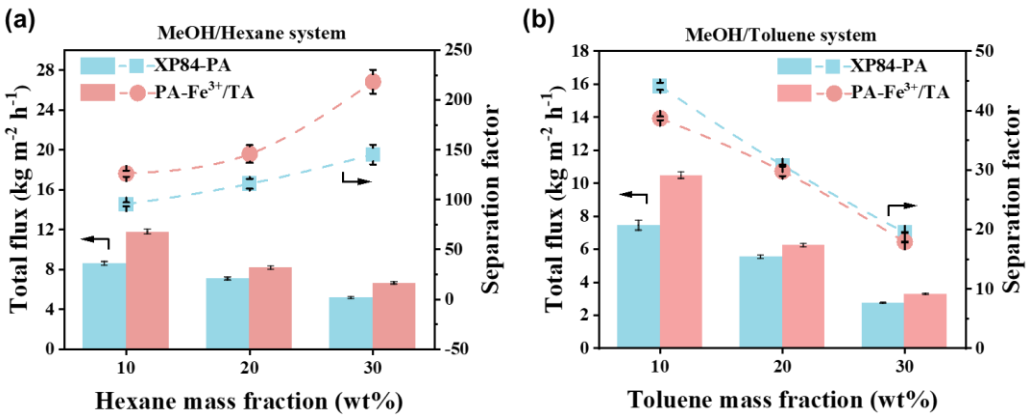

Fig. 3.9. (a, b) Total flux and separation factors of XP84-PA and PA-Fe^{3+}/TA membranes under feed solutions with varying hexane and toluene concentrations.

Table 3.4. Separation factors of XP84-PA and PA-Fe^{3+}/TA membranes by OSRO separation with different weight ratios of methanol/toluene under the specified transmembrane pressure, Δp (MPa), and 25 °C.

	Separation factor of M90T10		Separation factor of M80T20		Separation factor of M70T30	
Δp	XP84-PA	PA-Fe^{3+}/TA	XP84-PA	PA-Fe^{3+}/TA	XP84-PA	PA-Fe^{3+}/TA
3	19.3	19.2	4.5	4.5	3.9	3.6
5	34.4	32.8	16.9	16.5	6.5	6.3
7	44.1	38.7	30.8	29.8	19.5	17.9

M = Methanol; T = Toluene

Considering that MeOH/hexane is not a completely miscible system, the unusual concentration dependency of the MeOH/hexane separation system might stem from micro-phase separation phenomena [143, 144]. **Fig. 3.10** shows the proposed mechanism for the enhanced separation of MeOH/hexane mixture. Under pressure, a fraction of the MeOH/hexane mixture in the high-hexane concentration regime will undergo a transition from large solvent clusters to small solvent clusters, or even completely separate into individual MeOH and hexane molecules. Because hexane molecules cannot permeate the PA membrane on its own, it requires the assistance of

MeOH to permeate the PA membrane [83, 114]. Therefore, while neglecting the increase in osmotic pressure difference caused by the concentration increase, when the mixed system undergoes micro-phase separation, the relative amount of hexane that can permeate the PA membrane will decrease, and the relative amount of MeOH that can permeate the PA membrane will increase. This will lead to an increase in the separation factor of the MeOH/hexane mixture. To delve into this mechanism, the distribution of MeOH and hexane was simulated under different pressures in mixed liquids with various concentrations. Results (**Fig. 3.11**) indicate that as the hexane concentration increases to 20 wt%, the density distributions of MeOH and hexane began to fluctuate, indicating that micro-phase separation occurs in the mixed liquid. Further increasing the hexane concentration to 30 wt%, the micro-phase separation phenomenon becomes more severe.

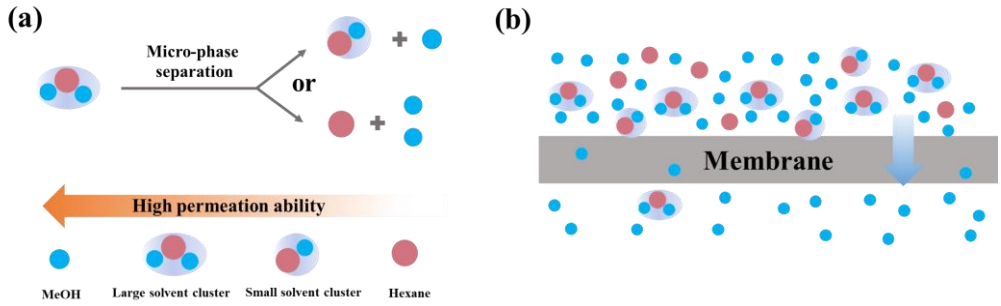

Fig. 3.10. The proposed mechanism for the enhanced separation factor of MeOH/hexane mixture.

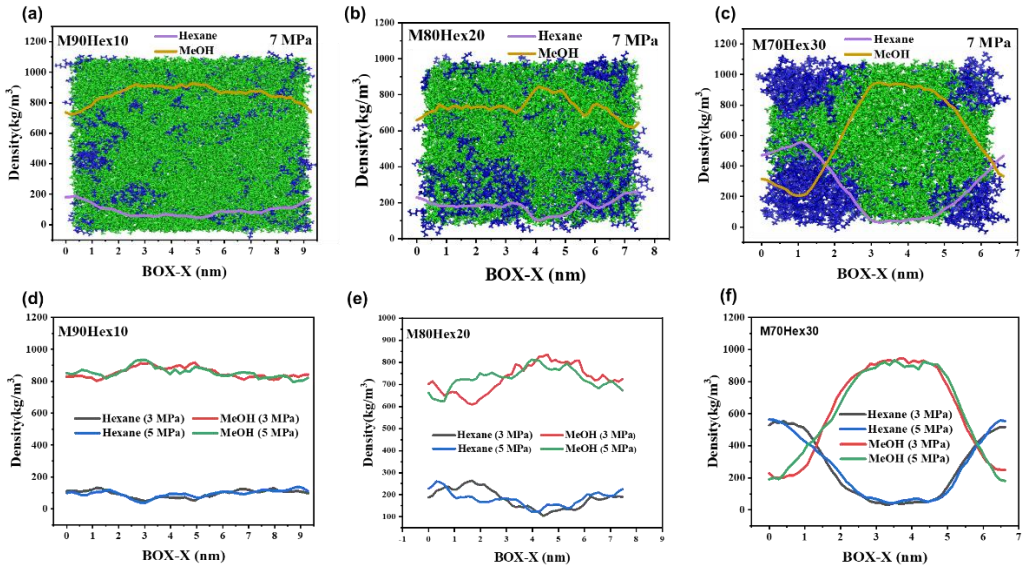

Fig. 3.11. The simulation of the distribution of MeOH and hexane under 7 MPa pressure in mixed liquids of (a) M90Hex10, (b) M80Hex20 and (c) M70Hex30. (Blue: hexane; green: MeOH). The simulation of the distribution of MeOH and hexane under 3 MPa and 5 MPa pressure in mixed liquids of (d) M90Hex10, (e) M80Hex20 and (f) M70Hex30.

Similarly, analyzing partial fluxes for mixture components sheds light on concentration dependence of separation performance. In the MeOH/hexane system, both MeOH and hexane partial fluxes are influenced by hexane concentration, but hexane partial flux exhibits greater concentration sensitivity (**Fig. 3.12a**). Consequently, the MeOH/hexane separation factors demonstrate an upward trend with increasing hexane concentration. Conversely, different from the immiscible system of MeOH/hexane, MeOH/toluene is a completely miscible system and will not produce micro-phase separation [143, 144]. Therefore, in the MeOH/toluene system, MeOH partial flux exhibits higher sensitivity to concentration (**Fig. 3.12b**), resulting in decreased MeOH/toluene separation factors with increasing toluene concentration. These findings further support the notion that micro-phase separation in the MeOH/hexane system drives its unique concentration dependency.

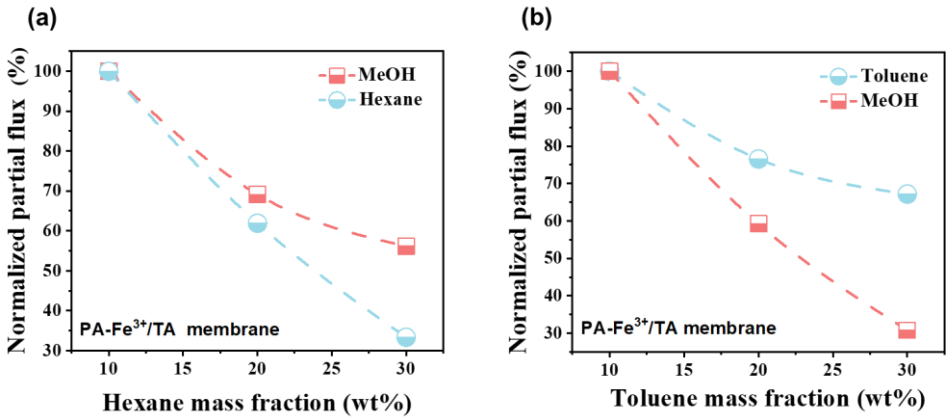

Fig. 3.12. Concentration sensitivity of the normalized partial flux of the PA-Fe^{3+}/TA membrane for (a) M90Hex10 and (b) M90T10 feed solution. These experiments were conducted at an operating pressure of 7 MPa.

Ensuring long-term stability of PA-Fe^{3+}/TA membranes is crucial for practical applications involving organic solvents. Continuous permeation experiments were conducted using M90Hex10 at 7 MPa operating pressure demonstrated stable separation performance and excellent swelling resistance over 28 days of continuous testing (**Fig. 3.13a**).

The performance of the PA-Fe^{3+}/TA membrane in the separation of MeOH/hexane mixture was compared with recently reported membranes, such as polyketone-supported PA membrane (PK-RO) [83] and PK-RO membrane subjected to a two-step heat treatment (A130W95) [54] (**Fig. 3.13b** and **Table 3.5**). The PA-Fe^{3+}/TA membrane exhibited higher flux and superior MeOH/hexane separation performance compared to earlier reported membranes [54, 83]. In the case of separating MeOH/toluene mixtures (**Fig. 3.13c** and **Table 3.6**), the PA-Fe^{3+}/TA membrane outperformed other reported OSRO membranes, showing a separation factor approximately four times higher than most membranes and increased permeability [54, 55, 83, 110, 114]. These suggest that the inherent permeability and selectivity trade-off effect could be overcome through a simple surface polarity modification approach.

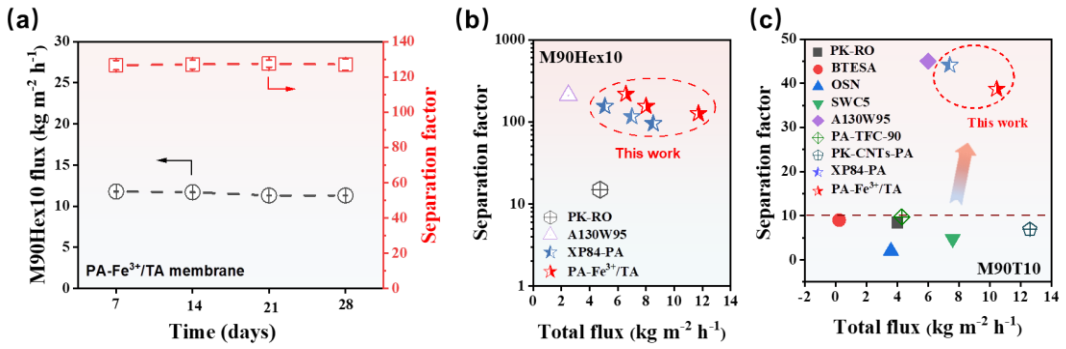

Fig. 3.13. Long-term stability of PA-Fe^{3+}/TA membrane tested under 7 MPa with M90Hex10 as the feed solution (a). Performance comparison of our membranes with the state-of-the-art OSRO membranes using (b) M90Hex10, and (c) M90T10 as the feed solution.

Table 3.5. Comparison of the separation performance between literatures and this work for methanol/hexane.

Membrane	Hexane in feed [wt%]	Operating pressure [MPa]	Total flux [kg m^{-2} h^{-1})]	Separation factor [-]
A130W95[54]	10	3	2.50	210
PK-RO[83]	10	3	4.74	14.9
XP84-PA (This work)	10	7	8.52	95.3
	20	7	7.00	116
	30	7	5.09	145
PA-Fe^{3+}/TA (This work)	10	7	11.72	126
	20	7	8.10	146
	30	7	6.58	218

Table 3.6. Comparison of the separation performance between literatures and this work for methanol/toluene.

Membrane	Toluene in feed [wt%]	Operating pressure [MPa]	Total flux [kg m^{-2} h^{-1})]	Separation factor [-]
BTESA[110]	10	18	0.24	9.00
PK-RO[83]	10	3	4.03	8.40
OSN[83]	10	3	3.6	2.00
SWC5[83]	10	3	7.6	4.80
A130W95[54]	10	3	6.0	45.0
PA-TFC-90[55]	10	3	4.3	9.76
PK-CNTs-PA[114]	10	3	12.6	6.90
XP84-PA (This work)	10	7	7.41	44.1
PA-Fe^{3+}/TA (This work)	10	7	10.45	38.7

3.4 Conclusions

This study successfully developed a high-performance OSRO membrane with enhanced surface polarity by coating a layer of Fe^{3+}/TA complex on the surface of the PA membrane. Experimental and simulation results highlight that enhanced surface polarity of the membrane increased the interaction disparity between polar and non-polar solvents and the membrane, and formed a polarization layer on the membrane surface, thereby weakening the concentration polarization effect on the membrane surface. Consequently, the PA-Fe^{3+}/TA membrane exhibited improved permeability and selectivity, breaking the inherent trade-off effect associated with PA membranes. In addition, the concept of partial flux was proposed to further understand the pressure, concentration dependence and sensitivity of separation performance in the OSRO process. This provides valuable reference for in-depth understanding of the OSRO

mass transfer process.

This work underscores the significance of further research into the mass transfer mechanisms of the OSRO process, particularly in understanding the interactions between components of the organic mixtures and the membrane. Optimizing and regulating the interactions are identified as crucial factors on improving separation efficiency. Overall, the findings contribute a simple and practical method for developing high-performance OSRO membranes and enhance the understanding of the role of PA membranes in the separation of polar/non-polar liquid mixtures.

Chapter 4: Surface repair engineering of polyamide membranes for high-performance organic solvent reverse osmosis

4.1. Introduction

Organic solvent separation and purification technology is an important foundational technique in industries such as chemical engineering and pharmaceuticals. It holds vast prospects for applications in environmental protection and resource utilization [1-4]. However, conventional methods for handling organic solvents, such as distillation and chemical adsorption, often require substantial energy and chemical inputs, resulting in resource wastage and the generation of chemical waste [2]. In contrast, membrane separation technology, which employs porous or selectively permeable thin films to selectively separate organic solvents, reducing waste generation and saving approximately 90% of energy consumption in chemical separation processes [4], has gained prominence due to its efficiency, sustainability, and environmentally friendly attributes [10, 109, 110].

Currently, membrane-based organic solvent separation processes can be roughly divided into three categories: organic solvent nanofiltration (OSN), pervaporation (PV), and organic solvent reverse osmosis (OSRO) [10, 110]. Although research on OSN is increasing, it is difficult to use OSN membrane to separate organic liquid mixtures (such as alkanes, alcohols, aromatics, and cyclic alkanes) [10]. PV can separate organic liquid mixtures, but is still an energy-intensive process [110]. Compared with OSN and PV, OSRO can provide smaller pore size (<0.5 nm) and lower energy consumption to separate organic liquid mixtures, which is an ideal process to separate organic liquid mixtures. Therefore, the development of high-performance OSRO membranes is of great significance and urgent.

Polyamide (PA) membranes are considered ideal OSRO membrane materials due

to their high perm-selectivity, excellent processability and scalability, and excellent solvent resistance. Recent efforts by researchers have involved the development of polyketone-supported polyamide (PK-PA) composite membranes on solvent-resistant PK ultrafiltration substrates for OSRO applications [55, 83, 114, 115]. Despite their contribution to the development of OSRO membranes, these composite membranes still exhibit limited selectivity. For example, the separation factor of a methanol/toluene mixed liquid with a mass fraction ratio of 90/10 is less than 12. The relatively low selectivity of interfacial polymerization-prepared PA membranes may be attributed to their wide pore size distribution. Therefore, constructing PA membranes with small pores and narrow pore size distribution is crucial for enhancing their OSRO performance.

A promising strategy for improving the OSRO performance of PA membranes is to reduce their free volume by implementing a post-treatment heating process. Liu *et al*. [54] implemented a two-step heat post-treatment process on the PK-PA membrane The findings revealed that the two-step heat treatment triggered the rearrangement of PA segments, consequently decreasing their free volume diameter from 0.546 nm to 0.528 nm. This effectively improved the OSRO performance of the PA membranes. In a recent study, Chiao *et al*. developed a simple thermal annealing and tannic acid/PEI surface coating method to modify commercial seawater desalination membranes, achieving high ethanol dehydration performance through the osmotically assisted reverse osmosis (OARO) process. The study demonstrates the effectiveness of this method in reducing PA membrane pore size.

OSRO membranes are known to be highly sensitive to surface defects, with even minor defects causing significant performance declines.[108] Lively *et al*. [145] prepared various "defect-engineered" Torlon hollow fiber membranes to investigate the role of skin layer defects in OSRO membranes. Interestingly, repairing surface defects to improve membrane gas separation performance has been extensively studied and applied. For instance, a polydimethylsiloxane (PDMS) coating eliminates the ability of permeating molecules to access Posselier-type defects and is commonly

used in commercial gas separation membranes. However, such defect sealing strategies have not been extensively explored in the OSRO literature. Inspired by the aforementioned work, surface coating to repair PA membrane surface defects is proposed as a promising approach for enhancing OSRO performance.

In this study, the first application of chitosan (CS) coating was introduced to repair surface defects on PA membranes and enhance their OSRO performance. The choice of CS stems from several compelling factors: 1) CS is a natural cationic polysaccharide with excellent biocompatibility and non-toxicity. Its positive charges facilitate electrostatic interactions with the negatively charged PA membrane. 2) Hydroxyl groups within CS molecules can form hydrogen bonds with carboxyl and amide groups on the PA membrane surface, further strengthening the interaction. 3) Amino groups in CS may undergo condensation reactions with carboxyl groups on the PA membrane, leading to the formation of amide covalent bonds. These robust interactions between CS and the PA membrane ensure the stability of the CS coating. CS membranes have been extensively employed in pervaporation (PV) processes for the separation of organic azeotropes, demonstrating their solvent resistance [146]. To further enhance the solvent resistance of the CS coating, glutaraldehyde (GA) crosslinking was employed. Experimental results confirm that the simple CS coating effectively repairs surface defects on the PA membrane, reducing surface pore size and narrowing pore size distribution. The modified PA composite membrane exhibits a remarkable 2.4-fold enhancement in the separation factor for methanol/toluene (mass ratio 9:1), reaching a value of 86.3, which represents the highest reported value to date. This work provides a simple and practical solution for developing high-performance OSRO membranes.

4.2 Experimental

4.2.1 Materials

Lenzing P84 type Polyimide polymer particles (Granlat/SG, ~100,000 g/mol) were procured from Ensinger Sintimid GmbH (Linz, Austria). 1,6-hexanediamine

(HDA, purity 99%) was obtained from Tokyo Chemical Industry (Tokyo, Japan). The m-phenylenediamine (MPD, purity 99.0%) and 1,3,5-benzenetricarbonyl trichloride (TMC, purity 98.0%) were purchased from Sigma-Aldrich (St. Louis, MO, USA). CS with 3 different molecular weights, low molecular weight (50,000-190,000Da), medium molecular weight (190,000-310,000 Da), high molecular weight (310,000 - 375,000 Da), were obtained from Sigma-Aldrich (St. Louis, MO, USA). Glutaraldehyde aqueous solution (GA, 50%) was supplied by Tokyo Chemical Industry (Tokyo, Japan). Other organic solvents ((e.g., methanol, ethanol, propanol, butanol, pentanol, methyl tert-butyl ether (MTBE), isopropyl alcohol, toluene, hexane) used in this study were purchased from FUJIFILM Wako Pure Chemical (Osaka, Japan). Deionized (DI) water was produced using a Milli-Q ultrapure water system (Merck Millipore, Billerica, MA, USA).

4.2.2 Preparation of the control and CS/GA-coated TFC membranes

The cross-linked P84 polyimide (XP84) ultrafiltration (UF) support membranes were fabricated by the nonsolvent-induced phase separation (NIPS) method and subsequent cross-linking procedures according to previous report [68, 70, 72, 120]. In this work, it was aimed to enhance the pressure resistance of the XP84 support membrane by simply increasing the concentration of the P84 casting solution from the previously reported 22% to 28%.

The control TFC membranes, named TFC-PA membranes, were prepared by conventional IP using MPD and TMC on the XP84 UF membranes (**Fig. 4.1a**). Briefly, the surface of the XP84 membranes was prewetted by 3.4 wt% MPD aqueous solution and kept for 2 min, followed by draining the excess aqueous phase solution immediately, and then use a rubber roller to remove the remaining aqueous solution on the membrane surface. Air drying was performed for 1 min, and then a 0.15 wt% TMC/*n*-hexane solution was rapidly poured onto the MPD-impregnated side for 1 min. After removing the excess TMC solution, the nascent membrane was further post-treated in a ventilated oven at a temperature of 60 °C for 10 min. Finally, the resultant

membranes were washed with deionized (DI) water for further modification, testing, and characterization.

The CS/GA-coated TFC membranes, named TFC-PA-CS membranes, were prepared by sequentially immersing the TFC-PA membranes in CS aqueous solution containing 1 wt% acetic acid for 20 min (**Fig. 4.1b**). Specifically, the TFC-PA membranes were washed with DI water, then immersed in a 0.3 wt% GA aqueous solution for 5 min. Finally, the modified membranes were rinsed with DI water several times. The detailed nomenclature of the membranes and the corresponding concentrations of CS and GA during post-coating treatment are presented in **Table 4.1**.

Table 4.1. The nomenclature of the membranes and the corresponding concentrations of CS and GA during post-coating treatment.

Membrane	CS concentration (wt%)	GA concentration (wt%)
TFC-PA	0	0
TFC-PA-CS-0.05	0.05	0.3
TFC-PA-CS-0.1	0.1	0.3
TFC-PA-CS-0.2	0.2	0.3
TFC-PA-CS-0.4	0.4	0.3

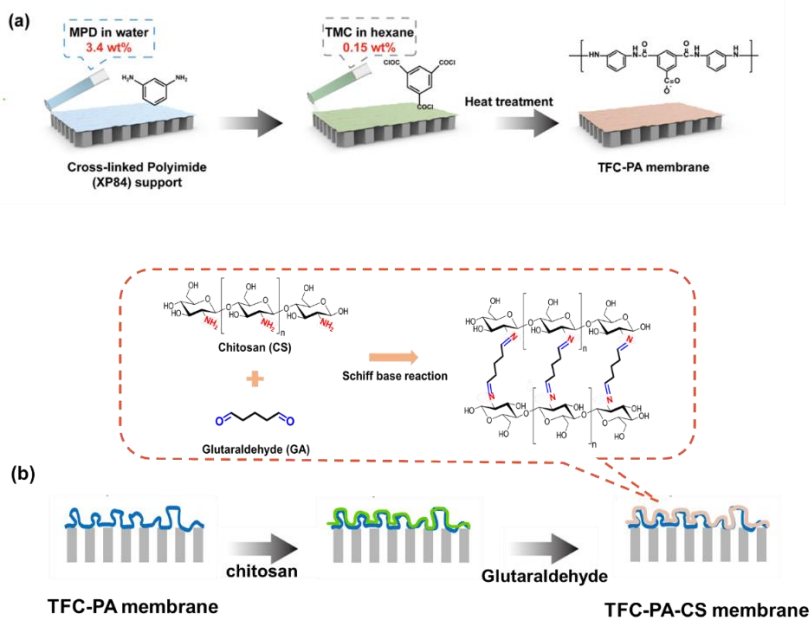

Fig.4.1. Schematic illustration for the fabrication of (a) the TFC-PA membrane and (b) the TFC-PA-CS membrane via interfacial polymerization and surface physical coating method.

4.2.3 Characterizations

The surface chemical structures and element composition of the membranes were analyzed using an attenuated total reflection fourier transform infrared spectrometer (ATR-FTIR; Alpha, Bruker, USA) and an X-ray photoelectron spectroscopy with monochromatic Al Kα excitation (XPS, JPS-9010MC, JEOL, Japan). The surface and cross-sectional morphologies of the membranes was observed by field-emission scanning electron microscopy (FE-SEM, JSM7500F, JEOL Co. Ltd., Tokyo, Japan). The surface roughness of the membranes was characterized by Atomic Force Microscopy (AFM, SPA-400, Hitachi, Japan) in the dynamic force microscopy (tapping) mode. The membrane surface hydrophilicity and polarity were measured using a contact angle analyzer (WCA, DM-300, Kyowa, Japan) with a droplet volume of 2 μL. All samples were fully dried in an oven at 45℃ overnight before characterizations and all tests were performed at room temperature.

4.2.4 Molecular weight cut-off (MWCO) and pore size distribution of PA composite membrane

According to the reported method [54, 147], the molecular weight cut-off

(MWCO) and pore size distribution of TFC-PA and TFC-PA-CS membranes were determined using the rejection rates of small alcohol molecules with different molecular weights, such as ethanol (46 Da), propanol (60 Da), butanol (74 Da), and pentanol (88 Da). The feed solution was MeOH solution with 1 wt% small alcohol. Rejection rate tests were conducted using a laboratory cross-flow system, and solute concentrations in the feed and permeate were measured by gas chromatography (GC, GC-2014, Shimadzu, Japan). The mean effective pore size (μ_p) of the membrane is defined as the solute Stokes diameter (ds) at a solute rejection rate (R) of 50%. The MWCO of the membrane corresponds to the molecular weight at a solute rejection rate (R) of 90%. The Stokes radius (r_p) of the solute can be calculated using Equation (1):

$$\log(r_p) = -1.4962 + 0.4654 \log(\mathrm{Mw}) \tag{4.1}$$

Where Mw is the molecular weight of the model solutes.

To obtain the pore size distribution of the tested membranes, a log-normal model relating solute rejection and solute Stokes radius is applied [148-150], as represented by Equation (2):

$$\frac{dR(d_p)}{dd_p} = \frac{1}{d_p ln\sigma_{p\sqrt{2\pi}}} exp\left[-\frac{(lnd_p - ln\mu_p)^2}{2(ln\sigma_p)^2}\right] \tag{4.2}$$

where μ_p is the mean effective pore size which is determined at solute rejection R = 50%, and σ_p is the geometric standard deviation, which is defined as the ratio of d_p at R = 84.13% over that at R = 50%.

4.2.5 OSRO performance measurement

The OSRO performance, including the selective separation of organic solvent mixtures, long-term organic solvent mixtures separation stability, etc., was evaluated in a cross-flow filtration system [55, 83, 91, 114, 119]. The membrane was placed in a stainless-steel cell (effective permeation area: 7.07 cm^2) before performance evaluation. The stirring speed of the stainless-steel cell was fixed to 900 rpm to minimize the possible change in osmotic pressure caused by concentration

polarization when testing the selective separation of organic mixtures. The applied pressure was slowly increased in a range of 0–14 MPa *via* a back-pressure valve (Swagelok, KPB). The feed solution was circulated back to the feed container using a plunger pump (NP-FX100 series; FLOM Co., Japan) at the flow rate of 20 mL min^{-1}. The OSRO performance tests were performed by pre-compacting the membrane in pure methanol under 7 MPa at least 12 hours to obtain a stable membrane performance. The selective separation performance of three kinds of organic mixtures, including methanol/hexane (M/Hex), methanol/toluene (M/T), and methanol/MTBE (M/MTBE), were evaluated within the methanol concentration range (70 wt%-100 wt%) and pressure range (3-7MPa). Based on its composition, the mixture is denoted AxBy. For example, a solution containing 90 wt% MeOH and 10 wt% toluene is denoted M90T10. The composition of permeate and feed solution were detected using gas chromatography (GC, GC-2014, Shimadzu, Japan). After the measurement of each mixture, the feed solution was displaced with pure methanol, and pure methanol flux was measured again in order to evaluate membrane stability. The solvent flux (J_v, kg m^{-2} h^{-1}) and the separation factor (α) of azeotropic mixture were calculated using equations (3) and (4):

$$J_v = \frac{m}{A * T} \tag{4.3}$$

where *m*, *A*, and *T* are the respective permeate weight (kg), effective membrane area (m^2), and operation time (h).

$$\alpha_{A/B} = \frac{\chi_{Ap}/\chi_{Bp}}{\chi_{Af}/\chi_{Bf}} \tag{4.4}$$

where χ_{Ap}, χ_{Bp}, and χ_{Af}, χ_{Bf} are molar fractions of component A and component B in the permeate and feed, respectively. The composition of the permeate and feed samples was analyzed using a GC-2014 gas chromatograph using methods reported in the literature [83].

4.3 Results and discussion

4.3.1 Synthesis and intercalation of mediated nanoparticles

The top surface SEM images (**Fig. 4.2a-e**) indicate that with the increase in CS concentration, the protruding structures on the surface of the TFC-PA membrane are gradually covered by the CS/GA layer, eventually achieving complete coverage. It is noteworthy that the surface of the TFC-PA membrane does not exhibit the typical peak-valley structure but rather shows small protrusions resembling those of nanofiltration membranes. This phenomenon may be attributed to the use of different support membranes, which could influence the interfacial polymerization process. Compared to the large-scale peak-valley structure on the PA membrane [130, 131], these small protrusions may be more conducive to the deposition of the CS/GA layer on the surface of the PA membrane. Roughly estimate the thickness of selective layers by measuring SEM cross-sectional images of each membrane. The results (**Fig. 4.2f-j**) shows that as the CS concentration increases, the thickness of the selective layer gradually increases from approximately 29 nm initially to 100 nm. AFM results (**Fig. 4.2k-o**) show that the average roughness (Ra) of the PA composite membrane surface is slightly reduced after coating CS/GA layer.

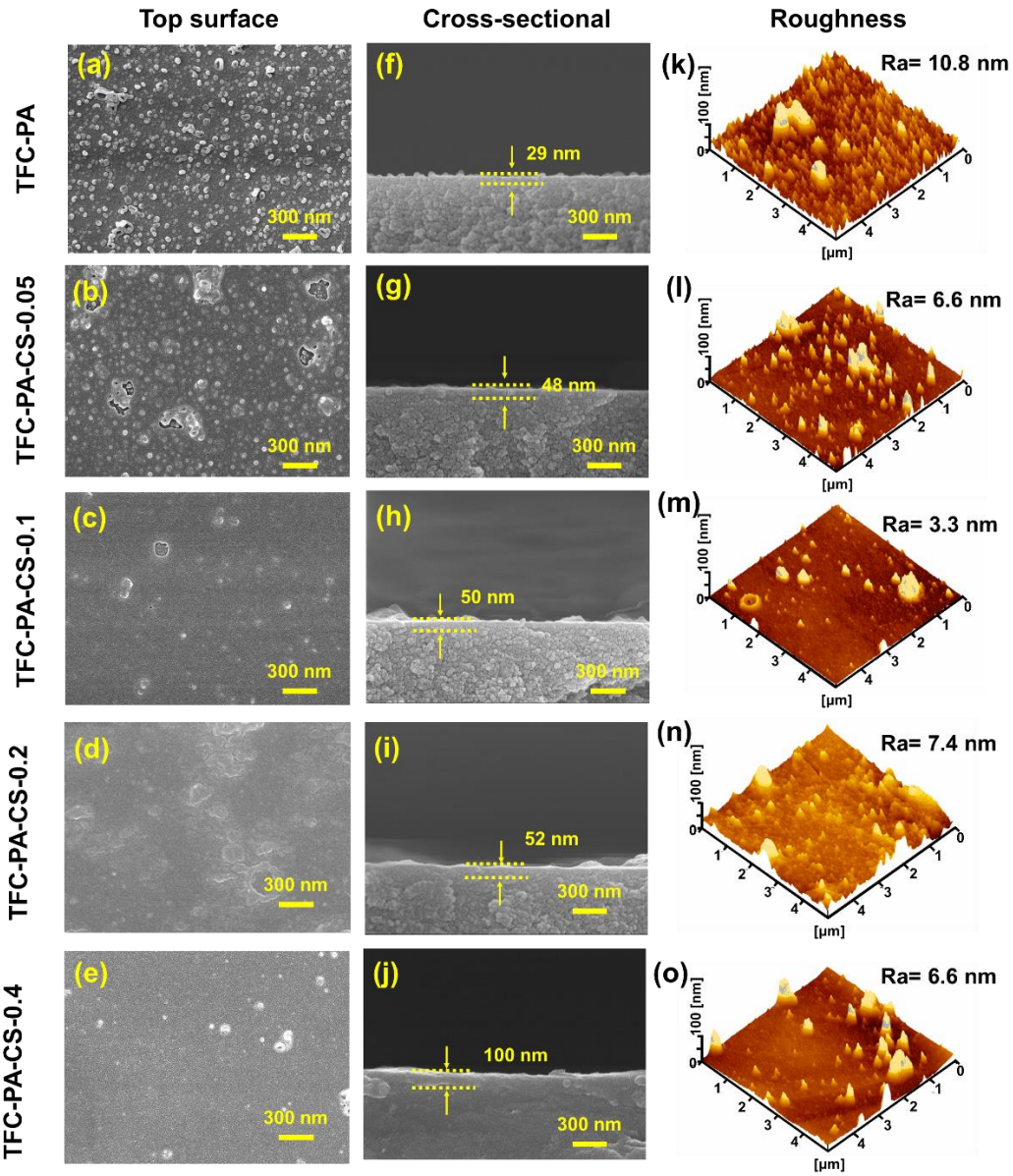

Fig. 4.2. SEM surface morphologies, SEM cross-sectional morphologies, and the AFM 3D profile of the (a, f, k) TFC-PA membrane, (b, g ,l) TFC-PA-CS-0.05 membrane, (c, h, m) TFC-PA-CS-0.1 membrane, (d, i, n) TFC-PA-CS-0.2 membrane, (e, j, o) TFC-PA-CS-0.4 membrane.

ATR-FTIR technology was implemented to characterize the chemical structure changes on the PA membrane surface before and after coating the CS/GA layer. The results (**Fig. 4.3a**) show that both the TFC-PA membrane and the TFC-PA-CS membranes exhibit nearly identical infrared characteristic absorption peaks. Although the Schiff base reaction between CS and GA forms imine bonds distinguishable from those of the PA membrane, the imine bonds of the XP84 support membrane may

introduce interference, considering the depth of the infrared detection. The partial enlargement of the FTIR spectrum (**Fig. 4.3b**) shows that the intensity of the broad peak at 3250-3550 cm^{-1} wavenumbers attributed to the -NH_2 and -OH functional groups in PA or CS/GA layer gradually increases with the CS concentration. This implies that the loading amount of CS/GA on the PA membrane surface gradually increases, which is consistent with the SEM results.

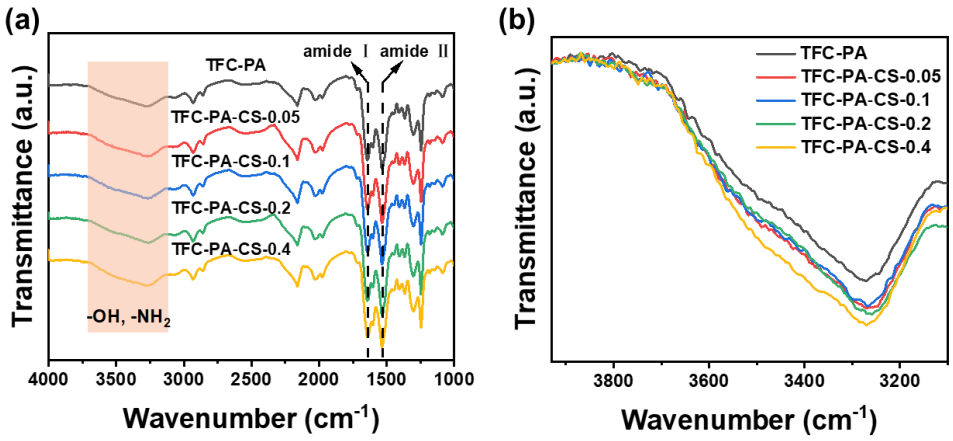

Fig. 4.3 The FTIR spectrum of (a) the TFC-PA and the TFC-PA-CS membranes. (b) The partial enlargement of the FTIR spectrum in a wavenumber range of 3100-3920 cm^{-1}.

XPS characterization was used to study the changes in the elemental composition of the PA membrane surface before and after coating with CS/GA layer. **Fig. 4.4** presents the high-resolution XPS spectra in the N 1s region of the TFC-PA and TFC-PA-CS membrane. Two resolved peaks at 399.8 eV and 400.7 eV of TFC-PA membrane were observed (**Fig. 4.4a**), which was corresponded to the -CONH and -NH_3^+ formed after protonation of unreacted amino groups. As shown in **Fig. 4.4b-e,** the new components at 402.1 eV of TFC-PA-CS membrane were observed, which was corresponded to the -N=C (imine bonds) attributed to the Schiff base reaction between CS and GA. [146] The results indicate the successful coating of the CS/GA layer on the PA membrane surface. It has been observed that with the increase in CS concentration, the content of imine bonds initially increases and then decreases (**Fig.**

4.4f). This trend may be attributed to the fact that at higher CS concentrations, the denser entanglement of CS chains constrains the cross-linking efficiency of GA. [151]

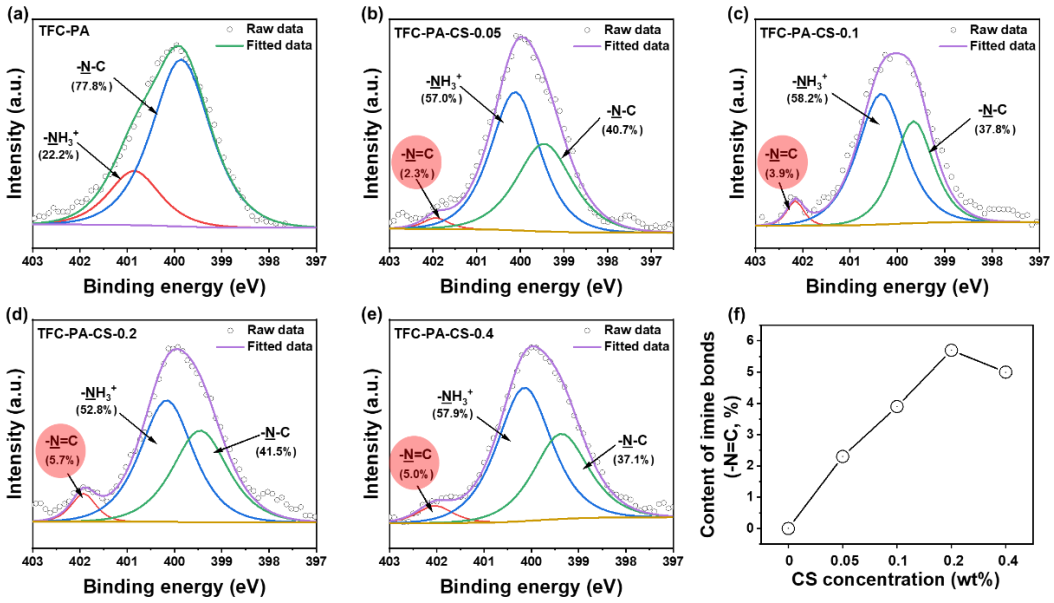

Fig. 4.4. High-resolution XPS spectra in the N 1s region of the (a) TFC-PA membrane, and (b-e) TFC-PA-CS membranes with different CS concentration. (f) Changes in imine bond content on the TFC-PA-CS membranes surface with CS concentration.

4.3.2 The effect of coating CS/GA layer on surface pore size and distribution of the PA membrane

The hypothesis of this study is that the surface pore size and its distribution of the PA composite membrane will become smaller and narrower after coating with CS/GA layer. However, directly measuring the pore size and distribution on the membrane surface often presents technical challenges, thus making indirect characterization of pore size changes a common approach. By determining the MWCO of the membrane, one can assess the membrane's density and infer trends in pore size changes. Furthermore, using a log-normal distribution model based on solute rejection and solute Stokes radius, the pore size distribution of the membrane can be quantitatively analyzed. [148-150] As illustrated in the **Fig. 4.5a**, the TFC-PA membrane exhibits the highest MWCO value of approximately 74 Da, while the TFC-PA-CS membrane displays a significantly lower MWCO value. This observation

indicates that the PA composite membrane became denser after the application of the CS/GA layer. Notably, the TFC-PACS-0.2 membrane exhibits the lowest MWCO value of around 66 Da. Furthermore, the trend of MWCO value changes for the TFC-PA-CS membrane aligns with the trend of imine bond content variations observed in XPS analysis. This finding suggests that the crosslinking degree of CS/GA influences the ultimate compactness of the PA composite membrane. Delving further, the pore size distribution curve of the membrane was obtained based on the log-normal distribution model between solute rejection rate and Stokes radius. The results (**Fig. 4.5b**) demonstrate that the TFC-PA membrane exhibits a relatively broad pore size distribution with a mean effective pore size of approximately 0.64 nm. In contrast, the TFC-PA-CS membrane displays a significantly narrower pore size distribution with a mean effective pore size ranging from 0.38 to 0.4 nm. This compelling evidence strongly suggests that the deposition of a CS/GA layer effectively reduces the pore size on the surface of the PA membrane and leads to a more uniform pore size distribution.

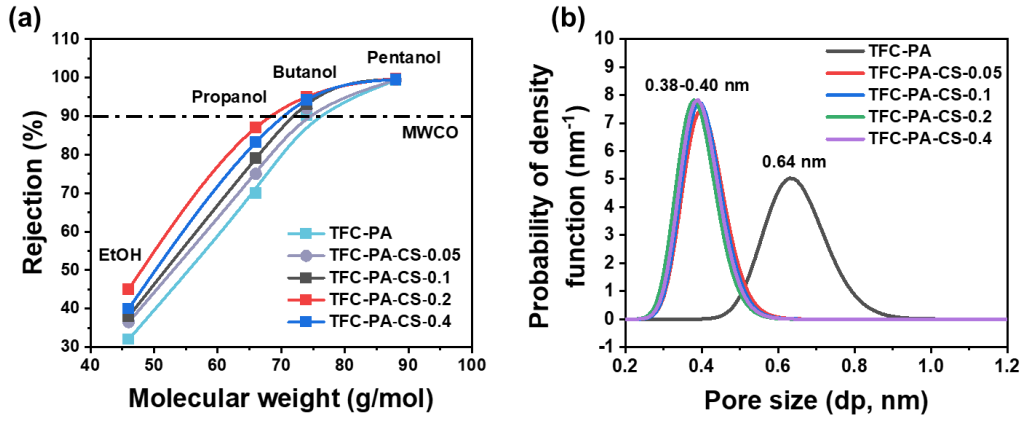

Fig. 4.5. (a) The rejection of small molecular alcohols with different molecular weights. Feed solution is MeOH with 1 wt% solute (EtOH, propanol, butanol, pentanol). The molecular weight corresponding to a rejection of 90% is the molecular weight cut-off (MWCO) of the membrane. (b) The pore size distribution of the TFC-PA and TFC-PA-CS membranes.

4.3.3 OSRO performances

Polar/non-polar organic liquid mixtures have extensive applications in various industrial sectors, with MeOH/toluene mixtures being particularly prevalent in the pharmaceutical and fine chemical industries [54, 110, 114, 138, 139]. The separation of MeOH and toluene waste streams generated during production is crucial for achieving sustainable manufacturing practices. Leveraging the inherent polarity of PA membranes, these membranes hold immense potential for the separation of MeOH/toluene mixtures. Accordingly, this study delves into a comprehensive evaluation of the OSRO performance of PA composite membranes by investigating the transmembrane flux and separation factor of MeOH/toluene organic liquid mixtures. The impact of CS concentration on the separation performance of the membrane towards the M90T10 mixture was initially investigated. As illustrated in the **Fig. 4.6a**, with the gradual increase of CS concentration from 0 to 0.2 wt%, the total flux of M90T10 for the PA composite membrane exhibited a decreasing trend, while the M90T10 separation factor showed a significant enhancement. This improvement in separation factor and decrease in flux can be attributed to the smaller pore size and narrower pore size distribution of the TFC-PA-CS membrane. Further increasing the CS concentration to 0.4 wt% led to a rebound in flux and a decline in separation factor. Excessively high CS concentration, on the one hand, restricted its crosslinking efficiency with GA, diminishing the repair effect of the CS/GA layer on the PA membrane surface. On the other hand, it could potentially result in excessive deposition of CS/GA on the PA membrane surface, leading to defect formation. Notably, the PA composite membrane exhibited optimal performance when the CS concentration was 0.2 wt%, with its separation factor improving from the initial 35.4 to 86.3, while the total flux decreased from 10.43 kg m^{-2} h^{-1} to 5.04 kg m^{-2} h^{-1}. **Fig. 4.6b** shows the effect of using CS with different molecular weights on the M90T10 separation performance of the PA composite membrane. The results show that low molecular weight CS has the best modification effect, and the prepared membrane has the highest M90T10 flux and separation factor.

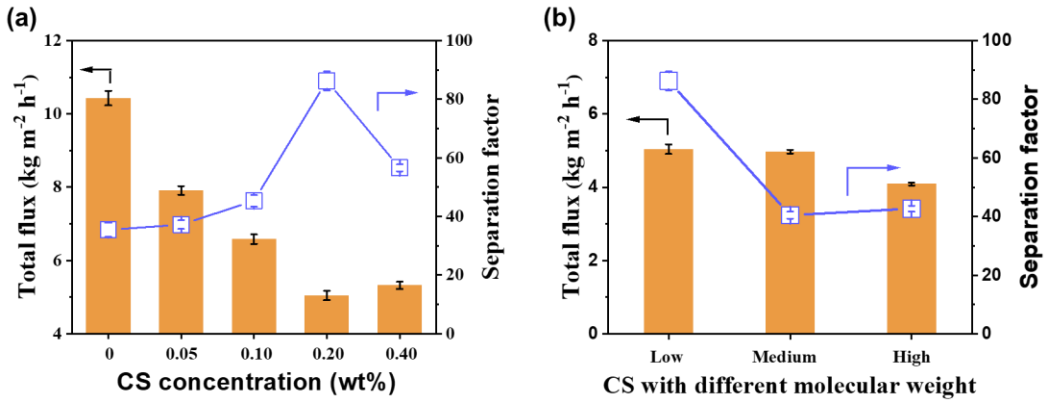

Fig. 4.6. Total flux and separation factor of PA composite membrane modified (a) with different CS concentration and (b) with CS of different molecular weights. The feed solution is M90T10, and the operating pressure is 7 MPa.

The crucial importance of operating conditions on separation performance is undeniable, and this is particularly evident in the OSRO process. As is well-known, organic solvent mixtures generate relatively high osmotic pressure, necessitating the operation of the OSRO process under high pressure. [83, 110, 114] Due to the varying sensitivities of the individual components of organic mixtures to the applied pressure, their separation performance often exhibits differences. [152] Furthermore, the osmotic pressure of organic mixtures is closely related to their concentration. [110, 141, 142, 152] In practical applications, organic liquid mixtures with different solute concentrations have different application scenarios. To ensure consistent separation performance, different concentrations of organic mixtures require matching operation pressures. Therefore, in-depth investigation of the impact of operating pressure and feed organic mixture concentration on the entire OSRO separation process holds significant theoretical and practical value.

Fig. 4.7a shows the effect of operating pressure on the M90T10 flux and separation factor of TFC-PA and optimal TFC-PA-CS-0.2 membranes. The results demonstrate that both the M90T10 flux and separation factor exhibit an upward trend with increasing pressure, which is consistent with the findings reported in the literature. [110, 141, 142, 152] According to the solution-diffusion theory, the membrane flux is directly proportional to the pressure difference.[54] [153] The

enhancement of the separation factor with increasing pressure is primarily attributed to the higher pressure-sensitivity of MeOH transport across the membrane compared to that of toluene. Toluene molecules cannot permeate the PA membrane independently and can only cross the membrane in the form of MeOH-toluene clusters.[152] However, the permeability of these clusters is significantly lower than that of MeOH molecules. Therefore, higher applied pressure provides M90T10 with a higher flux and separation factor.

As depicted in **Fig. 4.7b**, the separation performance of the membranes exhibits a clear trend with variations in toluene concentration in the M90T10 feed solution: both membrane flux and separation factor decrease as toluene concentration increases. This observation aligns with the findings reported in the literature. [54, 152] The underlying mechanism for this trend lies in the continuously expanding osmotic pressure difference across the membrane with increasing toluene concentration, leading to a decreased effective driving force and a consequent decline in the membrane's M90T10 flux. Notably, MeOH exhibits a higher sensitivity to concentration changes compared to toluene, mirroring the difference in pressure sensitivity between the components of the M90T10 mixture. Specifically, on the one hand, as toluene concentration increases, the decreased effective driving force leads to a decrease in the flux of both MeOH and toluene in the mixed solvent. On the other hand, as toluene concentration increases, the increasing abundance of MeOH-toluene clusters and the decreasing number of MeOH molecules result in a relative increase in toluene flux and a relative decrease in MeOH flux. In summary, a higher toluene concentration in the M90T10 feed solution leads to a dual decline in both membrane flux and separation factor. In general, the similar responses of the two membranes to operating pressure and feed solution concentration indicate that the coating of the CS/GA layer did not alter the fundamental separation characteristics of the PA membrane. However, due to its smaller pore size and narrower pore size distribution, the TFC-PA-CS-0.2 membrane exhibits lower flux and higher separation factor compared to the TFC-PA membrane.

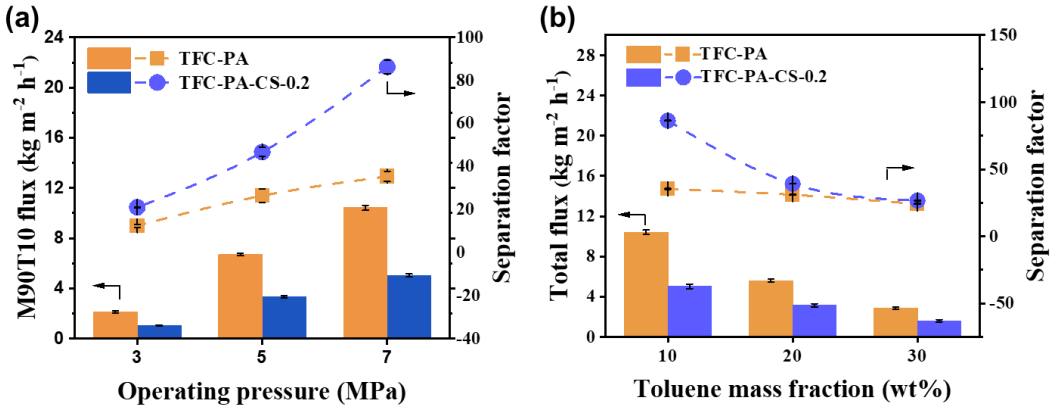

Fig. 4.7. (a) M90T10 flux and separation factors of TFC-PA and TFC-PA-CS-0.2 membranes under different operating pressures. (b) Total flux and MeOH/Toluene separation factors of TFC-PA and TFC-PA-CS-0.2 membranes under feed solutions with varying toluene concentrations.

The long-term stability of OSRO membranes is particularly crucial in practical applications involving organic solvents. Herein, we used M90T10 as the feed solution to conduct continuous penetration experiments at an operating pressure of 7 MPa. The results showed (**Fig. 4.8a**) that the TFC-PA-CS-0.2 membrane maintained stable separation performance during continuous testing for up to 7 days, which demonstrated a good long-term stability and excellent swelling resistance of the TFC-PA-CS-0.2 membrane. As shown in **Fig. 4.8b** and **Table 4.2**, compared with OSRO membranes used to separate MeOH/toluene organic liquid mixtures,[54, 55, 83, 110, 114, 152] our membrane exhibits superior MeOH/toluene separation performance, with a separation factor approximately 2-8 times that of most membranes. In summary, our membrane exhibits excellent OSRO performance, and its OSRO performance is further improved through simple surface physical modification.

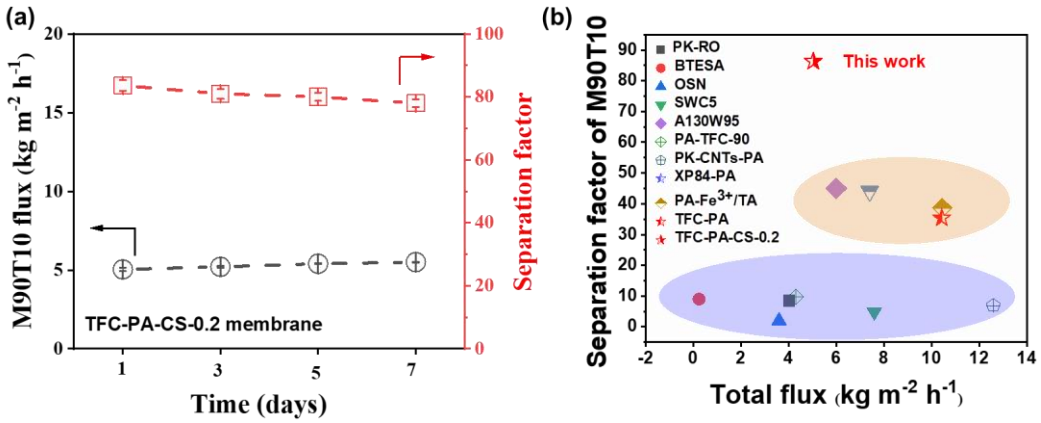

Fig. 4.8. (a) Long-term stability of TFC-PA-CS-0.2 membrane tested under 7 MPa with M90T10 as the feed solution. (b) Performance comparison of our membranes with the state-of-the-art OSRO membranes using M90T10 as the feed solution.

Table 4.2. Comparison of the separation performance between literatures and this work for methanol/toluene.

Membrane	Operating pressure [MPa]	Total flux [kg m^{-2} h^{-1})]	Separation factor [-]
BTESA[110]	18	0.24	9.00
PK-RO[83]	3	4.03	8.40
OSN[83]	3	3.6	2.00
SWC5[83]	3	7.6	4.80
A130W95[54]	3	6.0	45.0
PA-TFC-90[55]	3	4.3	9.76
PK-CNTs-PA[114]	3	12.6	6.90
XP84-PA[152]	7	7.41	44.1
PA-Fe^{3+}/TA[152]	7	10.45	38.7
TFC-PA (This work)	7	10.43	35.4
TFC-PA-CS-0.2 (This work)	7	5.04	86.3

4.4 Conclusions

In summary, a high-performance OSRO membrane with smaller pore size and narrower pore size distribution was developed by coating a layer of CS/GA on the surface of the PA membrane. The experimental results emphasized that coating the CS/GA layer effectively repaired the defects on the PA membrane surface. The similar responses of the TFC-PA-CS-0.2 membrane and the TFC-PA membrane to pressure and feed concentration prove that the separation characteristics of the PA composite membrane are not changed after coating the CS/GA layer. Importantly, the CS/GA layer reduces the pore size of the TFC membrane, achieving smaller pore size and narrower pore size distribution. Compared with TFC-PA membrane, the optimal TFC-PA-CS-0.2 membrane exhibits 2.4 times higher separation factor of M90T10. Overall, this study provides a simple and practical method for developing high-performance OSRO membranes.

References

[1] R.P. Lively, D.S. Sholl, From water to organics in membrane separations, Nat Mater, 16 (2017) 276-279.
[2] P. Marchetti, M.F. Jimenez Solomon, G. Szekely, A.G. Livingston, Molecular separation with organic solvent nanofiltration: a critical review, Chem. Rev., 114 (2014) 10735-10806.
[3] C. Capello, U. Fischer, K. Hungerbühler, What is a green solvent? A comprehensive framework for the environmental assessment of solvents, Green Chemistry, 9 (2007) 927-934.
[4] D.S. Sholl, R.P. Lively, Seven chemical separations to change the world, Nature, 532 (2016) 435-437.
[5] D. De Meis, Overview on porous inorganic membranes for gas separation, 2017.
[6] A. Gul, J. Hruza, F. Yalcinkaya, Fouling and Chemical Cleaning of Microfiltration Membranes: A Mini-Review, Polymers (Basel), 13 (2021).
[7] N. Hampu, J.R. Werber, W.Y. Chan, E.C. Feinberg, M.A. Hillmyer, Next-Generation Ultrafiltration Membranes Enabled by Block Polymers, ACS Nano, 14 (2020) 16446-16471.
[8] S. Shao, F. Zeng, L. Long, X. Zhu, L.E. Peng, F. Wang, Z. Yang, C.Y. Tang, Nanofiltration Membranes with Crumpled Polyamide Films: A Critical Review on Mechanisms, Performances, and Environmental Applications, Environ. Sci. Technol., 56 (2022) 12811-12827.
[9] R.H. Hailemariam, Y.C. Woo, M.M. Damtie, B.C. Kim, K.D. Park, J.S. Choi, Reverse osmosis membrane fabrication and modification technologies and future trends: A review, Adv. Colloid Interface Sci., 276 (2020) 102100.
[10] C. Liu, G. Dong, T. Tsuru, H. Matsuyama, Organic solvent reverse osmosis membranes for organic liquid mixture separation: A review, J. Membr. Sci., 620 (2021) 118882.
[11] A.A. Bhat, V.G. Pangarkar, Methanol-selective membranes for the pervaporative separation of methanol–toluene mixtures, J. Membr. Sci., 167 (2000) 187-201.
[12] D. Ren, S. Ren, Y. Lin, J. Xu, X. Wang, Recent developments of organic solvent resistant materials for membrane separations, Chemosphere, 271 (2021) 129425.
[13] P. Vandezande, L.E. Gevers, I.F. Vankelecom, Solvent resistant nanofiltration: separating on a molecular level, Chem. Soc. Rev., 37 (2008) 365-405.
[14] S. Hermans, H. Mariën, C. Van Goethem, I.F.J. Vankelecom, Recent developments in thin film (nano)composite membranes for solvent resistant nanofiltration, Current Opinion in Chemical Engineering, 8 (2015) 45-54.
[15] Y. Li, Z. Guo, S. Li, B. Van der Bruggen, Interfacially Polymerized Thin-Film Composite Membranes for Organic Solvent Nanofiltration, Advanced Materials Interfaces, 8 (2020) 2001671.
[16] S. Sourirajan, Separation of Hydrocarbon Liquids by Flow Under Pressure Through Porous Membranes, Nature, 203 (1964) 1348-1349.
[17] S. Manjikian, S. Loeb, J. McCutchan, Improvement in fabrication techniques for

reverse osmosis desalination membranes, Proc. 1st Int. Syrup. Water Desalination, (1965) 159-173.
[18] G. Szekely, M.F. Jimenez-Solomon, P. Marchetti, J.F. Kim, A.G. Livingston, Sustainability assessment of organic solvent nanofiltration: from fabrication to application, Green Chem., 16 (2014) 4440-4473.
[19] M. Qasim, M. Badrelzaman, N.N. Darwish, N.A. Darwish, N. Hilal, Reverse osmosis desalination: A state-of-the-art review, Desalination, 459 (2019) 59-104.
[20] J.M. Gohil, P. Ray, A review on semi-aromatic polyamide TFC membranes prepared by interfacial polymerization: Potential for water treatment and desalination, Separation and Purification Technology, 181 (2017) 159-182.
[21] S. Manjikian, S. Loeb, J. McCutchan, Improvement in fabrication techniques for reverse osmosis desalination membranes, in: Proceedings of the First International Symposium on Water Desalination, 1967, pp. 159-173.
[22] J.C. Jansen, S. Darvishmanesh, F. Tasselli, F. Bazzarelli, P. Bernardo, E. Tocci, K. Friess, A. Randova, E. Drioli, B. Van der Bruggen, Influence of the blend composition on the properties and separation performance of novel solvent resistant polyphenylsulfone/polyimide nanofiltration membranes, J. Membr. Sci., 447 (2013) 107-118.
[23] C. Guizard, A. Ayral, A. Julbe, Potentiality of organic solvents filtration with ceramic membranes. A comparison with polymer membranes, Desalination, 147 (2002) 275-280.
[24] W. Li, Z. Yang, Q. Meng, C. Shen, G. Zhang, Thermally stable and solvent resistant self-crosslinked TiO2/PAN hybrid hollow fiber membrane fabricated by mutual supporting method, J. Membr. Sci., 467 (2014) 253-261.
[25] T. Tsuru, M. Miyawaki, H. Kondo, T. Yoshioka, M. Asaeda, Inorganic porous membranes for nanofiltration of nonaqueous solutions, Separation and purification technology, 32 (2003) 105-109.
[26] W.J. Koros, R. Mahajan, Pushing the limits on possibilities for large scale gas separation: which strategies?, J. Membr. Sci., 175 (2000) 181-196.
[27] S. Morooka, S. Yan, K. Kusakabe, Y. Akiyama, Formation of hydrogen-permselective SiO2 membrane in macropores of α-alumina support tube by thermal decomposition of TEOS, J. Membr. Sci., 101 (1995) 89-98.
[28] M. Lee, B. Wang, K. Li, New designs of ceramic hollow fibres toward broadened applications, J. Membr. Sci., 503 (2016) 48-58.
[29] F.E. Bortot Coelho, G. Magnacca, V. Boffa, V.M. Candelario, M. Luiten-Olieman, W. Zhang, From ultra to nanofiltration: A review on the fabrication of ZrO2 membranes, Ceram. Int., 49 (2023) 8683-8708.
[30] S. Karan, Z. Jiang, A.G. Livingston, MEMBRANE FILTRATION. Sub-10 nm polyamide nanofilms with ultrafast solvent transport for molecular separation, Science, 348 (2015) 1347-1351.
[31] J. Liu, J. Jiang, Microporous benzimidazole-linked polymer and its derivatives for organic solvent nanofiltration, Polymer, 185 (2019) 121932.
[32] K.S. Goh, J.Y. Chong, Y. Chen, W. Fang, T.-H. Bae, R. Wang, Thin-film composite hollow fibre membrane for low pressure organic solvent nanofiltration, J.

Membr. Sci., 597 (2020) 117760.
[33] H. Siddique, Y. Bhole, L.G. Peeva, A.G. Livingston, Pore preserving crosslinkers for polyimide OSN membranes, J. Membr. Sci., 465 (2014) 138-150.
[34] H.M. Tham, S. Japip, T.-S. Chung, WS2 deposition on cross-linked polyacrylonitrile with synergistic transformation to yield organic solvent nanofiltration membranes, J. Membr. Sci., 588 (2019) 117219.
[35] T. Huang, J. Song, S. He, T. Li, X.-M. Li, T. He, Enabling sustainable green close-loop membrane lithium extraction by acid and solvent resistant poly (ether ether ketone) membrane, J. Membr. Sci., 589 (2019) 117273.
[36] E.J. Kappert, M.J.T. Raaijmakers, K. Tempelman, F.P. Cuperus, W. Ogieglo, N.E. Benes, Swelling of 9 polymers commonly employed for solvent-resistant nanofiltration membranes: A comprehensive dataset, J. Membr. Sci., 569 (2019) 177-199.
[37] K.P. Lee, T.C. Arnot, D. Mattia, A review of reverse osmosis membrane materials for desalination—Development to date and future potential, Journal of Membrane Science, 370 (2011) 1-22.
[38] B. Khorshidi, T. Thundat, B.A. Fleck, M. Sadrzadeh, A Novel Approach Toward Fabrication of High Performance Thin Film Composite Polyamide Membranes, Sci. Rep., 6 (2016) 22069.
[39] E.L. WITTBECKER, P.W. MORGAN, Interfacial Polycondensation, Journal of Polymer Science, 40 (1959) 289-297.
[40] P.W. Morgan, S.L. Kwolek, Interfacial polycondensation. II. Fundamentals of polymer formation at liquid interfaces, J. Polym. Sci., 40 (2003) 299-327.
[41] J. Cadotte, R. Petersen, R. Larson, E. Erickson, A new thin-film composite seawater reverse osmosis membrane, Desalination, 32 (1980) 25-31.
[42] K.A. Thompson, R. Mathias, D. Kim, J. Kim, N. Rangnekar, J. Johnson, S.J. Hoy, I. Bechis, A. Tarzia, K.E. Jelfs, N-Aryl–linked spirocyclic polymers for membrane separations of complex hydrocarbon mixtures, Science, 369 (2020) 310-315.
[43] V. Freger, G.Z. Ramon, Polyamide desalination membranes: Formation, structure, and properties, Prog. Polym. Sci., 122 (2021) 101451.
[44] N.Y. Yip, A. Tiraferri, W.A. Phillip, J.D. Schiffman, M. Elimelech, High Performance Thin-Film Composite Forward Osmosis Membrane, Environmental science & technology, 44 (2010) 3812-3818.
[45] J.E. Cadotte, R.J. Petersen, R.E. Larson, E.E. Erickson, A new thin-film composite seawater reverse osmosis membrane, Desalination, 32 (1980) 25-31.
[46] W.-S. Hung, T.-J. Lin, Y.-H. Chiao, A. Sengupta, Y.-C. Hsiao, S.R. Wickramasinghe, C.-C. Hu, K.-R. Lee, J.-Y. Lai, Graphene-induced tuning of the d-spacing of graphene oxide composite nanofiltration membranes for frictionless capillary action-induced enhancement of water permeability, J. Mater. Chem. A, 6 (2018) 19445-19454.
[47] S. Wang, D. Mahalingam, B. Sutisna, S.P. Nunes, 2D-dual-spacing channel membranes for high performance organic solvent nanofiltration, J. Mater. Chem. A, 7 (2019) 11673-11682.
[48] R. Ding, H. Zhang, Y. Li, J. Wang, B. Shi, H. Mao, J. Dang, J. Liu, Graphene

oxide-embedded nanocomposite membrane for solvent resistant nanofiltration with enhanced rejection ability, Chemical Engineering Science, 138 (2015) 227-238.
[49] S. Li, C. Li, X. Song, B. Su, B. Mandal, B. Prasad, X. Gao, C. Gao, Graphene Quantum Dots-Doped Thin Film Nanocomposite Polyimide Membranes with Enhanced Solvent Resistance for Solvent-Resistant Nanofiltration, ACS Appl Mater Interfaces, 11 (2019) 6527-6540.
[50] S. Roy, S.A. Ntim, S. Mitra, K.K. Sirkar, Facile fabrication of superior nanofiltration membranes from interfacially polymerized CNT-polymer composites, J. Membr. Sci., 375 (2011) 81-87.
[51] Q. Liu, P. Zhang, B. Na, R. Lv, R. Tian, Silica Nanoparticle-Mediated Solution-Phase Separation to Highly Porous Polylactide Membranes, J. Phys. Chem. C, 118 (2014) 25620-25625.
[52] J. Campbell, R. Davies, D.C. Braddock, A. Livingston, Improving the permeance of hybrid polymer/metal–organic framework (MOF) membranes for organic solvent nanofiltration (OSN)–development of MOF thin films via interfacial synthesis, J. Mater. Chem. A, 3 (2015) 9668-9674.
[53] C. Li, S. Li, L. Tian, J. Zhang, B. Su, M.Z. Hu, Covalent organic frameworks (COFs)-incorporated thin film nanocomposite (TFN) membranes for high-flux organic solvent nanofiltration (OSN), J. Membr. Sci., 572 (2019) 520-531.
[54] C. Liu, R. Takagi, D. Saeki, L. Cheng, T. Shintani, T. Yasui, H. Matsuyama, Highly improved organic solvent reverse osmosis (OSRO) membrane for organic liquid mixture separation by simple heat treatment, J. Membr. Sci., 618 (2021) 118710.
[55] G. Xu, Y.-H. Chiao, W. Fu, L. Deng, M. Hu, K. Guan, R.R. Gonzales, H. Matsuyama, Temperature-modulated formation of polyamide layer for enhanced organic solvent reverse osmosis (OSRO) performance, J. Membr. Sci., 682 (2023) 121793.
[56] S. Li, R. Dong, V.E. Musteata, J. Kim, N.D. Rangnekar, J.R. Johnson, B.D. Marshall, S. Chisca, J. Xu, S. Hoy, B.A. McCool, S.P. Nunes, Z. Jiang, A.G. Livingston, Hydrophobic polyamide nanofilms provide rapid transport for crude oil separation, Science, 377 (2022) 1555-1561.
[57] D.S. Sholl, R.P. Lively, Seven chemical separations to change the world, Nature, 532 (2016) 435-437.
[58] X. Shan, S.-L. Li, W. Fu, Y. Hu, G. Gong, Y. Hu, Preparation of high performance TFC RO membranes by surface grafting of small-molecule zwitterions, J. Membr. Sci., 608 (2020) 118209.
[59] S.L. Li, X. Shan, Y. Zhao, Y. Hu, Fabrication of a Novel Nanofiltration Membrane with Enhanced Performance via Interfacial Polymerization through the Incorporation of a New Zwitterionic Diamine Monomer, ACS Appl Mater Interfaces, 11 (2019) 42846-42855.
[60] M.F. Jimenez Solomon, Y. Bhole, A.G. Livingston, High flux membranes for organic solvent nanofiltration (OSN)—Interfacial polymerization with solvent activation, J. Membr. Sci., 423-424 (2012) 371-382.
[61] H. Marien, L. Bellings, S. Hermans, I.F. Vankelecom, Sustainable Process for the Preparation of High-Performance Thin-Film Composite Membranes using Ionic

Liquids as the Reaction Medium, ChemSusChem, 9 (2016) 1101-1111.
[62] M.F. Jimenez Solomon, Y. Bhole, A.G. Livingston, High flux hydrophobic membranes for organic solvent nanofiltration (OSN)—Interfacial polymerization, surface modification and solvent activation, J. Membr. Sci., 434 (2013) 193-203.
[63] M.F. Jimenez-Solomon, P. Gorgojo, M. Munoz-Ibanez, A.G. Livingston, Beneath the surface: Influence of supports on thin film composite membranes by interfacial polymerization for organic solvent nanofiltration, J. Membr. Sci., 448 (2013) 102-113.
[64] S. Kandambeth, B.P. Biswal, H.D. Chaudhari, K.C. Rout, H.S. Kunjattu, S. Mitra, S. Karak, A. Das, R. Mukherjee, U.K. Kharul, R. Banerjee, Selective Molecular Sieving in Self-Standing Porous Covalent-Organic-Framework Membranes, Adv. Mater., 29 (2017) 1603945.
[65] J. Liu, D. Hua, Y. Zhang, S. Japip, T.S. Chung, Precise Molecular Sieving Architectures with Janus Pathways for Both Polar and Nonpolar Molecules, Adv. Mater., 30 (2018) 1705933.
[66] L.F. Villalobos, T. Huang, K.V. Peinemann, Cyclodextrin Films with Fast Solvent Transport and Shape-Selective Permeability, Adv. Mater., 29 (2017) 1606641.
[67] T. Huang, T. Puspasari, S.P. Nunes, K.V. Peinemann, Ultrathin 2D-Layered Cyclodextrin Membranes for High- Performance Organic Solvent Nanofiltration, Adv. Funct. Mater., 30 (2019) 1906797.
[68] W. Fu, Y. Huang, L. Deng, J. Sun, S.-L. Li, Y. Hu, Ultra-thin microporous membranes based on macrocyclic pillar[n]arene for efficient organic solvent nanofiltration, J. Membr. Sci., 655 (2022) 120583.
[69] Z. Zhai, C. Jiang, N. Zhao, W. Dong, P. Li, H. Sun, Q.J. Niu, Polyarylate membrane constructed from porous organic cage for high-performance organic solvent nanofiltration, J. Membr. Sci., 595 (2020) 117505.
[70] W. Fu, W. Zhang, H. Chen, S.-L. Li, W. Shi, Y. Hu, A high-flux organic solvent nanofiltration membrane with binaphthol-based rigid-flexible microporous structures, J. Mater. Chem. A, 9 (2021) 7180-7189.
[71] S.L. Li, G. Chang, Y. Huang, K. Kinooka, Y. Chen, W. Fu, G. Gong, T. Yoshioka, N.B. McKeown, Y. Hu, 2,2'-Biphenol-based Ultrathin Microporous Nanofilms for Highly Efficient Molecular Sieving Separation, Angew. Chem. Int. Ed. Engl., 61 (2022) e202212816.
[72] M.F. Jimenez-Solomon, Q. Song, K.E. Jelfs, M. Munoz-Ibanez, A.G. Livingston, Polymer nanofilms with enhanced microporosity by interfacial polymerization, Nat Mater, 15 (2016) 760-767.
[73] T.H. Bae, J. Liu, J.S. Lee, W.J. Koros, C.W. Jones, S. Nair, Facile high-yield solvothermal deposition of inorganic nanostructures on zeolite crystals for mixed matrix membrane fabrication, J. Am. Chem. Soc., 131 (2009) 14662-14663.
[74] L. Gui, J. Dong, W. Fang, S. Zhang, K. Zhou, Y. Zhu, Y. Zhang, J. Jin, Ultrafast Ion Sieving from Honeycomb-like Polyamide Membranes Formed Using Porous Protein Assemblies, Nano Lett., 20 (2020) 5821-5829.
[75] R.H. Hailemariam, J.-S. Choi, M.M. Damtie, H. Rho, K.-D. Park, J. Lee, Y.C. Woo, Enhancing performances of polyamide thin film composite membranes via co-solvent assisted interfacial polymerization, Desalination, 524 (2022) 115481.

[76] Q. Gan, L.E. Peng, H. Guo, Z. Yang, C.Y. Tang, Cosolvent-Assisted Interfacial Polymerization toward Regulating the Morphology and Performance of Polyamide Reverse Osmosis Membranes: Increased m-Phenylenediamine Solubility or Enhanced Interfacial Vaporization?, Environ. Sci. Technol., 56 (2022) 10308-10316.
[77] J.Y. Sum, J.J. Beh, A.L. Ahmad, B.S. Ooi, Enhancing the solvent-dendrimer miscibility at the interface and its impact on the thin film composite membrane, Journal of Industrial and Engineering Chemistry, 58 (2018) 229-239.
[78] T. Kamada, T. Ohara, T. Shintani, T. Tsuru, Controlled surface morphology of polyamide membranes via the addition of co-solvent for improved permeate flux, J. Membr. Sci., 467 (2014) 303-312.
[79] C. Kong, M. Kanezashi, T. Yamomoto, T. Shintani, T. Tsuru, Controlled synthesis of high performance polyamide membrane with thin dense layer for water desalination, J. Membr. Sci., 362 (2010) 76-80.
[80] C. Kong, T. Shintani, T. Kamada, V. Freger, T. Tsuru, Co-solvent-mediated synthesis of thin polyamide membranes, J. Membr. Sci., 384 (2011) 10-16.
[81] J. Lee, R. Wang, T.-H. Bae, A comprehensive understanding of co-solvent effects on interfacial polymerization: Interaction with trimesoyl chloride, J. Membr. Sci., 583 (2019) 70-80.
[82] C. Li, Y. Zhao, G.S. Lai, R. Wang, Investigation of aqueous and organic co-solvents roles in fabricating seawater reverse osmosis membrane, J. Membr. Sci., 645 (2022) 120187.
[83] C. Liu, R. Takagi, T. Shintani, L. Cheng, K.L. Tung, H. Matsuyama, Organic Liquid Mixture Separation Using an Aliphatic Polyketone-Supported Polyamide Organic Solvent Reverse Osmosis (OSRO) Membrane, ACS Appl Mater Interfaces, 12 (2020) 7586-7594.
[84] R.R. Gonzales, L. Zhang, Y. Sasaki, W. Kushida, H. Matsuyama, H.K. Shon, Facile development of comprehensively fouling-resistant reduced polyketone-based thin film composite forward osmosis membrane for treatment of oily wastewater, J. Membr. Sci., 626 (2021) 119185.
[85] K. Guan, Y. Sasaki, Y. Jia, R.R. Gonzales, P. Zhang, Y. Lin, Z. Li, H. Matsuyama, Interfacial polymerization of thin film selective membrane layers: Effect of polyketone substrates, J. Membr. Sci., 640 (2021) 119801.
[86] P. Ball, Chemical physics: How to keep dry in water, Nature, 423 (2003) 25-26.
[87] A. Poynor, L. Hong, I.K. Robinson, S. Granick, Z. Zhang, P.A. Fenter, How water meets a hydrophobic surface, Phys. Rev. Lett., 97 (2006) 266101.
[88] D. Chandler, Physical chemistry: oil on troubled waters, Nature, 445 (2007) 831-832.
[89] L. Benjamin, Mechanism and dynamics of ion transfer across a liquid-liquid interface, Science, 261 (1993) 1558-1560.
[90] I.L. Carpenter, W.J. Hehre, A molecular dynamics study of the hexane/water interface, The Journal of Physical Chemistry, 94 (2002) 531-536.
[91] Q. Shen, Y. Lin, P. Zhang, J. Segawa, Y. Jia, T. Istirokhatun, X. Cao, K. Guan, H. Matsuyama, Development of ultrathin polyamide nanofilm with enhanced inner-pore interconnectivity via graphene quantum dots-assembly intercalation for high-

performance organic solvent nanofiltration, J. Membr. Sci., 635 (2021) 119498.
[92] K. Grzebyk, M.D. Armstrong, O. Coronell, Accessing greater thickness and new morphology features in polyamide active layers of thin-film composite membranes by reducing restrictions in amine monomer supply, J Memb Sci, 644 (2022) 120112.
[93] L.E. Peng, Z. Yao, Z. Yang, H. Guo, C.Y. Tang, Dissecting the Role of Substrate on the Morphology and Separation Properties of Thin Film Composite Polyamide Membranes: Seeing Is Believing, Environ. Sci. Technol., 54 (2020) 6978-6986.
[94] L.E. Peng, Z. Yang, L. Long, S. Zhou, H. Guo, C.Y. Tang, A critical review on porous substrates of TFC polyamide membranes: Mechanisms, membrane performances, and future perspectives, J. Membr. Sci., 641 (2022) 119871.
[95] M. Kahrizi, R.R. Gonzales, L. Kong, H. Matsuyama, P. Lu, J. Lin, S. Zhao, Significant roles of substrate properties in forward osmosis membrane performance: A review, Desalination, 528 (2022) 115615.
[96] M.C.Y. Wong, L. Lin, O. Coronell, E.M.V. Hoek, G.Z. Ramon, Impact of liquid-filled voids within the active layer on transport through thin-film composite membranes, J. Membr. Sci., 500 (2016) 124-135.
[97] L. Lin, R. Lopez, G.Z. Ramon, O. Coronell, Investigating the void structure of the polyamide active layers of thin-film composite membranes, J. Membr. Sci., 497 (2016) 365-376.
[98] X. Ma, Z. Yang, Z. Yao, H. Guo, Z. Xu, C.Y. Tang, Tuning roughness features of thin film composite polyamide membranes for simultaneously enhanced permeability, selectivity and anti-fouling performance, J. Colloid Interface Sci., 540 (2019) 382-388.
[99] I. Nulens, A. Ben Zvi, I.F.J. Vankelecom, G.Z. Ramon, Re-thinking polyamide thin film formation: How does interfacial destabilization dictate film morphology?, J. Membr. Sci., 656 (2022) 120593.
[100] P.W. Morgan, S.L. Kwolek, Interfacial polycondensation. II. Fundamentals of polymer formation at liquid interfaces, J. Polym. Sci., Part A: Polym. Chem., 34 (1996) 531-559.
[101] R. Patne, G.Z. Ramon, Stability of fluid flows coupled by a deformable solid layer, J. Fluid Mech., 905 (2020) A36.
[102] J. Zhang, B. Sun, X. Huang, S. Chen, G. Wang, Honeycomb-like porous gel polymer electrolyte membrane for lithium ion batteries with enhanced safety, Sci. Rep., 4 (2014) 6007.
[103] M.H. Stenzel, C. Barner-Kowollik, T.P. Davis, Formation of honeycomb-structured, porous films via breath figures with different polymer architectures, J. Polym. Sci., Part A: Polym. Chem., 44 (2006) 2363-2375.
[104] S. Sorribas, P. Gorgojo, C. Tellez, J. Coronas, A.G. Livingston, High flux thin film nanocomposite membranes based on metal-organic frameworks for organic solvent nanofiltration, J. Am. Chem. Soc., 135 (2013) 15201-15208.
[105] Q. Liu, X. Wu, K. Zhang, Polysulfone/Polyamide-SiO(2) Composite Membrane with High Permeance for Organic Solvent Nanofiltration, Membranes (Basel), 8 (2018) 89.
[106] J. Liu, D. Hua, Y. Zhang, S. Japip, T.S. Chung, Precise Molecular Sieving Architectures with Janus Pathways for Both Polar and Nonpolar Molecules, Adv

Mater, 30 (2018).
[107] D.Y. Koh, B.A. McCool, H.W. Deckman, R.P. Lively, Reverse osmosis molecular differentiation of organic liquids using carbon molecular sieve membranes, Science, 353 (2016) 804-807.
[108] M.L. Jue, D.-Y. Koh, B.A. McCool, R.P. Lively, Enabling Widespread Use of Microporous Materials for Challenging Organic Solvent Separations, Chemistry of Materials, 29 (2017) 9863-9876.
[109] C.J. Roos, D.J. Weber, H.Y. Jang, R.P. Lively, Matching Analysis of Mixed Matrix Membranes for Organic Solvent Reverse Osmosis, Ind. Eng. Chem. Res., 61 (2022) 3395-3411.
[110] G. Dong, H. Nagasawa, L. Yu, M. Guo, M. Kanezashi, T. Yoshioka, T. Tsuru, Energy-efficient separation of organic liquids using organosilica membranes via a reverse osmosis route, J. Membr. Sci., 597 (2020) 117758.
[111] W. Kushida, R.R. Gonzales, T. Shintani, A. Matsuoka, K. Nakagawa, T. Yoshioka, H. Matsuyama, Organic solvent mixture separation using fluorine-incorporated thin film composite reverse osmosis membrane, J. Mater. Chem. A, 10 (2022) 4146-4156.
[112] Y. Zhang, H. Wang, J. Guo, X. Cheng, G. Han, C.H. Lau, H. Lin, S. Liu, J. Ma, L. Shao, Ice-confined synthesis of highly ionized 3D-quasilayered polyamide nanofiltration membranes, Science, 382 (2023) 202-206.
[113] M. Elimelech, W.A. Phillip, The future of seawater desalination: energy, technology, and the environment, Science, 333 (2011) 712-717.
[114] L. Deng, R.R. Gonzales, W. Fu, G. Xu, R. Takagi, Q. Song, S. Zhou, H. Matsuyama, Organic solvent separation using carbon nanotube-interlayered thin film composite membrane, Chem. Eng. J., 473 (2023) 145197.
[115] K. Guan, S. Fang, S. Zhou, W. Fu, Z. Li, R.R. Gonzales, P. Xu, Z. Mai, M. Hu, P. Zhang, H. Matsuyama, Thin film composite membrane with improved permeance for reverse osmosis and organic solvent reverse osmosis, J. Membr. Sci., 688 (2023) 122104.
[116] Z.H. Foo, D. Rehman, O.Z. Coombs, A. Deshmukh, J.H. Lienhard, Multicomponent Fickian solution-diffusion model for osmotic transport through membranes, J. Membr. Sci., 640 (2021) 119819.
[117] H. Jalaei Salmani, R. Hardian, H. Kalani, M.R. Moradi, H. Karkhanechi, G. Szekely, H. Matsuyama, Predicting the performance of organic solvent reverse osmosis membranes using artificial neural network and principal component analysis by considering solvent–solvent and solvent–membrane affinities, J. Membr. Sci., 687 (2023) 122025.
[118] C. Liu, L. Cheng, T. Shintani, H. Matsuyama, AF2400/polyketone composite organic solvent reverse osmosis membrane for organic liquid separation, J. Membr. Sci., 628 (2021) 119270.
[119] W. Fu, L. Deng, M. Hu, Z. Mai, G. Xu, Y. Shi, K. Guan, R.R. Gonzales, A. Matsuoka, H. Matsuyama, Polyamide composite membrane with 3D honeycomb-like structure via acetone-regulated interfacial polymerization for high-efficiency organic solvent nanofiltration, J. Membr. Sci., 679 (2023) 121711.

[120] Y.H. See Toh, F.W. Lim, A.G. Livingston, Polymeric membranes for nanofiltration in polar aprotic solvents, J. Membr. Sci., 301 (2007) 3-10.
[121] W. Gunsteren, Biomolecular simulation: the GROMOS96 manual and user guide. VDF Hochschulverlag AG ander ETH Zürich, Zürich, (1996).
[122] B. Hess, C. Kutzner, D. van der Spoel, E. Lindahl, GROMACS 4: Algorithms for Highly Efficient, Load-Balanced, and Scalable Molecular Simulation, J. Chem. Theory Comput., 4 (2008) 435-447.
[123] D. Van Der Spoel, E. Lindahl, B. Hess, G. Groenhof, A.E. Mark, H.J. Berendsen, GROMACS: fast, flexible, and free, J. Comput. Chem., 26 (2005) 1701-1718.
[124] E. Lindahl, B. Hess, D. van der Spoel, GROMACS 3.0: a package for molecular simulation and trajectory analysis, J. Mol. Model., 7 (2001) 306-317.
[125] C. Oostenbrink, A. Villa, A.E. Mark, W.F. van Gunsteren, A biomolecular force field based on the free enthalpy of hydration and solvation: the GROMOS force-field parameter sets 53A5 and 53A6, J. Comput. Chem., 25 (2004) 1656-1676.
[126] C. Gaussian 16 Rev. C.01 (Wallingford, 2016).
[127] T. Darden, D. York, L. Pedersen, Particle mesh Ewald: An N·log(N) method for Ewald sums in large systems, J. Chem. Phys., 98 (1993) 10089-10092.
[128] U. Essmann, L. Perera, M.L. Berkowitz, T. Darden, H. Lee, L.G. Pedersen, A smooth particle mesh Ewald method, J. Chem. Phys., 103 (1995) 8577-8593.
[129] B. Hess, H. Bekker, H.J. Berendsen, J.G. Fraaije, LINCS: A linear constraint solver for molecular simulations, J. Comput. Chem., 18 (1997) 1463-1472.
[130] Q. Zhao, D.L. Zhao, L.Y. Ee, T.-S. Chung, S.B. Chen, In-situ coating of Fe-TA complex on thin-film composite membranes for improved water permeance in reverse osmosis desalination, Desalination, 554 (2023) 116515.
[131] Y.-H. Chiao, Z. Mai, W.-S. Hung, H. Matsuyama, Osmotically assisted solvent reverse osmosis membrane for dewatering of aqueous ethanol solution, J. Membr. Sci., 672 (2023) 121434.
[132] J. Wu, Z. Wang, W. Yan, Y. Wang, J. Wang, S. Wang, Improving the hydrophilicity and fouling resistance of RO membranes by surface immobilization of PVP based on a metal-polyphenol precursor layer, J. Membr. Sci., 496 (2015) 58-69.
[133] J. Carpenter, H. Kim, J. Suarez, A. van der Zande, N. Miljkovic, The Surface Energy of Hydrogenated and Fluorinated Graphene, ACS Appl Mater Interfaces, 15 (2023) 2429-2436.
[134] A. Kozbial, Z. Li, C. Conaway, R. McGinley, S. Dhingra, V. Vahdat, F. Zhou, B. D'Urso, H. Liu, L. Li, Study on the surface energy of graphene by contact angle measurements, Langmuir, 30 (2014) 8598-8606.
[135] R. Zhang, Y. Liu, M. He, Y. Su, X. Zhao, M. Elimelech, Z. Jiang, Antifouling membranes for sustainable water purification: strategies and mechanisms, Chem. Soc. Rev., 45 (2016) 5888-5924.
[136] W. Bai, L. Samineni, P. Chirontoni, I. Krupa, P. Kasak, A. Popelka, N.B. Saleh, M. Kumar, Quantifying and reducing concentration polarization in reverse osmosis systems, Desalination, 554 (2023) 116480.
[137] R. Epsztein, E. Shaulsky, M. Qin, M. Elimelech, Activation behavior for ion

permeation in ion-exchange membranes: Role of ion dehydration in selective transport, J. Membr. Sci., 580 (2019) 316-326.
[138] R.Y.M. Huang, G.Y. Moon, R. Pal, N-acetylated chitosan membranes for the pervaporation separation of alcohol/toluene mixtures, J. Membr. Sci., 176 (2000) 223-231.
[139] Z. Zhu, W. Bai, Y. Xu, H. Gong, Y. Wang, D. Xu, J. Gao, Liquid-liquid extraction of methanol from its mixtures with hexane using three imidazolium-based ionic liquids, The Journal of Chemical Thermodynamics, 138 (2019) 189-195.
[140] N. Tsubaki, M. Ito, K. Fujimoto, A New Method of Low-Temperature Methanol Synthesis, J. Catal., 197 (2001) 224-227.
[141] G. Dong, Y. Zhang, T. Sato, H. Nagasawa, M. Kanezashi, T. Tsuru, Reverse osmosis and pervaporation of organic liquids using organosilica membranes: Performance analysis and predictions, AlChE J., 68 (2022) e17585.
[142] G. Dong, H. Nagasawa, M. Kanezashi, T. Tsuru, Experimental study and modeling of organic solvent reverse osmosis separations through organosilica membranes, AlChE J., 66 (2020) e16283.
[143] J.J. Max, C. Chapados, Infrared spectroscopy of methanol-hexane liquid mixtures. II. The strength of hydrogen bonding, J. Chem. Phys., 130 (2009) 124513.
[144] I. Essafri, A. Ghoufi, Microstructure of nonideal methanol binary liquid mixtures, Phys Rev E, 99 (2019) 062607.
[145] H.Y. Jang, R.P. Lively, The role of skin layer defects in organic solvent reverse osmosis membranes, Journal of Membrane Science Letters, 1 (2021) 100004.
[146] W. Zhang, G. Li, Y. Fang, X. Wang, Maleic anhydride surface-modification of crosslinked chitosan membrane and its pervaporation performance, J. Membr. Sci., 295 (2007) 130-138.
[147] N.T. Correia, J.J.M. Ramos, B.J.V. Saramago, J.C.G. Calado, Estimation of the Surface Tension of a Solid: Application to a Liquid Crystalline Polymer, J. Colloid Interface Sci., 189 (1997) 361-369.
[148] J. Gao, S.-P. Sun, W.-P. Zhu, T.-S. Chung, Green modification of outer selective P84 nanofiltration (NF) hollow fiber membranes for cadmium removal, J. Membr. Sci., 499 (2016) 361-369.
[149] M. Jiang, K. Ye, J. Deng, J. Lin, W. Ye, S. Zhao, B. Van der Bruggen, Conventional Ultrafiltration As Effective Strategy for Dye/Salt Fractionation in Textile Wastewater Treatment, Environ. Sci. Technol., 52 (2018) 10698-10708.
[150] Y. Lin, Q. Shen, Y. Kawabata, J. Segawa, X. Cao, K. Guan, T. Istirokhatun, T. Yoshioka, H. Matsuyama, Graphene quantum dots (GQDs)-assembled membranes with intrinsic functionalized nanochannels for high-performance nanofiltration, Chem. Eng. J., 420 (2021) 127602.
[151] G. Martínez-Mejía, N.A. Vázquez-Torres, A. Castell-Rodríguez, J.M. del Río, M. Corea, R. Jiménez-Juárez, Synthesis of new chitosan-glutaraldehyde scaffolds for tissue engineering using Schiff reactions, Colloids Surf. Physicochem. Eng. Aspects, 579 (2019) 123658.
[152] W. Fu, M. Hu, J. Liu, L. Deng, K. Guan, R.R. Gonzales, S. Fang, Z. Wang, Y. Shi, S. Xiang, P. Zhang, W. Shi, H. Matsuyama, Surface polarity modulation enables

high-performance polyamide membranes for separation of polar/non-polar organic solvent mixtures, J. Membr. Sci., 704 (2024) 122901.
[153] D. Paul, Reformulation of the solution-diffusion theory of reverse osmosis, J. Membr. Sci., 241 (2004) 371-386.

Chapter 5: Conclusions

Organic solvent separation and purification (OSSP) techniques are indispensable in various industries, including chemical processing, pharmaceuticals, and environmental protection. Compared to conventional OSSP methods, membrane separation technology stands out as a promising alternative due to its advantages in simplicity, selectivity, energy efficiency, and environmental sustainability. Among various polymer membranes, polyamide (PA) membranes have emerged as the most promising candidates for OSSP owing to their excellent solvent resistance and high separation selectivity. PA OSSP membranes can be further categorized into PA organic solvent nanofiltration (OSN) and PA organic solvent reverse osmosis (OSRO) membranes based on the size of the target solutes. However, PA OSN membranes face limitations such as low permeation surface area and flux, while PA OSRO membranes suffer from weak surface polarity, broad pore size distribution, and low separation efficiency. To address these challenges and develop high-performance PA OSSP membranes, this study delves into comprehensive explorations and discussions.

In Chapter 2, to overcome the issues of small permeation surface area and low flux in PA OSN membranes, this study employed an acetone-assisted interfacial polymerization strategy to optimize the membrane structure, creating PA membranes with a unique 3D honeycomb-like structure. This distinctive structure endowed the PA membranes with an exceptionally high specific surface area, significantly improving their OSN performance. In Chapter 3, addressing the problem of low separation efficiency in PA OSRO membranes due to weak surface polarity, this study innovatively applied a physical surface modification method. By coating the PA membrane surface with an Fe3+/TA layer, an enhanced polarity surface was constructed. The increased surface polarity facilitated the formation of a polarization layer on the PA membrane surface while reducing concentration polarization effects, enhancing the interaction differences between polar and non-polar solvents on the

membrane surface, ultimately significantly improving the separation efficiency of the PA membrane for polar/non-polar mixtures. In Chapter 4, to address the issue of low separation efficiency in PA OSRO membranes due to wide pore size distribution, this study employed surface repair engineering techniques. By coating the PA membrane surface with a CS/GA layer, the membrane pores on the PA surface were blocked and repaired, resulting in a PA composite membrane with a narrow pore size distribution. This PA composite membrane with a narrow pore size distribution exhibited extremely high OSRO separation performance. All the results were described in Chapters 2-4, as follows:

5.1 Polyamide composite membrane with 3D honeycomb-like structure via acetone-regulated interfacial polymerization for high-efficiency organic solvent nanofiltration

In this chapter, a high-performance TFC-PA OSN membrane with a 3D honeycomb-like structure on porous PK supports was developed by regulating the IP process with acetone as an organic co-solvent. The experimental results emphasized that acetone regulation and sufficient MPD supply through PK supports during the IP process were the necessary conditions for the formation of a honeycomb-like structured PA layer. Both the experimental and MD simulation results confirmed that the acetone co-solvent enlarged the IP reaction zone and greatly promoted the convective diffusion of MPD and TMC, leading to a more vigorous IP reaction. The increased heat release led to aggravated vaporization of acetone, which facilitated the formation of a 3D honeycomb-like structure of the PA layer. Such a 3D honeycomb-like structure endowed the TFC-PA-acetone membrane with an ultrahigh specific surface area. Compared with the TFC-PA membrane prepared by the conventional IP method, the optimized TFC-PA-acetone membrane demonstrated 2.6 times higher MeOH solvent permeance (7.0 LMH/bar) and comparable MO selectivity (94.6%). This work explored the underlying mechanism of acetone co-solvents in IP reactions, providing new ideas for tailoring the membrane morphology and separation properties

for high-efficiency organic solvent nanofiltration.

5.2 Surface polarity modulation enables high-performance polyamide membranes for separation of polar/non-polar organic solvent mixtures

This study successfully developed a high-performance OSRO membrane with enhanced surface polarity by coating a layer of Fe^{3+}/TA complex on the surface of the PA membrane. Experimental and simulation results highlight that enhanced surface polarity of the membrane increased the interaction disparity between polar and non-polar solvents and the membrane, and formed a polarization layer on the membrane surface, thereby weakening the concentration polarization effect on the membrane surface. Consequently, the PA-Fe^{3+}/TA membrane exhibited improved permeability and selectivity, breaking the inherent trade-off effect associated with PA membranes. In addition, the concept of partial flux was proposed to further understand the pressure, concentration dependence and sensitivity of separation performance in the OSRO process. This provides valuable reference for in-depth understanding of the OSRO mass transfer process.

This work underscores the significance of further research into the mass transfer mechanisms of the OSRO process, particularly in understanding the interactions between components of the organic mixtures and the membrane. Optimizing and regulating the interactions are identified as crucial factors on improving separation efficiency. Overall, the findings contribute a simple and practical method for developing high-performance OSRO membranes and enhance the understanding of the role of PA membranes in the separation of polar/non-polar liquid mixtures

5.3 Surface repair engineering of polyamide membranes for high-performance organic solvent reverse osmosis

In this chapter, a high-performance OSRO membrane with smaller pore size and narrower pore size distribution was developed by coating a layer of CS/GA on the surface of the PA membrane. The experimental results emphasized that coating the

CS/GA layer effectively repaired the defects on the PA membrane surface. The similar responses of the TFC-PA-CS-0.2 membrane and the TFC-PA membrane to pressure and feed concentration prove that the separation characteristics of the PA composite membrane are not changed after coating the CS/GA layer. Importantly, the CS/GA layer reduces the pore size of the TFC membrane, achieving smaller pore size and narrower pore size distribution. Compared with TFC-PA membrane, the optimal TFC-PA-CS-0.2 membrane exhibits 2.4 times higher separation factor of M90T10. Overall, this study provides a simple and practical method for developing high-performance OSRO membranes.

Publication list

Chapter 2:

Fu. W, Deng. L, Hu. M, et al. Polyamide composite membrane with 3D honeycomb-like structure via acetone-regulated interfacial polymerization for high-efficiency organic solvent nanofiltration[J]. Journal of Membrane Science, 2023, 679: 121711.

Chapter 3:

Fu. W, Hu. M, Liu J, et al. Surface polarity modulation enables high-performance polyamide membranes for separation of polar/non-polar organic solvent mixtures[J]. Journal of Membrane Science, 2024, 704: 122901.

Chapter 4:

Fu. W, Hu. M, Liu J, et al. Surface repair engineering of polyamide membranes for high-performance organic solvent reverse osmosis. (submitted)

Doctoral Dissertation, Kobe University

“Preparation of polyamide-based composite membranes and investigation of their performance in organic solvent separation (ポリアミド系複合膜の作製と有機溶媒分離性能の検討)”, 111 pages

Submitted on Jul 01, 2024

When published on the Kobe University institutional repository */Kernel/*, the publication date shall appear on the cover of the repository version.